Photovoltage detection of spin excitations of nanocrystals and nanomagnets with 2D electron systems

Almulhem, Najla

Award date:
2020

Awarding institution:
University of Bath

Photovoltage detection of spin excitations of nanocrystals and nanomagnets with 2D electron systems

submitted by

Najla Khaled Almulhem

for the degree of Doctor of Philosophy of the

University of Bath

Department of Physics

January 2020

Abstract

Photovoltage spectroscopy is an attractive technique for investigating the dynamic properties of the spin excitations of sub-micron scale ferromagnetic elements (cobalt stripes or disks) fabricated on the surface of a $GaAs/Al_{0.33}Ga_{0.67}As$ heterojunction. Localised spin wave modes are detected via the photovoltage induced in a two-dimensional electron gas (2DEG) formed in the heterojunction. The two-dimensional nature of the detector separates the effects of the in-plane and normal vector components of the magnetisation. The high sensitivity of this technique arises from the high electron mobility and low electron density of 2DEGs relative to metals, given by, respectively, $\mu = 1.5 \times 10^6 cm^2 V^{-1} s^{-1}$ and $n_s = 1.6 \times 10^{11} cm^{-2}$. We report on the discrete structure of spin wave resonance as a function of the shape of the cobalt magnet, the geometry of the magnets, and the magnetic field orientation (perpendicular or parallel to the magnetisation). Spin wave resonances in a micromagnetic stripe are experimentally measured at different frequencies at low temperature and the cases of perpendicular and parallel field orientation are compared. The photovoltage spectra are modelled using micromagnetic simulation (OOMMF). The photovoltage resonances indicate the presence of Damon-Eshbach modes when B_{dc} is parallel to the long axis of the stripe. Bonding-antibonding spin waves are observed when B_{dc} is perpendicular to the long axis of the stripe. We also describe the discrete structure of photovoltage spectroscopy for individual disks. Our cobalt disk has a 40 nm radius and is magnetised perpendicular to the 2DEG by the static magnetic field. Tilting B_{dc} in the plane does no effect on the photovoltage for symmetry reasons. Our results show that photovoltage measurements in hybrid semiconductor-ferromagnetic structures provide a sensitive and versatile tool for probing the spin waves of small magnets of size $\sim$ 80 nm.

Acknowledgments

At this point, I would like to take this opportunity to thank several people who deserve great praise and thanks for their support and help, both practical and in terms of influence, inspiration, and sheer patience.

I would first like to express massive gratitude to my supervisor, Professor Alain Nogaret for his unlimited support, encouragement, patience, and for giving me the excellent opportunity to do research at this level. I am grateful for the time he has taken amidst his busy schedule to dispel my concerns, large or small, academic or personal. I also thank my second supervisor, Dr Steven Davies, for all of his helpful advice in designing the microstrip antenna. Furthermore, I would like to thank the University of Bath for providing a friendly and engaging work environment. The past four years have been tough, but nonetheless memorable, and I have learned many new skills.

In addition, I am grateful to the many collaborators and groups who have aided me in making this research possible. This includes the technical staff in the Department of Physics in particular Paul Reddish, for building the microwave bench used in the experiments and providing me with the liquid nitrogen; Dr Maksym Stability, for his assistance during the OOMMF simulations; Joseph Taylor, who always helps me in any difficulty especially with language; and Nisrin Alnaim who is my closest friend in the Department of Physics, for always understanding and listening to me.

I would like to thank my family, whose unwavering love and support have allowed me to chase this dream of mine. I cannot find the words to truly express my gratitude for all of your help over the years. I particularly mention my siblings (**Noora, Ahmed, Nuorah, Latifah, Malak, and Rayan**), for their ever-present love, and photo updates about my nieces and nephews (**Khalid, Ghadah, Huda, Mohammed, Abdulrahman, Najla, and Yousef**). I must highlight my uncle

Ibrahim, who always believed in my abilities. Finally, I am ever indebted to both my admirable parents **Hoda Almulhem** and **Khalid Almolhim** for being my biggest supporters through this time, and for being at my side in all the decisions I have made. This thesis is a gift from me to my parents, as a symbolic reward for their everlasting dedication to their sons and grandsons even today, and the future will be better Inshaa Allah.

I am truly indebted to you all forever. Thank you so much.

Contents

List of Figures

Chapter 1

Introduction

The science and applications of nanomagnets is dependent upon insights into their discrete magnetic excitation modes, where surface effects are paramount [1, 2, 3, 4]. Numerous applications have exploited the localisation of spin-wave states, for example in spintronic devices for phase-resolved microwave sensors or in the high-density magnetic information storage and high-frequency (GHz) retrieval required by hard disk drives where a larger density is further desirable, for it allows more extra data to be stored in the same physical space [5, 6, 7, 8, 9]. The collective dynamics of the most interesting individual submicron magnets is currently inaccessible by standard methods, such as Brillouin light scattering (BLS) owing to the need for a large volume of the magnetic material used to obtain an optical signal [10, 11].

BLS is among the most important approaches for examining the dynamics of magnetic materials. It is an optical technique that measures the spin wave's momentum energy in samples that are larger than the wavelength of light ($\sim$ 500 nm). It gives information on energy losses incurred through the momentum $\hbar k = \vec{k} - \vec{k'}$, where $\vec{k}$ and $\vec{k'}$ are the wavevectors of the incident and scattered photons, respectively. In this manner, the energy-momentum $\omega(q)$ dispersion curves for the combined excitation of the electron spin structure (magnon) [2, 12] may be measured. However, due to the significant bulk of magnetic material required for an optical signal, which necessitates an array of micromagnets and

precludes the probing of individual magnets, BLS is presently unable to examine the combined dynamics of the most noteworthy individual submicron magnets [13, 14].

In the present work, a photovoltage spectroscopy technique is used to detect spin dynamics in submicron magnets [14, 15, 16, 17, 18]. The devices described here contain Co nanomagnets (stripe or dot) at the centre of a Hall bar system and are excited at microwave frequencies. The microwave frequency is detected via induced magnetic resonance at the active region of the Hall bar device [19]. The nanomagnets were microfabricated at the surface of $GaAs/Al_{0.33}Ga_{0.67}As$ heterojunction forming a two-dimensional electron gas (2DEG). The electrons are located at the interface of two layers of two semiconducting layers($GaAs$ and $AlGaAs$). When both materials are brought into contact, the electrons become conned in a plane [20, 21, 22].

Electron resonance, hereafter referred to as electron spin resonance (ESR), is generated by the application of both a static and a time-dependent magnetic field, the latter generally being provided by the magnetic component of an electromagnetic wave. The spin magnetic moment undergoes precesses at a frequency proportional to the magnitude of the static magnetic field (the Larmor frequency) and magnetic resonance is generated when this frequency equals that of the time-dependent magnetic field. While electrical measurement of microwave induced electron spin resonance in 2DEGs was established over twenty years ago under highly specific conditions by Dobers et al [23]. This thesis describes a more versatile and reliable technique.

The application of a static magnetic field, B_{dc}, in the plane of the 2DEG, but across the magnetic stripe, magnetises the stripe so that the 2DEG is subjected to a nearly linear perpendicular magnetic field gradient. Thus, the 2DEG has two regions which are subject to magnetic field of opposite sign and separated by a line where the magnetic field vanishes, called the magnetic edge. The spins in the magnetic stripe are able to exhibit magnetic resonance as well; this effect is called ferromagnetic resonance. When ferromagnetic resonance is induced, the magnetisation of the magnetic stripe oscillates at high frequency and the effective magnetic potential felt by the 2DEG oscillates and is rectified by the Hall effect which brings contribution to the current quadratic in B. Using this effect, the

2DEG can be employed as a sensor to detect perturbations to the spin ensemble of very small magnetic samples. This technique can detect the resonance of localised magnetic moments through the eddy current they induce in a high mobility 2DEG.

Inside the magnetic stripe, there is an internal magnetic field which is inhomogeneous in the plane of the magnetic stripe, being stronger in the middle of the stripe and decreasing considerably as it approaches the side edges. By applying microwave frequencies to the sample, the phase of the spins inside the magnetic material starts oscillating, giving rise to spin waves. The spin waves propagate transversely inside the stripe and become confined in the region of lower internal field. This area acts as a quantum well, discretising the spin-wave modes which can propagate in the area. This type of spin waves is called dipolar edge spin waves (DESW).

In the experiments described here, localised spin-wave modes are confined by a non-uniform magnetic field generated near the poles of a cobalt magnet, either a strip (width $\sim$ 80 nm and thickness $\sim$ 30 nm) created by applying a static field along the short axis of the nanomagnetic stripe or a disk (diameter $\sim$ 80 nm and thickness $\sim$ 30 nm) that is magnetised in-plane. By rectifying the high-frequency oscillation of the is magnetisation vector, the high sensitivity of the 2DEG to the dynamics of ultra-small magnetic elements at its surface is demonstrated. The discrete structure of the spin-wave resonance is described as a function of the shape of the cobalt magnet, the geometry of the magnets and the magnetic field orientation (perpendicular or parallel to the magnetisation).

When a static field is applied along the long axis of the nanomagnetic stripe, the internal magnetic field is homogeneous and equal to the applied magnetic field. Hence, there is a magnetostatic boundary condition that forces spin-wave modes to the surface of the magnets. The stripe then shows a backward volume mode which is modulated by Damon–Eshbach modes (DE), which propagate at the edges parallel to the external magnetic field.

The thesis is divided into the following chapters:

Chapter 2 introduces the pertinent theoretical principles of nanomagnetism, including the theory of magnetism, the exchange interaction, the states of a spin

1/2 particle in an ac magnetic field, ferromagnetic resonance, shape anisotropy, dynamic phenomena, magnetocrystalline anisotropy and the concept of the 2DEG.

Chapter 3 details the experimental setup and measurement procedure, including the preparation of the samples, the microwave bench and the microstrip antenna along with an examination of the principles behind the instrumentation employed. The measurement process is described using the LabVIEW program. The Object-Oriented MicroMagnetic Framework (OOMMF) which is a powerful program for simulating the dynamics of micromagnetic moments and photovoltage spectra is outlined as well.

Chapter 4 illustrates the ferromagnetic resonance of individual strips as a function of the magnetic field orientation, while the ferromagnetic resonance of the magnetic disk is detailed in Chapter 5. In brief, the results presented in Chapters 4 and 5 demonstrate the following:

- When B_{dc} is perpendicular to the long side of the rectangular magnetic strip, strong bulk-edge mode coupling is observed in the form of bonding-antibonding spin waves at various frequencies and low temperatures.

- Damon-Eshbach modes are only observed when B_{dc} is parallel to the long side (to the dc magnetic field) of the strip at different frequencies and low temperatures [24, 25, 26].

- A discrete structure of spin-wave resonance is detected for nanometer-size magnetic disks magnetised parallel to the 2DEG by the static magnetic field. The parallel orientation is no different than the perpendicular for symmetry measures [27].

- The experimental results are discussed along with the results of a theoretical simulation of the micromagnets' susceptibility using the OOMMF program [28].

- Ferromagnetic resonances shift to a new position under the influence of magnetocrystalline anisotropy in the experimental results only [29, 30].

- The photovoltage formula works very well to describe the experiments, giving a Lorentzian-type shape where the width of the resonances is connected

to the damping. The full-width-at-half-maximum (FWHM) of the resonance is utilised for describing the width of the peak [31, 32].

Finally, the conclusions of the work are summarized in Chapter 6 along with recommendations for future investigations. The overall conclusion is that photovoltage measurements in hybrid semiconductor-ferromagnetic structures furnish a powerful and widely applicable technique for examining the localisation of spin waves in small-scale magnets and the photovoltage of a perpendicularly magnetised stripe is larger because the induced modulation is larger than that in the parallel configuration [33, 34].

Chapter 2

Theoretical Fundamentals

The present chapter provides a theoretical background on magnetism that is used to interpret the results obtained in the later chapters of this thesis. This chapter focuses on the basic concepts of magnetism. It also introduces some essential magnetic phenomena that allow describing the work such as the dispersion relation of confined spin waves. Further to this, there are the energy contributions from exchange energy in ferromagnets, Zeeman energy and there is anisotropy, including magnetocrystalline anisotropy and shape anisotropy. In addition, the elements of electron spin resonance (ESR) and two-dimensional electron gas (2DEG) are described to provide an understanding of photovoltage detection of localised spin waves [35].

2.1 The Origin of Atomic Magnetic Moments

In an atom, magnetic moments arise from two types of electron motion. The orbital motion of the electron around the nucleus produces an orbital magnetic dipole moment. Rotation of the electron about its axis, known as spin, gives rise to a spin magnetic moment. An electron in motion around the nucleus may be considered as an electric current flowing in a closed loop without resistance. Accordingly, an electron with charge $-e$ and mass m_e, orbiting the nucleus with a velocity ν and orbital radius r, produces an orbital magnetic moment perpen-

dicular to the plane of the orbit. Physically, the orbital magnetic moment can be defined as $\mu_L = \gamma_L L$, where L is the total orbital angular momentum and is oriented opposite to the orbital magnetic moment (see Figure 2.1(a)). In 1925, Uhlenbeck and Goudsmit proposed that electrons additionally possess an intrinsic angular momentum, or spin, which creates a magnetic moment in the electron that interacts with an external magnetic field [36]. The electron spin and its magnetic moment are quantised, with two possible values that are often referred to as "spin-up" and "spin-down", shown in Figure 2.1(b). The definition of the spin magnetic moment is $\mu_S = \gamma_S S$, where S is the total spin angular momentum [37]. γ_L and γ_S are the gyromagnetic ratios, given by [38]:

$$\gamma_{L,S} = -g\mu_B/\hbar \tag{2.1}$$

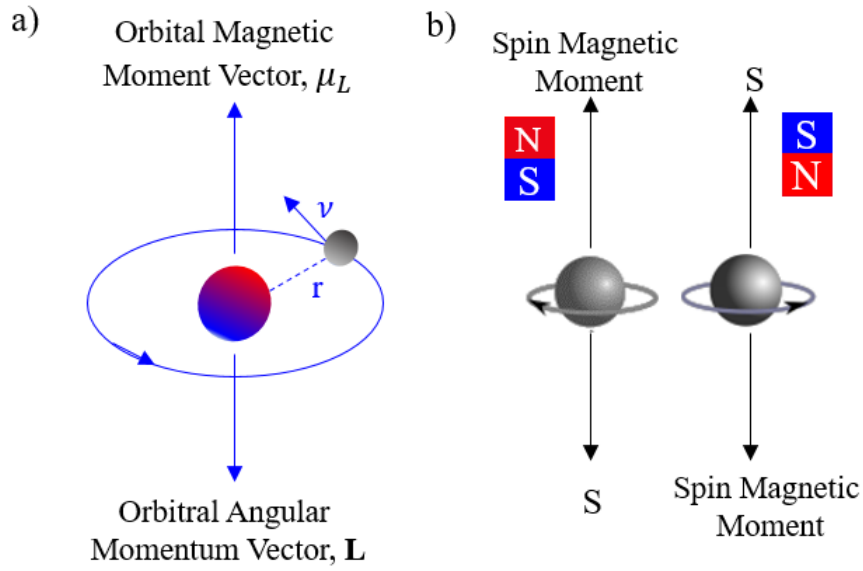

Figure 2.1 Schematic diagram of (a) orbital motion around the nucleus gives rise to an orbital magnetic moment with associated angular momentum, L. (b) spin of the electron around its own axis resulting in a spin magnetic moment with associated with angular momentum, S, for the spin-up and the spin-down.

where g is the Landé g-factor, $\hbar$ is Planck's constant, μ_B is the Bohr magneton which is $\mu_B = e\hbar/2m_e$. Figure 2.2 interprets the angular momentum coupling and the total angular momentum, J, which is a good quantum number for a multielectron atom:

$$\left.\begin{aligned} J &= S + L \\ L &= \Sigma_i l_i \\ S &= \Sigma_i s_i \end{aligned}\right\} \tag{2.2}$$

The general expression to define the total magnetic moment of the atom, μ_m, including spin and orbital angular momentum can be written as:

$$\mu_m = -\frac{g\mu_B}{\hbar} J \tag{2.3}$$

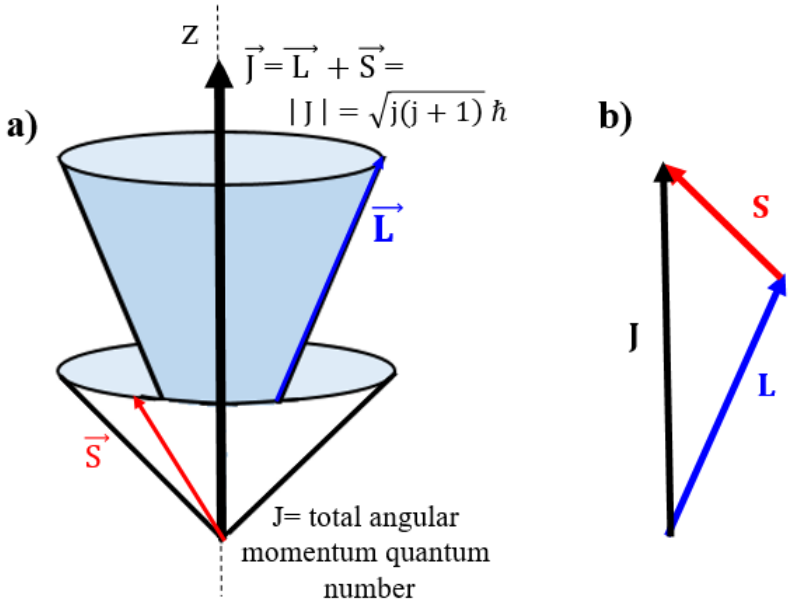

Figure 2.2 a) The total angular momentum, J, produced by combining the orbital angular momentum, L, and electron spin angular momentum, S.b) The vector model for the total angular momentum.

For defining the behaviour of magnetisation of metals, it is required to explain the magnetic response of the materials when subjected to an external magnetic field. Magnetic materials are traditionally classified into different groups: paramagnetic, diamagnetic, ferromagnetic, antiferromagnetic and ferrimagnetic [39]. Paramag-

netism and diamagnetism refer to non-magnetic materials, where the response to the applied field is very weak. However, in ferromagnetism, antiferromagnetism and ferrimagnetism, materials acquire a long-range magnetic order below the Curie temperature, T_C.

2.2 Classification of Magnetic Materials

Diamagnetism is a crucial characteristic of all materials in which the magnetisation opposes the applied magnetic field. Diamagnetism also has a negative and very weak susceptibility $\chi \approx -10^{-5}$ because of the induction of orbital currents and is slightly influenced by variations in temperature. Consequently, a very weak magnetisation is produced that opposes the applied magnetic field, directly manifesting Lenz's law: electrons in a magnetic field change their trajectory to induce a magnetic field that opposes the applied field. Most elements in the periodic table are diamagnetic such as copper, silver, and gold [1, 40, 41].

The paramagnetic materials typically have unpaired electrons in unfilled orbital shells giving a magnetic moment that is non-zero in response to the applied magnetic field. In the absence of the applied field, the magnetic moments are oriented randomly because the interaction between the magnetic moments and the neighbouring atoms is very weak [42]. When applying an external magnetic field to paramagnetic materials, the magnetic moments tend to align parallel to the external field, as shown in Figure 2.3. These materials also have a positive and small susceptibility that is typically $\chi \approx 10^{-3} - 10^{-5}$. Examples of paramagnetic materials are platinum and aluminium. The magnetic properties in diamagnetic and paramagnetic materials do not persist when the external magnetic field is removed.

Some materials containing permanent magnetic moments exhibit long-range order below the Curie temperature. There are several subtypes such as ferromagnets, antiferromagnets and ferrimagnets, and this study focuses on ferromagnetic materials. Because spontaneous magnetisation occurs a $B \simeq 0$, susceptibility of ferromagnets is much higher than 1 and values of $\chi \approx 50$ to $10,000$ are common e.g. in permalloy [43]. The most commonly used ferromagnetic materials consist

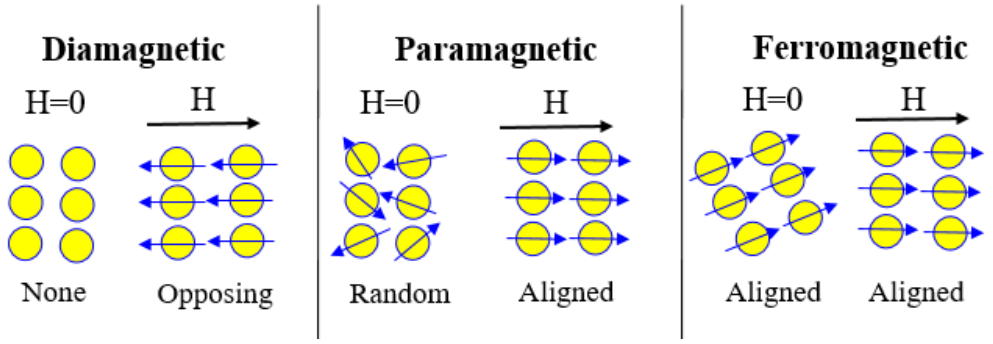

Figure 2.3 Graphical illustration of diamagnetic, paramagnetic, and ferromagnetic materials in the absence or presence of a magnetic field H.

of 3d transition metals. The magnetisation of the ferromagnetic system is higher than the external magnetic field because in such materials an effective internal field is keeping magnetic moments aligned. These magnets easily magnetised by applying a small external magnetic field. The magnetic properties of ferromagnetic materials also persist even without an applied magnetic field. When no magnetic field is applied, the magnetic moments remain spontaneously aligned up within tiny volumes called magnetic domains. But the domain acquire random magnetic orientation. In paramagnetic and thermal equilibrium, the orientation of the magnetisation of each domain is in a direction that reduces the magnetostatic energy.

When applying a magnetic field in ferromagnetic materials, magnetisation of each domain aligned parallel to the applied field, inducing a large net magnetisation. This effective magnetic field that gives rise to the spontaneous alignment of the magnetic moments is the exchange interaction. Exchange interaction is the microscopic contribution to the magnetisation of ferromagnetic materials and is discussed in detail in the next section. The response of a material to a magnetic field could be defined by magnetic susceptibility, as shown in the following equation [44, 45, 46]:

$$B = M_0 + \chi.H \tag{2.4}$$

Here, B is the induced magnetisation of the materials, M_0 is the spontaneous magnetisation when no field H is being applied, χ is the susceptibility a tensor for the isotropic materials.

Figure 2.4 illustrates the magnetisation curve of diamagnetic materials as the induced magnetisation is aligned antiparallel to the magnetic field. Consequently, the magnetic susceptibility in the diamagnets is negative. Furthermore, the response of the paramagnetic material to a magnetic field gives a magnetisation that is aligned parallel to the applied field. Accordingly, the paramagnet materials have a susceptibility that is positive.

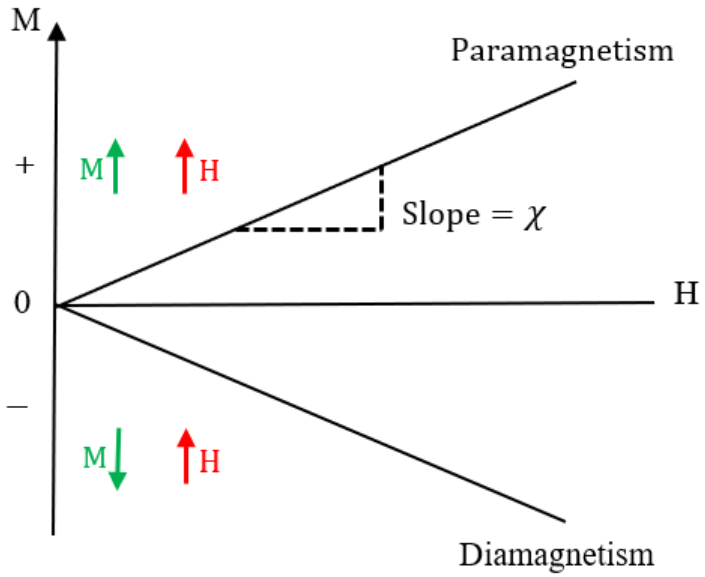

Figure 2.4 The M-H plots for diamagnetic and paramagnetic materials.

Weiss (1907) assumed that there is an internal magnetic field which is the exchange field, B_E, which acts to align the atomic moments even in the absence of an external magnetic field. The main assumption of this theory is that the exchange field is proportional to the induced magnetisation [1]:

$$B_E = \lambda M \tag{2.5}$$

where λ is a constant. At high temperatures, the exchange interaction competes with a thermal agitation, which destroys the magnetic order. Equation 2.4 can rewrite as:

$$M = \chi_p(B_a + B_E) \tag{2.6}$$

where B_a is an applied magnetic field. In addition, Curie's law expounds the paramagnetic susceptibility [47]:

$$\chi_p = \frac{C}{T} \tag{2.7}$$

Here, C is a constant for each material and known as the Curie constant while T is the absolute temperature in Kelvin. By linking Eqs. 2.5, 2.6 and 2.7, it is obtained:

$$M = \frac{CB_a}{T - C\lambda} \tag{2.8}$$

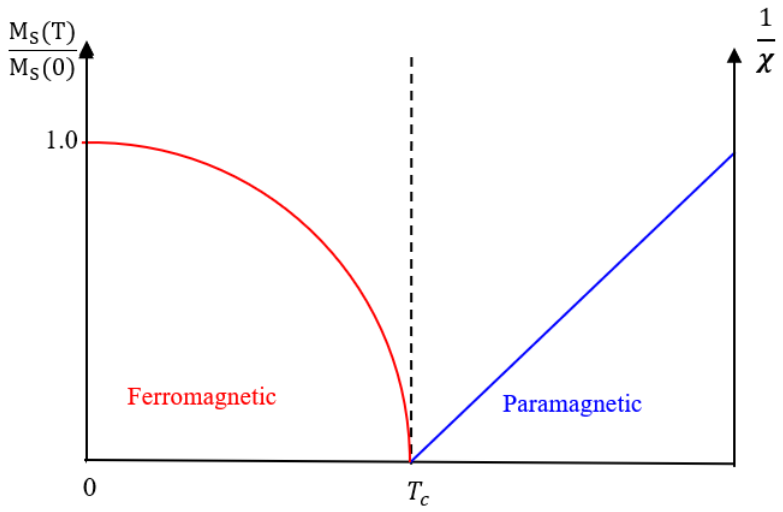

Figure 2.5 The Magnetisation and susceptibility curves of a ferromagnetic domain below and above the Curie temperature, T_C.

The influence of the temperature in this equation can be physically divided into different effects. As shown in the red curve in Figure 2.5, at low-temperature, $T < T_C$, the magnetic moments are aligned even without an external field applied, the magnetisation saturating at the maximum value and the magnetisation gradually decreasing until it reaches the Curie point. In contrast, by increasing the temperature, thermal energy is increased and destroys the spontaneous alignment of the magnetisation. Therefore, when $T = T_C$, the magnetic moments are completely destroyed. Additionally, the ferromagnetic materials become para-

magnetic in the presence of an applied field at temperatures above T_C where the susceptibility can be described by a Curie-Weiss law [48, 49].:

$$\chi = \frac{C}{T - T_C} \tag{2.9}$$

Figure 2.5 also displays a temperature-dependent susceptibility curve above the Curie temperature.

2.3 Exchange Interaction

The exchange interaction is a quantum mechanics effect that occurs between identical particles. It is the more robust magnetic interaction that gives rise to the parallel (ferromagnetic) or antiparallel (antiferromagnetic) spin alignment between neighbouring magnetic moments in materials. In ferromagnetism, the exchange interaction is essentially based on the Coulomb interaction between charges and the Pauli Exclusion Principle. The Pauli Exclusion Principle specifies that no two electrons within an atom can occupy the same quantum state. Each energy level contains a maximum of two electrons that must have opposite spins: 'spin-up and spin-down', Figure 2.6(a). In ferromagnets, two antiparallel ($\uparrow\downarrow$) spin pairs are not stable because Coulomb repulsion separates electron pairs. Electrons move away from each other, having the effect of stabilizing the parallel spin configuration [50].

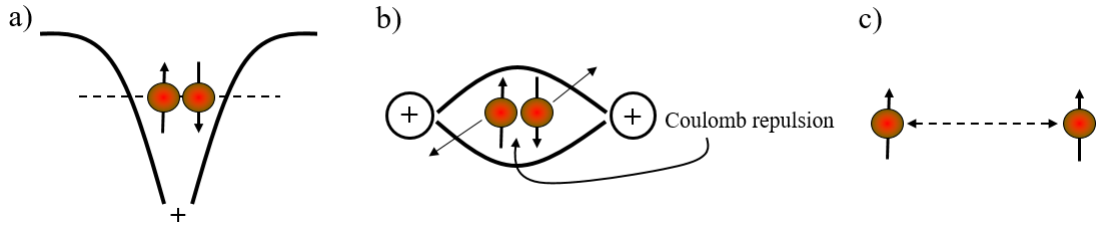

Figure 2.6 a) Pauli Exclusion Principle in He atom, b) Coulomb repulsion between electrons, c) The exchange interaction.

We now consider the simple case of having only two electrons with individual wavefunctions ϕ_1 and ϕ_2 that are confined over a double quantum well, which

refers to the quantum theory of magnetism. The total wavefunction for the two electrons system has a kinetic part and a spin part. The lower states of the double quantum well have bonding and antibonding wavefunctions, which are ϕ_B and ϕ_A, respectively, Figure 2.7. ϕ_B is the lower energy that has a symmetric exchange between the two electrons, $\phi_B = 1/\sqrt{2}(\phi_1 + \phi_2)$, while ϕ_A is the top one which is antisymmetrical, $\phi_A = 1/\sqrt{2}(\phi_1 - \phi_2)$. The total wavefunction ψ is formed by multiplying the kinetic wavefunction with the spin wavefunction. Because the electrons are fermions, the ψ is always antisymmetric concerning the exchange of the two electrons. This condition has been achieved using the following products: in the first case, there is a bonding state (symmetric) and spin singlet (antisymmetric) state, which the $\psi = \phi_B \otimes \Phi_{Singlet}$. The second case is the antibonding state (antisymmetric) and spin triplet (symmetric), which the ψ is $\psi = \phi_A \otimes \Phi_{Triplet}$.

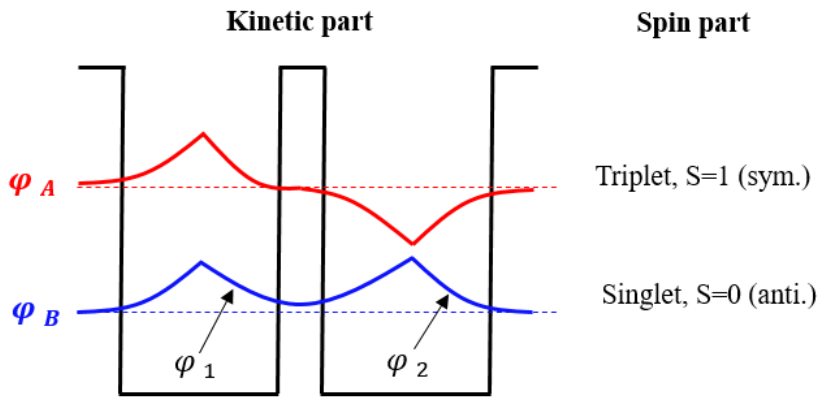

Figure 2.7 Two electrons with individual wavefunctions ϕ_1 and ϕ_2 confined by a double quantum well. The total wavefunction of the two-electron system has a kinetic part and a spin part.

We assuming the variation in the energies of the two states as E_B - E_A. This variation in the energies is an electrostatic term because of the exchange of two particles and is used to determine the exchange constant, which is a measure of the strength of the interaction:

$$J_{ex} = \frac{E_B - E_A}{2} \tag{2.10}$$

The value of the J, therefore, depends on the distance between interacting spins. The Heisenberg Hamiltonian gives a way to generalize the exchange interaction between two spins which are S_i and S_j are given by the [1, 51]:

$$E_{ex} = -(E_B - E_A)S_i.S_j = -2J_{ij}S_i.S_j \tag{2.11}$$

where J_{ij} is the exchange coupling constant. When $J_{ij} > 0$, the spins tend align parallel to one other, leading to ferromagnetism, which will be discussed later in more detail. Moreover, Stoner showed that when the gain from this exchange energy is bigger than the increase in kinetic energy from altering the band structure, spontaneous magnetisation will occur [52]. The magnetisation is stable when the product of the exchange is constant and the density of states at the Fermi surface $N(E_F)$ is higher than one and is recognized as the Stoner criterion [53]:

$$IJ_{ex}N(E_F) > 1 \tag{2.12}$$

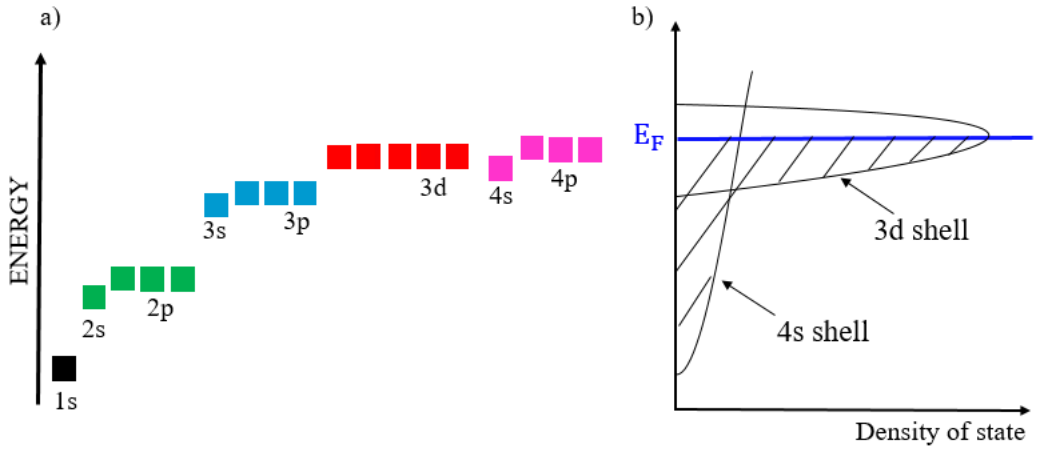

Figure 2.8 a) The electron configuration of cobalt is $1s^2 2s^2 2p^6 3s^2 3p^6 3d^7 4s^2$. b) The 4s band has a low density of states at the Fermi level while the 3d band has a higher density of states at the Fermi level.

where I is the exchange parameter. Because the value of exchange interaction $I \approx 1eV$ is similar for all 3d transition metals, the condition for ferromagnetic ordering depends on the $N(E_F)$ at a Fermi energy level. Consequently, in transition metals,

the 3d electrons are formed a small band structure that has a large density. This structure is complex inside the 3d band and indicates that only three elements Fe, Co and Ni have peaks in or near $N(E_F)$ that performs the Stoner criterion at room temperature [53, 54, 55]. This thesis focuses on Co, which has an electron configuration of $1s^2 2s^2 2p^6 3s^2 3p^6 3d^7 4s^2$. Theoretically, the 4s orbital has lower energy than the 3d orbitals because of that the 4s orbital will be filled first, then followed by all the 3d orbitals and the 4p orbitals as seen in Figure 2.8.

2.4 States of spin 1/2 particle in a.c magnetic field

To illustrate how spins evolve with time at magnetic resonance, electron spins are organized as either paramagnetic or ferromagnetic order or nuclear magnetic moments. The fundamental picture of a spin 1/2 particle in a uniform magnetic field must be revisited. Figure 2.9(a) shows the magnetic moment μ in Larmor precession when subjected to a static magnetic field, B_{dc}, that occurs when applied a static magnetic field to the spin. The magnetic torque can be described as $\tau = \mu \times B_{dc}$. The torque is equal to the rate of change of the angular momentum from the classical mechanics. This motion of the magnetisation in an effective field that was proposed by Bloch given by the following expression:

$$\frac{d\mu}{dt} = \gamma\mu \times B_{dc} \tag{2.13}$$

This equation explains the precession of the magnetic moment in the static field B_{dc}. When the static magnetic field in oriented along the z–axis, where the static magnetic field is $B_{dc} = B_0\hat{z}$, the tip of the magnetic moment vector will rotate in a circle around B_{dc} in the plane parallel to the x–y plane. Figure 2.9(a) illustrates the calculation of $d\mu$ when the magnetic moment vector travels through a small arc. The phase angle of the rotation that corresponds to $d\mu$ is given by ωdt. The angle of the cone outlined by the magnetic moment vector is θ and the radius of the magnetic moment can be specified mathematically as $\mu \sin\theta$. Accordingly, $d\mu = \omega dt\ \mu \sin\theta$; thus, by incorporating this result into Equation 2.13:

$$\gamma\mu \times B_{dc} = \omega\ \mu \sin\theta \tag{2.14}$$

Considering the angle θ that between μ and B_{dc} vectors, this term can be rewritten as:

$$\gamma\mu B_{dc} sin\theta = \omega\ \mu \sin\theta \tag{2.15}$$

Figure 2.9(a) shows ω_L, which is the frequency of precession that called Larmor precession, that could be described physically as ω_L=γB_{dc}. In contrast, the static magnetic field B_{dc} is called the Larmor field [56].

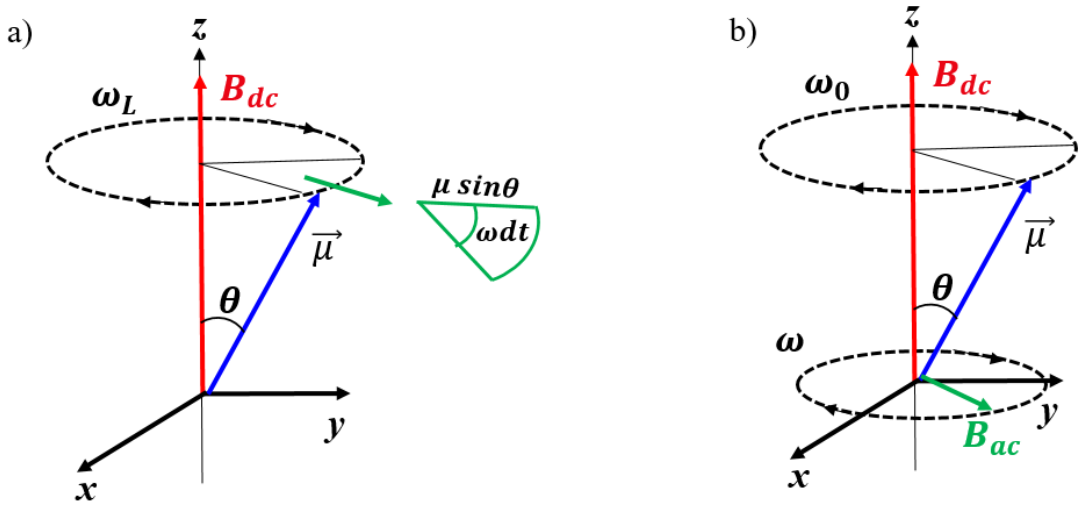

Figure 2.9 a) Schematic representation of Larmor precession of a single magnetic moment when subjected to a static magnetic field. b) Schematic shows the magnetic moment μ in the Larmor precession when subjected to crossed dc and ac magnetic fields.

This work also discusses the influence of a time dependence of B_{ac} that is applied perpendicular to the B_{dc}. As in Figure 2.9(b), B_{ac} is rotating in the x–y plane. The amplitude of B_{dc} is much larger than the amplitude of B_{ac}. Where the field with the specifications presented before, B_{dc}, is suitable to model a circularly polarised electromagnetic wave to irradiate a sample. The B_{ac} also induces an ac response from the magnetic moment. It can be replaced the field and magnetic moment in Equation 2.13 as a sum of the dc and ac components, which are μ_{dc} and μ_{ac}, and B_{dc} and B_{ac}. Because μ_{dc} and B_{dc} are parallel to the z–axis, $\mu_{dc} \times B_{dc} = 0$, and they can be neglected. Hence, Equation 2.13 can be rewritten as:

$$\frac{d\mu_{ac}}{dt} + \gamma\mu_{ac} \times B_{dc} = -\gamma\mu_{dc} \times B_{ac} \tag{2.16}$$

Introducing the complex variables to solve this equation which are:

$$\left.\begin{aligned}\dot{\mu}_{ac} &= \mu_{ac} exp(i\omega t)\\ \dot{B}_{ac} &= B_{ac} exp(i\omega t)\end{aligned}\right\} \tag{2.17}$$

By inserting Equation 2.16 in Equation 2.15, one find that [56]:

$$i\omega\mu_{ac} + \gamma\mu_{ac} \times B_{dc} = -\gamma\mu_{dc} \times B_{ac} \tag{2.18}$$

By projecting Equation 2.13 over the axes of a Cartesian coordinate system, one obtain:

$$\left.\begin{aligned}i\omega\mu_{ac.x} + \gamma B_{dc}\mu_{ac,y} &= \gamma\mu_{dc}B_{ac,y}\\ -\gamma B_{dc}\mu_{ac,x} + i\omega\mu_{ac,y} &= -\gamma\mu_{dc}B_{ac,x}\\ i\omega\mu_{ac.z} &= 0\end{aligned}\right\} \tag{2.19}$$

So, the solution of the system maybe rewritten as:

$$\left.\begin{aligned}\mu_{ac.x} &= \chi B_{ac,x} + i\chi_a B_{ac,y}\\ \mu_{ac.y} &= -i\chi_a B_{ac,x} + \chi B_{ac,y}\\ \mu_{ac.z} &= 0\end{aligned}\right\} \tag{2.20}$$

Hence χ and χ_a are the magnetic susceptibility components of the high-frequency and are defined by:

$$\left.\begin{aligned}\chi &= \frac{\gamma\mu_{dc}\omega_L}{\omega_L^2 - \omega^2}\\ \chi_a &= \frac{\gamma\mu_{dc}\omega}{\omega_L^2 - \omega^2}\end{aligned}\right\} \tag{2.21}$$

Thus, the fundamental idea of this study is that at resonance absorption of electromagnetic energy by the system, the Larmor frequency ω_L matches the frequency of the ac magnetic field.

Figure 2.10 illustrates the energy levels for a nucleus with spin quantum number S= 1/2 showing the Zeeman splitting. The quantisation of the energy levels of an electron is due to the quantum mechanical nature of the electron spin. If there is no magnetic field, the spin-up and spin-down levels are degenerate with no difference

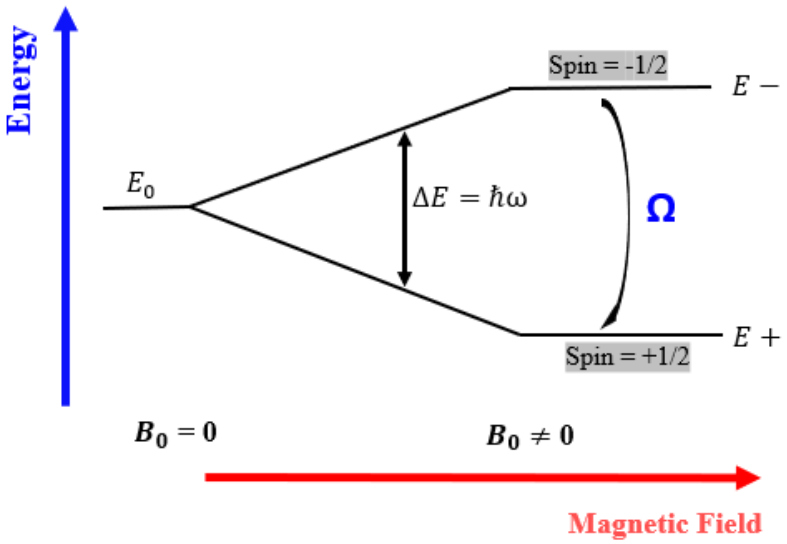

Figure 2.10 The Zeeman splitting and the energy difference between s = +1/2 and s = -1/2, which is proportional to the external magnetic field and given by ΔE = $\hbar\omega$.

between spin orientation. In contrast, when the external magnetic field is applied, $B_0 \neq 0$, the spin will split into two different states: spin-up $S = +1/2$ (parallel) and $S = -1/2$ spin-down (antiparallel) to the line of the external magnetic field and each level has a particular energy because of the Zeeman Effect. There are two states that are equally displaced from the original energy state and the gap between them is related to the energy corresponding to the frequency where the resonant absorption happens in the example explained in Section 2.4, $\Delta E = \hbar\omega_L$, where $\omega_L = \gamma B_0$. So, this split is proportional to the external magnetic field strength, B_0. Accordingly, the energy of states given as follows:

$$\Delta E = \hbar\omega = g\mu_B B_0 \tag{2.22}$$

where μ_B is the Bohr magneton which is used assuming the $S = 1/2$ particles are electrons, g is the g-factor. The g-factor in the case of $GaAs$ is about $g = -0.44$, that means the spin-up has a lowest energy. At resonance, the difference in the energy of the electron allows microwave radiation to be absorbed and appears at a resonance line in the absorption spectrum that might be measured. Furthermore, the spin system oscillates between both energy states to form the Rabi frequency

of $\Omega = \gamma B_{ac}$. However, this project focuses on the spectroscopy of confined spin waves and must be treated quantum mechanically. [57].

2.5 Shape anisotropy

Shape anisotropy is an important phenomenon to describe the anisotropy that depends on the shape of the specimen. Shape anisotropy appears in small magnetic materials and could be divided into two kinds of specimens: when the sample is spherical, the constant magnetic field magnetises the sample to the same extent in any direction. The parallel orientation is no different from the perpendicular for symmetry. However, when the specimen is not spherical, it magnetises along their long axis, as will be shown later. This section explains that the shape of the sample plays an important role [1, 56].

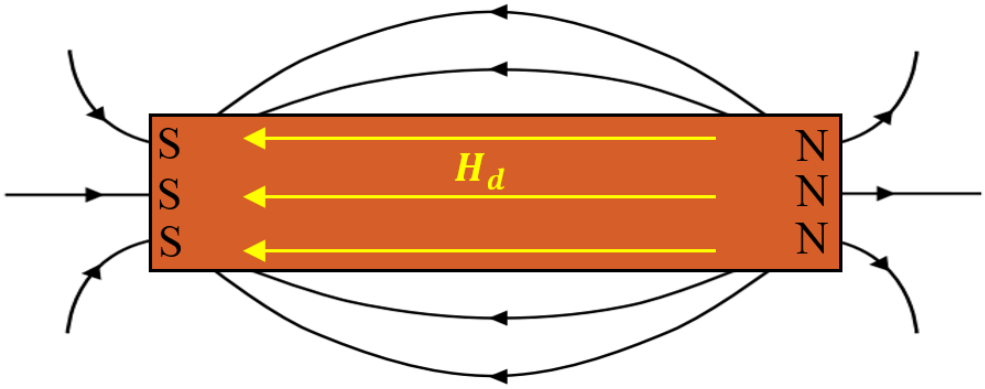

Figure 2.11 Stripe magnetised from left to right and will produce the magnetic poles at each end of a bar magnet. These poles induce a demagnetising magnetic field, H_d, with the opposite direction concerning the magnetisation and magnitude proportional to the magnetisation.

In addition, the formation of spin waves of the confined system relies on quantum mechanics and classical magnetisation. The magnetostatic potential of the demagnetising field produces the boundary conditions which generates discrete levels in the potential well. The origin of this demagnetisation field arises from the magnetic field that is applied to a bar magnet from left to right, as it was shown in Figure 2.11. The magnetisation within the sample is formed in the same direction

as the applied field. Thus, the magnetic poles create north and south poles at the boundaries. In addition, the north and south poles create a demagnetisation field H_d in the opposite direction to the magnetisation, minimizing the total magnetic field inside the magnet. The demagnetising fields are very important in the ferromagnetic materials because of the strong magnetisation which is close to saturation point, that leads to the strong demagnetising fields as well. However, the formation of the demagnetisation fields leads to define the shape anisotropy by starting with the basic relationship of the magnetic flux density in the magnet which is:

$$B = \mu_0(H + M) \tag{2.23}$$

where H is the magnetic field strength. By taking the divergence of this equation and calculate the divergence of the magnetisation:

$$\nabla \cdot M = \frac{\nabla \cdot B}{\mu_0} - \nabla \cdot H \tag{2.24}$$

Physically, It is known as $\nabla.B = 0$, from the Maxwell's equations. That leads to this equation:

$$\nabla \cdot H = -\nabla \cdot M \tag{2.25}$$

In effect, for the divergence of magnetisation, there is also a magnetic field inside the magnetic materials that is in the opposite direction to the magnetic moments that work to preserve the condition with no divergence in B and reduce the magnetic field inside the sample. The total internal field felt by the spins within the sample can be expressed as:

$$H_i = H_e + H_d \tag{2.26}$$

where H_e is the applied magnetic field and H_d is the demagnetisation field which could be explained as: $H_d = -NM$. Here N is the shape-dependent demagnetising tensor that is large along the short axis and close to zero along the long axis,

as follows [58]:

$$N = \begin{bmatrix} N_x & 0 & 0 \\ 0 & N_y & 0 \\ 0 & 0 & N_z \end{bmatrix} \tag{2.27}$$

Thus, the total field is smaller than the applied field. There is also energy associated with demagnetisation field, as given by the following:

$$E_d = -\frac{\mu_0}{2} \int_V M \cdot H_d dV \tag{2.28}$$

However, the demagnetisation factor considers the effect of sample shape through the magnetic charges resulting from the termination of lines of M at the surface of the sample. In other words, the dc components of the total magnetic field are crucial to rewriting the motion equation and calculating the shift in the resonance condition. Considering the dc component of the total magnetic field working on the spin, the motion equation can be expounded as a function of the dc component of the applied magnetic field, H^e_{dc}:

$$H^i_{dc} = H^e_{dc} - NM_{dc} \tag{2.29}$$

Hence, the H^i_{dc} is the is the dc component of the applied magnetic field, but the ac component of the internal field can be ignored because determining the magnetic response to an ac magnetisation is not important. A modification to Equation 2.16 must include the internal field given through Equation 2.29. There is also the vector result between the dc magnetisation and the dc internal field which are parallel to the z–axis, providing the following:

$$M_{dc} \times (H^e_{dc} - NM_{dc}) = 0 \tag{2.30}$$

consequently:

$$\left.\begin{aligned} i\omega M_{ac,x} + \gamma\mu_0(H^e_{dc} - N_z M_{dc} + N_y M_{dc}) M_{ac,y} = 0 \\ -\gamma\mu_0(H^e_{dc} - N_z M_{dc} + N_x M_{dc}) M_{ac,x} + i\omega M_{ac,y} = 0 \end{aligned}\right\} \tag{2.31}$$

The frequency of the oscillations is could be presented by solving equation 2.31, therefore [1]:

$$\omega_0 = \gamma\sqrt{[H_{dc}^e + (N_y - N_z)\mu_0 M_{dc}][H_{dc}^e + (N_x - N_z)\mu_0 M_{dc}]} \tag{2.32}$$

Ferromagnetic resonance occurs when the frequency of the ac magnetic field is equal to the frequency of free oscillation in Equation 2.32. In this thesis, the sample experimentally used the rectangular prisms. However, the demagnetisation factors an infinitely long stripe with a rectangular cross-section aspect ratio of $k = h/d$, as shown in Figure 2.12. The demagnetisation factors are $N_z = 0$ and could be calculated by these formulae [3, 59, 60]:

$$N_x = \frac{1}{\pi k}\ln\left(\frac{1}{\sqrt{1+k^2}}\right) + \frac{k}{\pi}\ln\left(\frac{\sqrt{1+k^2}}{k}\right) \tag{2.33}$$

$$N_y = \frac{k}{\pi}\ln\left(\frac{k}{\sqrt{1+k^2}}\right) + \frac{1}{\pi k}\ln\left(\sqrt{1+k^2}\right) + 1 - \frac{2}{\pi}\arctan k \tag{2.34}$$

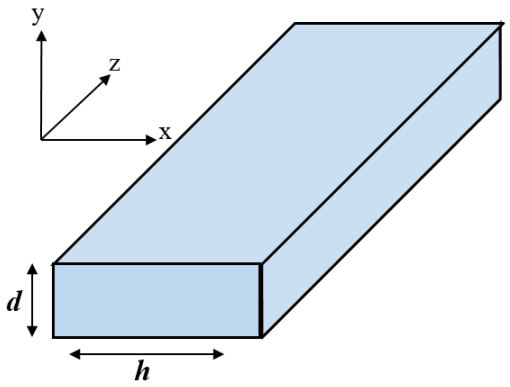

Figure 2.12 Schematic of dimensions, d and h, corresponding to the stripe width, stripe and thickness.

2.6 Magnetic Properties of Ferromagnetic Materials

2.6.1 Magnetisation Process in the Presence of Magnetic Domain

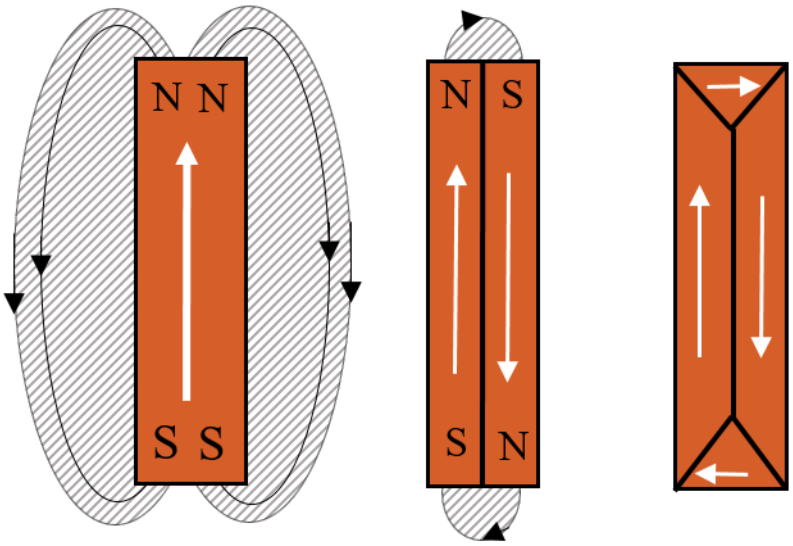

Figure 2.13 Schematic diagram of (a) A single ferromagnetic domain with a sizeable magnetostatic field. (b) Two ferromagnetic domains in order to reduce the magnetostatic field. (c) Four domains, the closure domains at the ends make the magnetostatic energy zero.

From the study of the ferromagnetic materials, the magnetisation of the material depends on both the applied magnetic field and temperature, as shown in Figure 2.5. When the temperature is below the Curie temperature, spontaneous alignment occurs. The material may manifest very small or no magnetisation because of the magnetic domains. Furthermore, the magnetostatic energy is partially accountable for the formation of magnetic domains. Figure 2.13 illustrates that the magnetostatic energy is lowered as magnetic domains form. In the first case, which is the single ferromagnetic domain, the lowest exchange energy is when the spins are parallel to each neighbouring magnet. This configuration also has a large amount of magnetostatic energy. In the second case, the sample is separated into two domains. The north and south pole are behind each other on the top and

vice verse in the bottom. This case has a lower magnetostatic energy than the single domain. There is no demagnetisation field created from south to north, but the field is confined in the two ends. The third case describes the sample that is subdivided into four domains. Therefore, the closure energy at the end has zero magnetostatic energy.

2.6.2 Hysteresis Curve

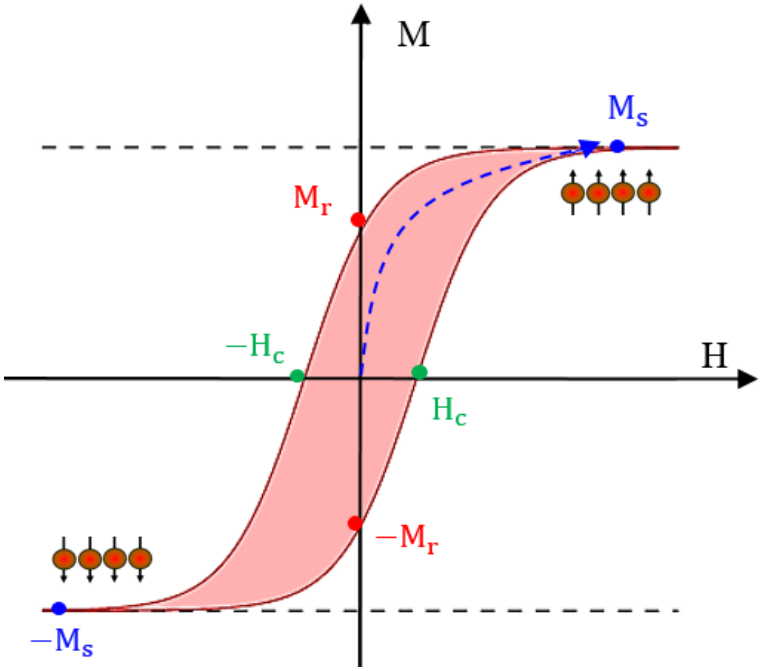

Figure 2.14 The Magnetic hysteresis loop M-H of the ferromagnetic materials.

However, ferromagnetic materials exhibit memory effects in their M(H) dependence. This property is observed as a hysteresis loop, which is one of the most common ways of characterising the magnetic properties of ferromagnetism. Extensive information about the magnetic materials can be obtained by studying its hysteresis loop. In Figure 2.14, the specimen is assumed to be unmagnitised at the centre of the graph (H = 0, M = 0). As a positive magnetic field is applied to the specimen, the magnetic moments align uniformly in the direction of the applied magnetic field until the magnetisation saturation point, M_s, is reached. When the applied magnetic field is reduced to zero, the magnetisation curve returns to a point known as the remanent magnetisation, M_r. Some magnetic flux

remains in the material even although the magnetising force is zero. By applying a magnetic field in the negative direction, the magnetisation may be reduced to zero: the corresponding field is called coercivity, -H_c. As the magnetising field is increased in the negative direction, the material again becomes saturated in the opposite direction, -M_s. Two classes of materials exist, depending on the coercivity: soft magnetic materials (small coercivity) are easy to magnetise and demagnetise, while the magnetic materials that are difficult to demagnetise are called hard magnetic materials (large coercivity). Moreover, reducing H to zero causes the curve to remnant magnetisation point which is in the negative direction -M_r. Then, Increasing the magnetic field back in the positive direction will return M to zero to reach the coercivity point again but in the positive direction, H_c. This curve will not return to the centre point because some force is required to remove the residual magnetism. Thus, it will complete the hysteresis loop by reaching the saturation point which is in the positive direction, M_s. Besides, the shape and size of the hysteresis loop largely depend on the nature of the magnetic material.

2.7 Dynamic Phenomena

2.7.1 Bulk Magnon Dispersion Relation

This section presents the analysis of the one-dimensional array of a chain of N magnetic moment. This system has energy that is a sum of the exchange interactions between the nearest neighbours of magnetic moment and is described by the Hamiltonian. The Hamiltonian is based on the Heisenberg model, which describes the energy of interaction between two magnetic moments. Equation 2.11 could be also rewritten between many neighbouring atoms as:

$$E_{ex} = -2J_{ex} \sum_{p=1}^{N} S_p . S_{p+1} \tag{2.35}$$

Here, S_p is the angular momentum of the magnetic moment p, while S_{p+1} indicate the closest neighbour of the magnetic moment p.

However, at the ground state in the ferromagnetic, all magnetic moments are parallel; in such state, $S_p \cdot S_{p+1} = S^2$, as shown in Figure 2.15(a). The exchange energy of this system can be identified as: $E_0 = -2NJS^2$. However, when one magnetic moment is reversed in the array, the energy for this state is higher by $8JS^2$ than the energy of the ground state, Figure 2.15(b). The energy of this state also is more efficient energetically when all of the magnetic moments participated in the excitation. Indeed, the orientation of the magnetic moments oscillates as an oscillatory system coupled by the exchange interaction, these systems are called magnons, Figure 2.15(c). The energy of this state is much lower than in Figure 2.15(b). In bulk, the spin-wave dispersion relation in a one-dimensional array with the nearest neighbour interaction is given by the following [43, 61]:

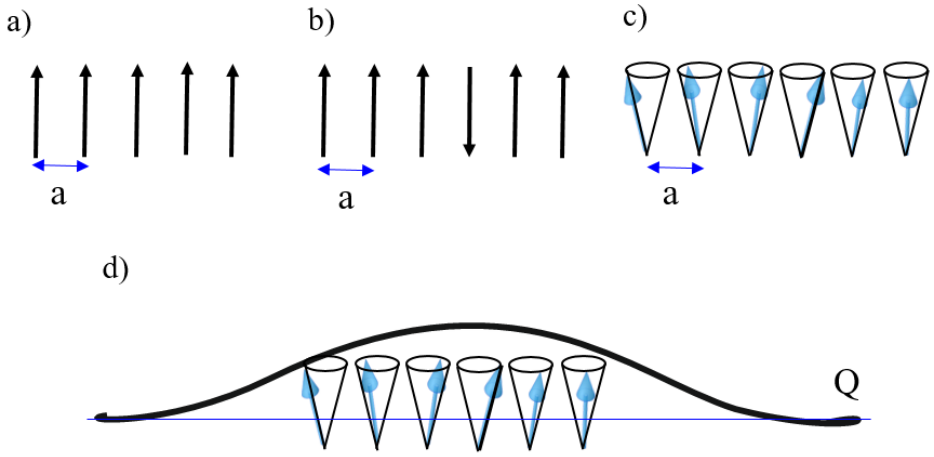

Figure 2.15 a) A classic picture of a ferromagnet. (a) The ground state of the magnet: all spins are aligned. (b) The excited state of the magnet: one spin is reversed. (c) The magnon state: a spin-wave on a line of spins and the spins vied in perspective. d) A spin-wave propagates along Q.

$$\hbar\omega = 4JS(1 - cos(ka)) \tag{2.36}$$

where ω is the frequency, k is the wavevector of the spin wave and a is the lattice constant. Equation 2.36 is plotted in Figure 2.16, which shows the dispersion relation that corresponds to the spin procession around the magnetisation direction in the specific range of k within a range of $0 \leq k \leq \pi/a$.

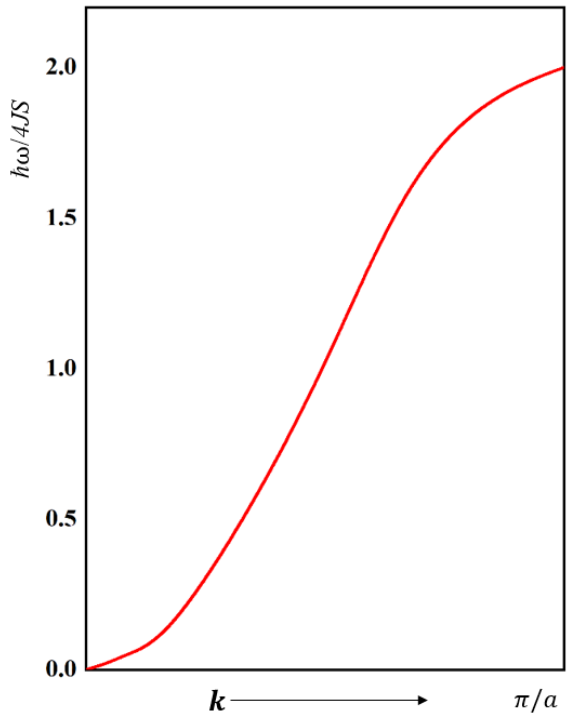

Figure 2.16 The dispersion relation for magnons in a ferromagnet in one dimension. Adapted from ref [1].

2.7.2 Localised Spin Wave Excitations

2.7.2.1 Damon-Eshbach Modes

Understanding the discrete modes of magnetic excitations of ultra-small magnets where surface effects play a dominant role is essential for both fundamental science and applications to high-density information storage. The collective dynamics of submicron magnets, which is the most interesting, is currently inaccessible by any standard methods such as Brillouin light scattering.

Brillouin light scattering is one of the most significant techniques to investigate the dynamic properties of magnetic materials [10, 11, 62]. Most importantly, BLS gives information on energy losses incurred at momentum $q = k$ - $\acute{k}$ where k and $\acute{k}$ are the wavevectors of the incident and scattered photons, Figure 2.17. In this way, the energy-momentum $\omega(q)$ dispersion curves of magnons can be measured. However, this technique can be understood as an inelastic scattering process of incident photons with spin wave (magnon) that considers energy and momentum

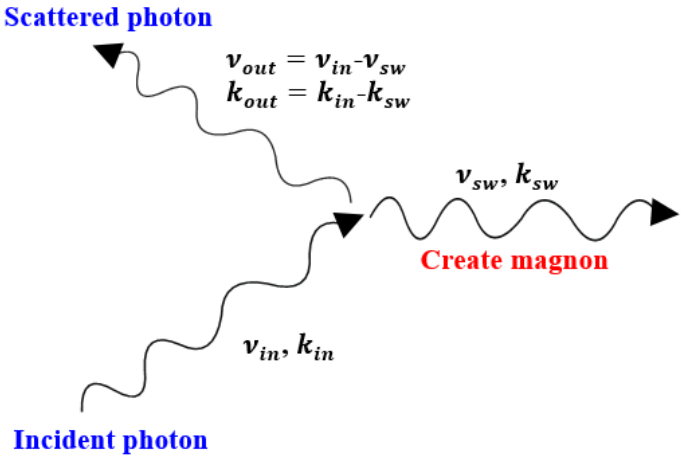

Figure 2.17 a) Scheme of inelastic scattering of an incident photon by a magnon. The incident light (in) creates a spin-wave (sw) in the Stokes process. The conservation of energy and momentum lead to a reduced wave vector and a smaller frequency of the scattered light (out).

conservation which decreases the k_{out},ν_{out} directly of the light which is scattered in the Stokes process [63]. This technique could be described by these equations:

$$h\nu_{out} = h\nu_{in} \pm h\nu_{sw} \tag{2.37}$$

$$\hbar k_{out} = \hbar k_{in} \pm \hbar k_{sw} \tag{2.38}$$

Here, h is the Planck's constant and ν is the frequency. (in) to the incident light whereas the scattered light (out) that carries information about the spin wave (sw).

Figure 2.18 illustrates the typical BLS spectrum for wavevector $q = 0.59 \times 10^5$ cm^{-1}, which is along the width and the external field $H_e = 100$ Oe, which is along the length of the stripe. Nevertheless, it could be observed that several peaks correspond to different quantised modes (m=1, 2, 3...) relative to the different frequencies. That result occurs by sending the light to excite the spin wave which is scattered to obtain the spin mode at room temperature, $T_R \gg \frac{\hbar\omega}{k_B} \approx 1K$.

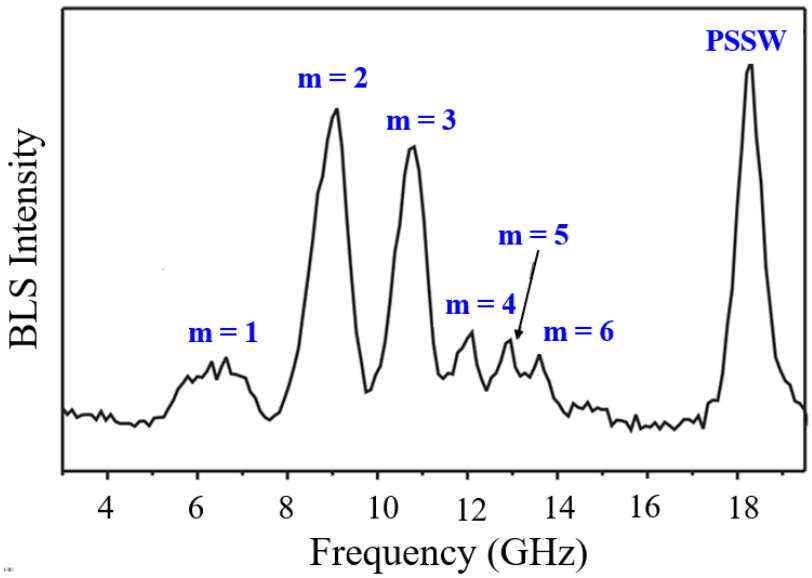

Figure 2.18 BLS spectrum of $1\mu m$ wide and 33 nm of thick stripes for rectangular elements in an external field of 100 Oe for a transferred wavevector of q = $0.59\times10^{5}cm^{-1}$ oriented along the width of the stripe. Adapted from ref [2].

The description of BLS technique is related to the photovoltage technique, which is the key idea in this thesis. Clearly, BLS is working very well for magnets of a size comparable to the optical wavelength (the wavelength of the laser beam being scattered $\sim$ 532 nm). In contrast, photovoltage spectroscopy is a powerful technique for probing magnetic excitations on a scale lower than 100 nm and this technique can also measure the dispersion curve of spin waves [64]. In this project, this aspect does not matter because the momentum of spin waves is strongly quantized by the boundary conditions of tiny magnets [65, 66, 67].

During the long stripes, two different geometries might be studied, allowing us to examine two different effects separately. Through the first kind of an infinite film, magnetic resonance is underpinned by a backward volume wave mode. In this case, the applied magnetic field is along the length of the magnetic stripe. The internal magnetic field is homogeneous and equal to the magnetic field which was applied. Therefore, the magnetostatic boundary conditions force spin-wave modes to the surface of magnets. The stripe then exhibits a backward volume mode modulated by Damon–Eshbach modes, which propagate along the edges parallel to the external magnetic field [2, 24, 25, 68].

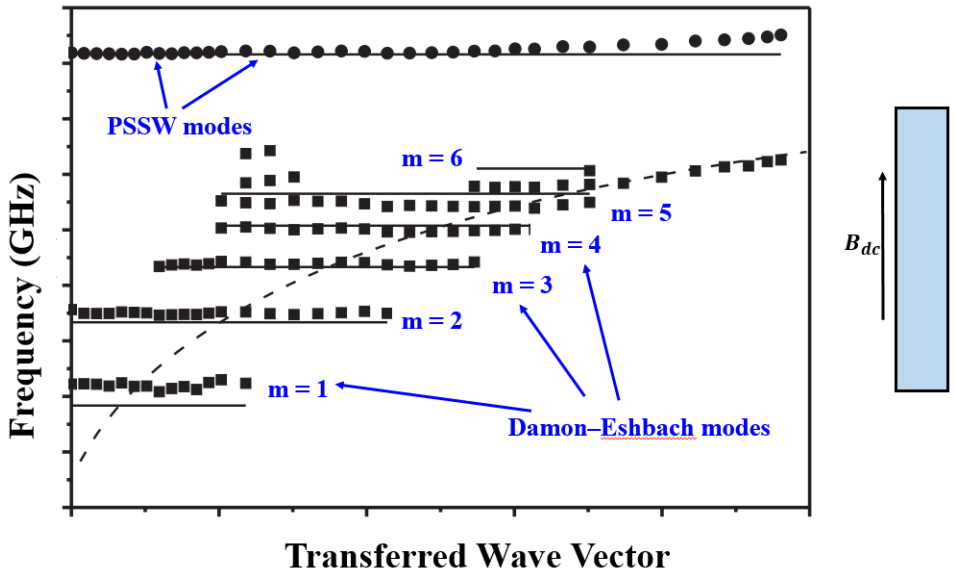

Figure 2.19 Measured dispersion relation of a thick stripe in an external field, B_{dc}, of 100 Oe applied along the length of the stripe. Adapted from ref [2].

Figure 2.19 illustrates the measurement of frequencies as a function of the wavevector at circle points that show a frequency of 18.5 GHz where the circles identify the perpendicular standing spin wave modes (PSSW). In addition, the squares correspond to the Damon–Eshbach modes which could be determined at low frequency and are quantized because of confinement caused by the finite stripe width.

2.7.2.2 Spin wave wells in transversely magnetised magnetic stripes

During this study, the spin waves propagation is identified in the rectangular sample, which is infinitely long. This sample is magnetised with an applied field in the plane and along the width of the thin stripe. There is a strong inhomogeneous internal field, particularly at the edges of the bar magnets wherever the poles are formed as a result of a demagnetisation field which is strong. The internal field induces the propagation of spin waves at the region where the field gradient is steeper. The strong inhomogeneous internal magnetic field introduces the confinement of the spin wave in the magnetic stripe [2]. Figure 2.20 shows the dipolar edge spin waves confined in wells of magnetic field near magnetic poles [69].

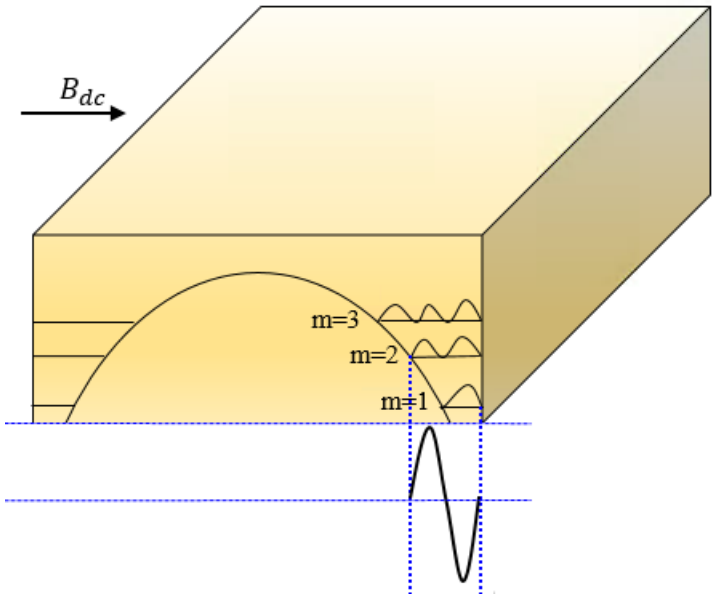

Figure 2.20 The dipolar edge spin-waves confined in wells of magnetic field near magnetic poles, the spatial profile of the magnetic field induced by DESWs at the site of the 2DEG [2]. The wave below the magnet is the spin wavefunction of the m = 2 level. The dashed line gives the width of the quantum well at the site of the m = 2 level.

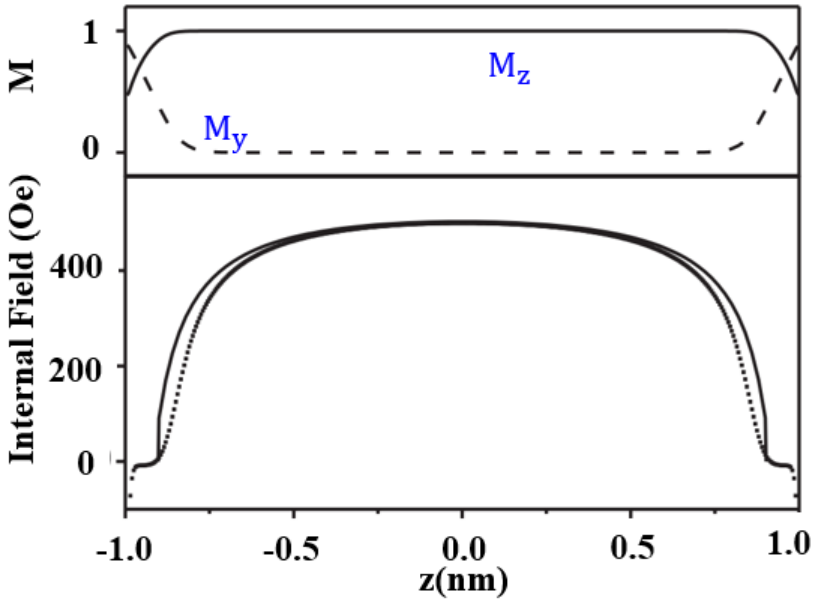

Figure 2.21 The Magnetisation components M_y and M_z along the width of the stripe (top). The full line is the internal field along the width of the stripe (bottom) and the dotted line is the output for the effective field of OOMMF simulation. Adapted from ref [2].

Figure 2.21 presents the internal field profile as a function of z–direction. The internal field is a maximum and broad at the centre of the stripe and the magnetisation is saturated and aligned with the internal field. In contrast, at the edge, the field is almost zero, and the magnetisation is no longer saturated; therefore, magnetic domains are created at the edge. On the other hand, the strong inhomogeneity affects the propagation of spin waves significantly via creating the well which confines spin waves. The spin-wave modes have different characteristics depending on the region of the inhomogeneous, potentially identifying the different types through Brillouin light scattering experiments (BLS).

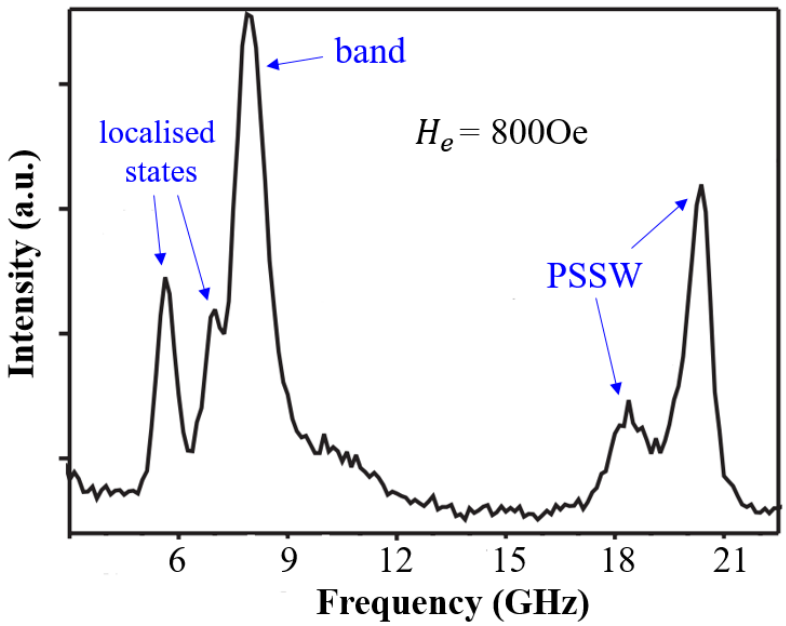

Figure 2.22 The spectra of BLS for a magnetic stripe that magnetised transversely, with an applied field 800 Oe. It shoes the PSSW modes at high frequency at 20 GHz, the band of spin wave modes corresponding to a band of resonances of nonlocalised spin-wave modes when decreasing the frequency (8 GHz) and the peak corresponds to the resonance of a localised mode confined in the spin-wave well at low frequency.This data refers to Bayer et al [2].

Figure 2.22 shows the spectrum of BLS at different frequencies. As shown, at high frequency (20 GHz), there are two peaks corresponding to two perpendicular surface spin-wave modes (PSSW) [70]. One of the peaks is placed at the centre of the stripe and another is placed nearly at z = ± 0.5 nm. When the frequency has decreased, it can be observed at (8 GHz), which corresponds to a band of

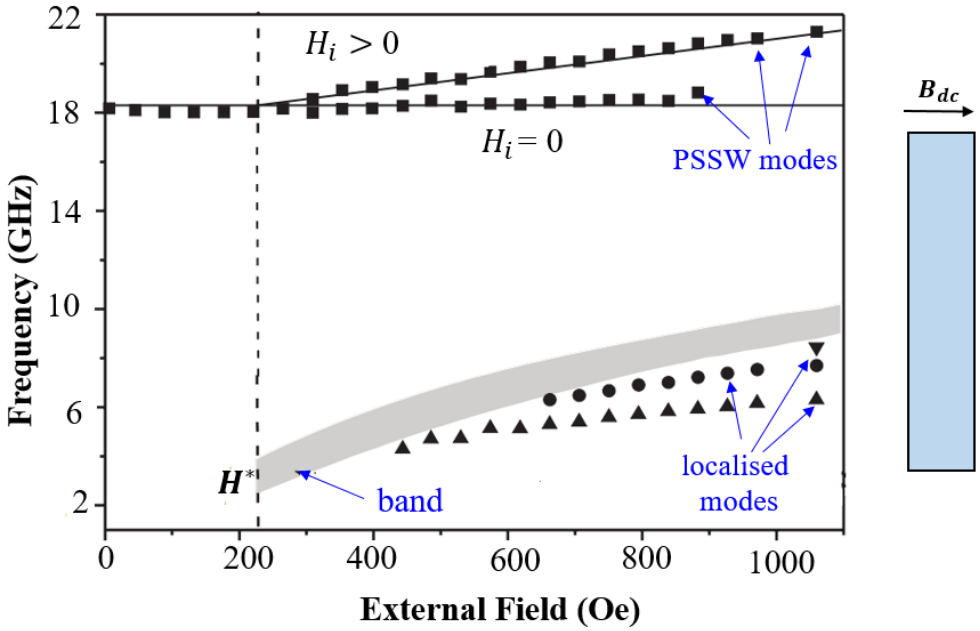

Figure 2.23 The frequency of the spin wave modes as a function of an applied magnetic field. The vertical dashed line indicates the critical field H^*. Adapted from ref [2].

resonances of nonlocalised spin-wave modes. However, at low frequency, the peak corresponds to the resonance of a localised mode confined in the spin-wave well with an applied field of $H_e = 800Oe$.

Figure 2.23 establishes the relation between the external field and the frequency which shows the several types of spin-wave modes. When increasing the applied field, the number of localised modes also increase and these modes shift from a low frequency to a higher frequency as seen in the bottom of Figure 2.23. Below the H^* value, where the field is not adequate to reach the saturation magnetisation point at the middle of the magnet there is a single PSSW mode only that specifically corresponds to $H_i = 0$. Besides, at H^*, the peak divides into one that is located at a high frequency where the magnetisation is saturated. The peak which is at a low field maintains its frequency while the frequency of the other PSSW mode increases with an increasing applied field.

For determining the localisation of spin waves as a function of frequency, the internal field needs to be calculated according to the following equation:

$$H_i = H_e + H_d + H_{MC} \tag{2.39}$$

Herein, H_e is the applied field, H_d is the demagnetising field and H_{MC} is the magnetocrystalline anisotropy field and will be described in the next section. The dispersion law for dipolar-exchange spin waves has a wavevector q parallel to the magnetic field in a thin film following the method of [71, 72, 10]:

$$\left(\frac{\omega}{\omega_M}\right)^2 = \left(\frac{\omega_H}{\omega_M} + \alpha q^2\right)\left[\frac{\omega_H}{\omega_M} + \alpha q^2 + 1 - \frac{1 - exp(-qh)}{qh}\right] \tag{2.40}$$

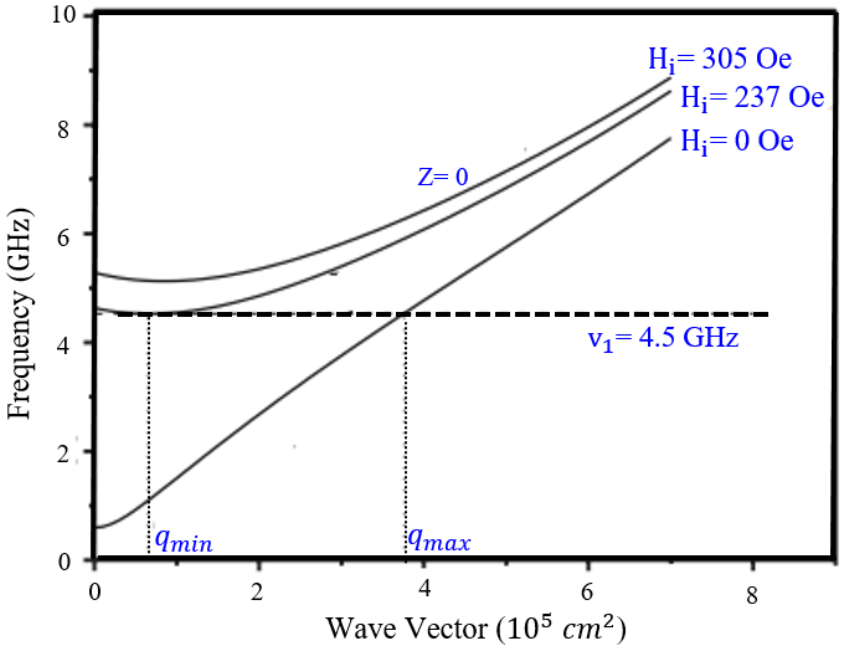

Figure 2.24 Dispersion curve of the spin waves at constant internal fields, which is an external field $H_e = 500$ Oe. $H_i = 0$ Oe and $H_i = 237$ Oe as a function of wavevector, q. Adapted from ref [2].

Hence, $\omega_M = \gamma\mu_0 M$, $\alpha = 2\pi A/\mu_0 M_s^2$ is the exchange constant expressed as a function of the effective area A, and $\omega_H = \gamma\mu_0 H_i$ is the Larmor frequency of the internal magnetic field. H_i is the internal field including B_{dc} and the demagnetising field where $M(z)$ is the stray magnetic field. Afterwards, the wavevector q has two quantised components, q_y and q_z, and a third free component, q_x. Where

$q_z = p\pi/h$ (p =1,2,...) is quantised by the finite thickness of the Co film while wave vector q_y is confined by the spatial variation of the internal magnetic field. Once ω_H is slightly smaller than the microwave frequency, ω, Equation 2.39 admits real solutions in q at the centre of the stripe which correspond to propagating waves, although, if the solution is imaginary, then the spin-wave is evanescent and this gives quantum wells for spin waves in spatially varying B-field [73, 74].

The dipolar surface spin-waves, therefore, propagate at the side of the poles where the internal magnetic field is the lowest. The quantisation of the spin-wave frequency, ω, results in a series of small peaks associated with localised edge spin waves [75, 76]. As long as, ω^2 is proportional to q^2 (where $q_n = 2\pi n/h$) ω must be proportional to q, which explains why the curve shown in Figure 2.24 becomes linear at shorter wavelength.

2.8 Magnetocrystalline Anisotropy

Understanding the magnetic anisotropy of ferromagnetic materials plays a dominant role in the magnetisation curves and ferromagnetic resonance spectra. The magnetic anisotropic, which is the most interesting, is determined by the field required to tilt the magnetisation from the easy axis to the hard axis. Anisotropy is also determined by the shape. Figure 2.25(a) shows the relation between the saturation magnetisation, M_s, and anisotropy field, H_K, in the hard axis hysteresis loop [1].

This study explains that in the typical situation with no magnetic field has been applied, $H = 0$, the magnetisation tends to align at the easy axis, $\alpha = 0$. Instead, when the applied field is increased, the magnetisation is closer to an applied magnetic field, as shown in Figure 2.25(b). Consequently, an external field must be applied to orient the magnetisation vector in the opposite direction. The applied magnetic field required to obtain the saturation magnetisation over the easy axis which is lower than the other axis while it is higher along the hard axis. Each material has a different easy axis [29]. The observed phenomena can be described by the spin-orbit interaction of electron and this interaction is modified depending on the orientation and affects the energy in the magnetisation process

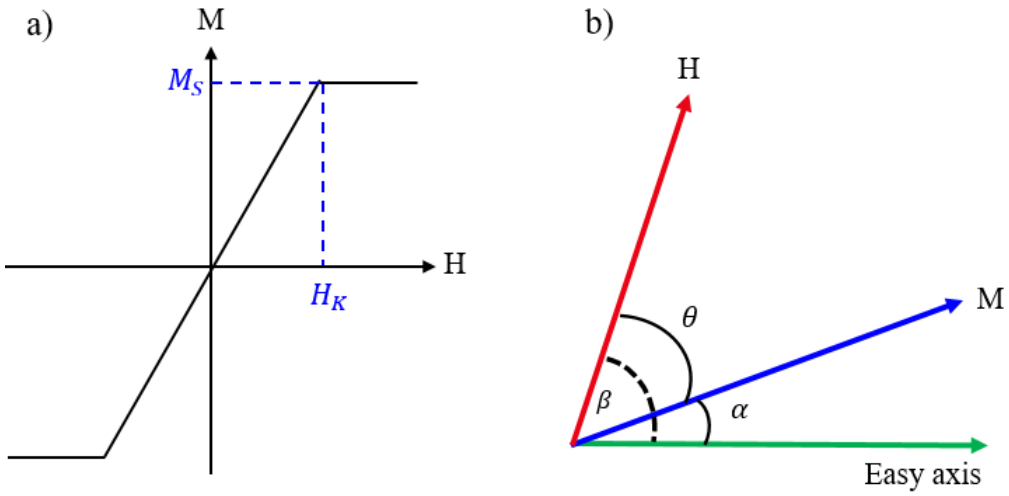

Figure 2.25 a) The relation between the saturation magnetisation, M_S, and anisotropy field, H_K in the Hard axis hysteresis loop. b) Schematic of the magnetisation, the applied field and easy axis for a material.

and the interaction takes a different form in cubic and hexagonal crystals such as cobalt [77, 78, 79].

Figure 2.26(a) shows the lattice structure with hexagonal symmetry of cobalt that possesses easy and hard axes that have been used in the experimental part. The figure shows that the direction of the magnetisation is perpendicular to the basal plane axis, whereas any direction that is parallel to the basal plane is a hard axis as long as the material with hexagonal symmetry only has one easy direction and this direction is called uniaxial. The long dimension of the crystal also produces a lies the easy axis. In individual stripes, the easy axis is along the longest edge, which is 80 nm whereas is the case of the disk the easy axis in the plane along the diameter, which is 80 nm.

Hence for the materials such as Co with easy axes that are perpendicular to the hard axes, the energy associated with the magnetic anisotropy can be written as [78]:

$$E = \sum_{n=1} K_n sin^{2n}\alpha \tag{2.41}$$

where K_n is the anisotropy constant and α is the angle between the magnetisation vector and the easy axis, as shown in Figure 2.26(b). It is sufficient to consider

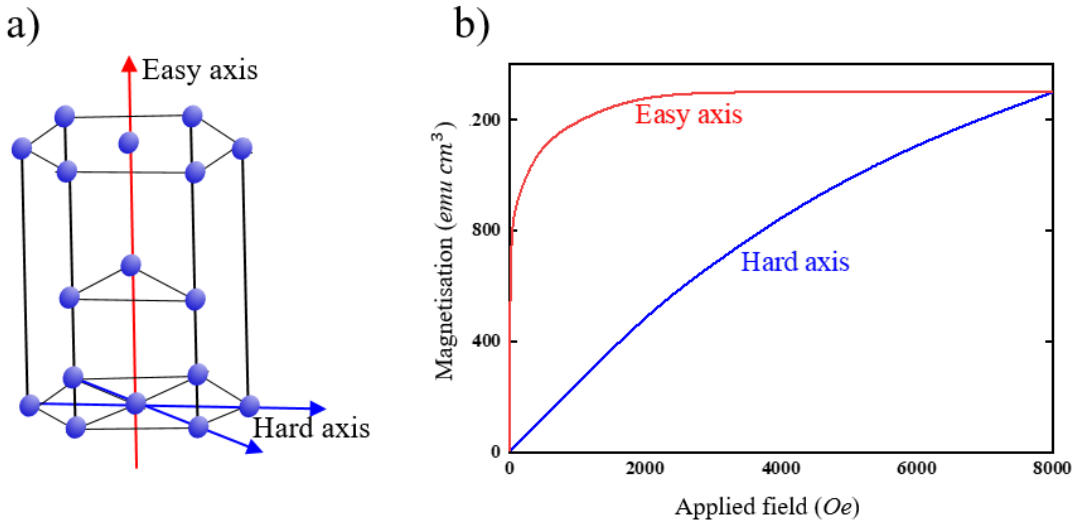

Figure 2.26 a) The cobalt lattice structure, HCP, showing the easy and hard axes in the case of uniaxial anisotropy. b) The magnetisation curves along the easy and hard axes and it can be verified the quick saturation when magnetisation in the easy axis.

only the first two terms. Ignoring the main term because it is isotropic, the energy does not depend on the angle, as follows:

$$E = K_1 sin^2\alpha + K_2 sin^4\alpha \tag{2.42}$$

At resonance, if the magnetic field B_{dc} was applied perpendicular to the easy axis, the magnetisation moves from one direction ($\alpha = 0$) to another direction ($\alpha = 180°$) by the energy barrier to obtain resonance, as shown in Figure 2.27. The energy barrier, $\Delta E = K_u V$, flips the magnetisation, and it is exactly the energy of anisotropy. K_u is the magnetocrystalline energy per volume where $K_u = \mu_0 B_{dc} M$ [80]. This energy barrier leads to the Zeeman energy that is the interaction of magnetic moments with an external magnetic field; thus:

$$E_{Zeeman} = -\mu_0 \int_V M B_{dc} dV \tag{2.43}$$

Consequently, the resonances have shifted in experimental data by the magneto-crystalline anisotropy of Co which added an extra magnetic field. The anisotropy field (coercive field) may be expressed by $H_c = 2K_u/M_s\mu_0$ [81]. K_u is the constant

anisotropy of Co which is 5.5×10^5 J/m^3, at low temperature, which will be used in the calculation in the chapters 4 and 5.

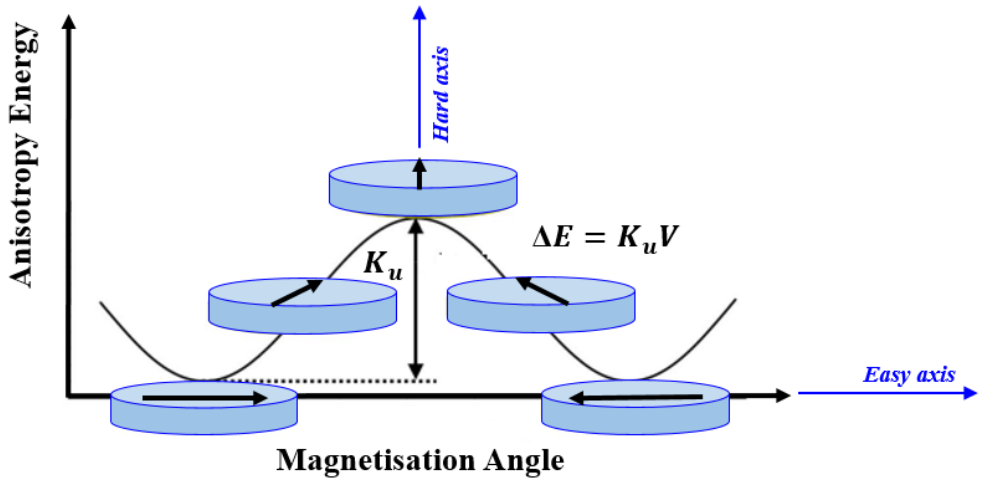

Figure 2.27 At magnetic resonance, the magnetisation will move from one direction ($\alpha = 0$) to another direction ($\alpha = 180°$) by the anisotropy energy, ΔE.

2.9 Two-dimensional Electron Gas System in a Semiconductor Heterojunction

A two-dimensional electron gas (2DEG) is a system of electrons whose motion is free in a two-dimensional plane and confined in the third. The confinement leads to quantized energy levels in the third dimension. This can be achieved in the 2DEGs that formed at the junction when two different materials which have different band gaps and Fermi levels come into contact. Because of the mismatch between conduction band offsets, the quantum potential well traps the 2DEG. It is ordinarily observed in semiconductor heterostructures such as $GaAs/AlGaAs$, graphene and the metal oxide semiconductor field effect transistors (MOSFETs), where we will focus on the $GaAs/AlGaAs$ heterojunction in this study. [82, 83, 84].

Figure 2.28 shows that the band structure of a semiconductor heterostructure consists of several layers grown on GaAs substrate. There is also a conduction band E_c, a valence band E_v and the Fermi level E_F, which determine the electron

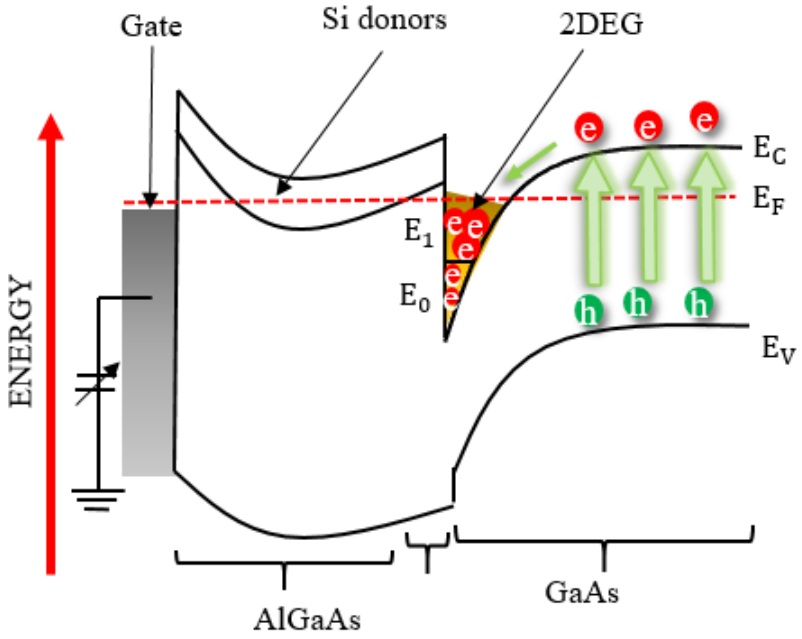

Figure 2.28 The conduction band structure of a $GaAs/AlGaAs$ heterojunction.

density in the 2DEG. The band gap of $AlGaAs$ is approximately 2.0 eV which is bigger than the band gap of $GaAs$, which is about 1.52 eV; a part of the barrier of the $AlGaAs$ is undoped near the interface and is called 'the spacer', the spacer increases the electron mobility by setting the impurity scattering potential away from the interface. The $AlGaAs$ barrier is Si-doped 10 nm from the interface to generate the free carriers of the electron gas. The Si has one extra electron per atom as substitutional impurities for Ga. These electrons will be jumping from the barrier down the potential triangular well.

Experimentally, the mobility of the electron gas increases with the thickness of the spacer while there is an inverse relationship between the 2DEG density and the thickness of the spacer [85]. Because the electrons are very far from the band impurities, that leads to the high mobility of this system. The most significant advantage of this technique is the high sensitivity that arises from the low electron density that can be described as the measure of the probability of an electron being present at a specific location and high charge carrier mobility of 2DEGs relative to metals in the order of $n_s = 1.6 \times 10^{11} cm^{-2}$ and $\mu = 1.5 \times 10^6 cm^2.V^{-1}.s^{-1}$, respectively [1, 3]. The mobility of the 2DEG is very high comparing with the mobility of 2-D Graphene which is between 3000 and 27000 $cm^2.V^{-1}.s^{-1}$. [86].

By applying the electric field, E, in the plane of the 2DEG, the electrons will move with drift velocity, v_d, which is given by this equation:

$$v_d = \frac{eE\Delta t}{m^*} \tag{2.44}$$

Herein, m^* is the carrier effective electron mass in $GaAs$ which is approximately $0.067\ m_e$, and Δt is the average time between collisions. The average of Δt is the scattering time τ and the average drift velocity can be displayed by this equation:

$$v_d = -\mu_e E \tag{2.45}$$

Here, μ_e is the electron mobility, which is $\mu_e = e\tau/m$. The minus sign points to that, the drift velocity has an opposite direction to the electric field vector direction. There is also a drift current, which is thus given as:

$$J_d = -en_s v_d \tag{2.46}$$

Equation 2.46 can be rewritten according to Ohm's law, where n_s is the electron density:

$$J_d = \sigma E \tag{2.47}$$

The conductivity could be derived as $\sigma = n_s e \mu_e$, where the energy of the conduction electrons in a sub-band of a 2DEG can be written as a function of momentum, $\hbar^2 k^2$, as:

$$E(k) = \frac{\hbar^2 k^2}{2m^*} \tag{2.48}$$

Now, calculating the density of states which is the derivative of the number of electronic states $n(E)$ with energy [87]:

$$\rho(E) = \frac{dn(E)}{dE} \tag{2.49}$$

where the number of states is given by:

$$n(E) = \frac{g_s g_v A}{(2\pi)^2} \tag{2.50}$$

Therefore, A is the area of the Fermi surface, which is circle in the k-space, it could be expressed as $A = \pi k_F^2$ with a radius equal to the Fermi wavevector (k_F). From Equation 2.48, $k^2 = 2m^*E/\hbar^2$. Thus, $A = 2\pi m^*E/\hbar^2$. There is also a number of states given by:

$$n(E) = \frac{g_s g_v m^* E}{2\pi\hbar^2} \tag{2.51}$$

Here, g_s and g_v are the spin (g_s) and valley (g_v) degeneracies, respectively. So, the final equation describes the density of states corresponding to a single sub-band in a 2DEG:

$$\rho(E) = \frac{g_s g_v m^*}{2\pi\hbar^2} \tag{2.52}$$

It is constant inside each sub-band for any energy value. Moreover, n_s is dependent on the following factors: the number of states, $n(E)$, and the Fermi–Dirac occupation function which is related to the temperature. The Fermi wavevector k_F is therefore $k_F = \sqrt{2\pi n_s}$.

Figure 2.29(a) illustrates the density of states $\rho(E)$ as a function of energy in 2DEG. The sequence of sub-bands is related to the discrete levels in the potential well, which is confines the 2DEG to the interface. So, when the temperature is low enough, that means the electron density and the Fermi level will be low as well. The reason for that, at the constant density of state, n_s have a linear relationship with E_F as a function of Equation $n(E) = g_s g_v m^* E_F/2\pi\hbar^2$.

When the magnetic field is applied perpendicular to the 2DEG, it will introduce the Landau quantization of the energy levels, which characterises the quantum Hall regime [88]. The action of the Lorentz force will force the electrons into circular cyclotron orbits and the energy spectrum becomes discrete. Consequently, the radius of the cyclotron will be quantized because it is proportional to the square root of the energy. The energy level which is from the quantization of the circular cyclotron motion can be written as [89]:

$$E_n = \hbar\omega_c(n + \frac{1}{2}) \tag{2.53}$$

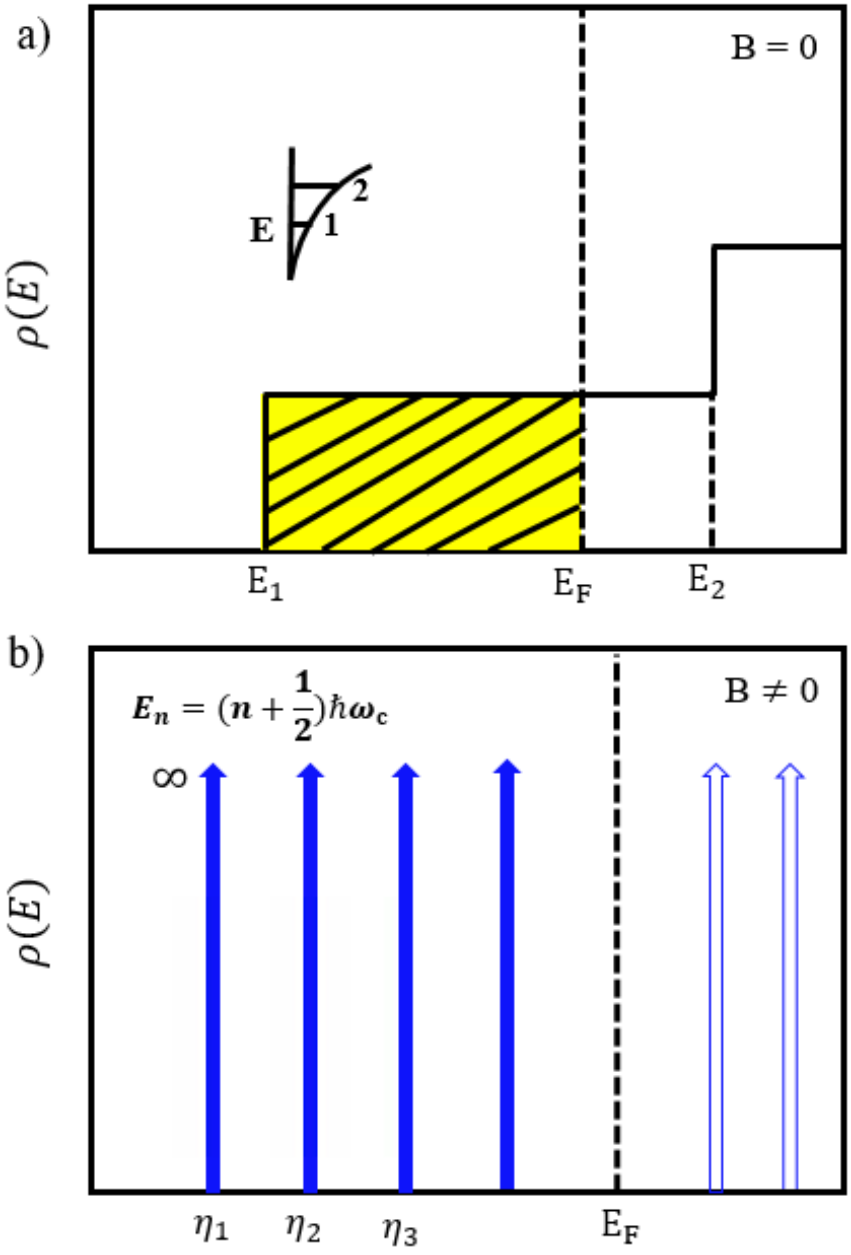

Figure 2.29 a) The density of states $\rho(E)$ as a function of energy in 2DEG. Inset: confinement potential well perpendicular to the plane of the 2DEG. The discrete energy levels (E_1 and E_2) are corresponding to the bottoms of the first and second 2D sub-bands. b) The density of states for a 2DEG in a perpendicular magnetic field as a function of energy. The landau levels are shown in blue below Fermi level.

Herein, $\omega_c = eB/m^*$ is the cyclotron frequency and $n = 1, 2, 3, ...$ is the quantum number associated with the Landau levels. Figure 2.29(b) shows the density of states in a perpendicular magnetic field, where E_1 and E_2 are the energy values of the first two Landau levels. By Equation 2.53, there is a linear proportionality between the magnetic field that is applied and the spacing between the Landau levels.

Chapter 3

Experimental and Simulation Methods

The first aim of this chapter is to describe how the hybrid ferromagnetic-semiconductor device was fabricated [90]. Ferromagnetic nanomagnets (Cobalt) were fabricated on top of $GaAs/AlGaAs$ structures using electron beam lithography. The second aim is to describe the experimental setup, including fabricating the sample, a microstrip antenna and a microwave bench, which were built in the laboratory. The microwave bench was controlled by LabVIEW software, which was developed to automate the experiment. A range of microstrip antenna was designed each of which was centred on a different frequency in the 3 GHz - 30 GHz range of ferromagnetic resonance, which generated an ultra-high frequency spectrum and was utilised to transmit electromagnetic waves to the sample. The third aim is to focus on the micromagnetic simulation by OOMMF and compare the results with experimental measurements.

3.1 Experimental Setup

3.1.1 Samples Fabrication

The first step to creating a semiconductor device is to grow the Wafer. The Wafers used to fabricate the samples were grown at the University of Cambridge (Cavendish Laboratory) on the silicon substrate. However, $GaAs$ is commonly used to manufacture semiconductor devices, which typically consist of two layers, $GaAs$ and $Al_{0.33}Ga_{0.67}As$. These layers have a similar lattice constant, so there is a smooth boundary between them. 2DEG could also be formed at the interface due to differences in the two layers' conduction band energy. The $GaAs/Al_{0.33}Ga_{0.67}As$ heterojunction hosting the 2DEG was 30 nm beneath the surface. Such shallow 2DEG allowed minimizing the decay of the magnetic field from the nanomagnets [91].

However, when the wafer arrived in the shape of a thin disc (3 in diameter), the substrate was then sliced to a suitable size for processing, ordinarily, $1cm^2$. Through a series of lithographic steps: First, resist was spun on the wafer at a speed of 4000 rpm giving a thickness of resist of nearly 1.4μm [21, 22, 92]. Next, the resist was baked in the oven at $95C^0$ for 30 minutes, followed by exposing and developing the sample to transfer the pattern to the resist. The exposed area was more soluble in the developer and was removed. One of the most important steps is employing the etching technique; to remove the exposed GaAs, which is not protected by photoresist and insulate 2DEG.

The Hall bar system was etched in a $SiCl_4 : SiF_4$ plasma for nearly nine seconds; the remaining resist is then stripped by washing in acetone. Because it was impossible to attach wires to the semiconductor, it was necessary to fabricate a metal contact between the surface and the 2DEG utilising an evaporation technique. It was performed in a vacuum, typically $\approx 10^{-6}$ mbar, to avoid impurities in the deposited film. Once again, for the contact to the 2DEG, four metal layers were evaporated: 60 nm of Ge and 90 nm of Au, followed by 33 nm of Ni and a further 200 nm of Au. Finally, to diffuse the ohmic contact through the GaAs surface and create a metal connection with the 2DEG, the wafer was placed into a rapid thermal annealer and heated to $400C^0$ for 15s.

Since the size of the semiconductor device is remarkably small, it is exceedingly difficult to wire it to precise measurements. Sample mounting and bonding are crucial to afford the device to a $1cm^2$ 'chip carrier'. The chip carrier is the ceramic tile with a series of metallic contact pads around the edge where wires can be soldered to. Nevertheless, it will be glued to the chip carrier by GE varnish to retain the adhesive characteristics of the material in the low-temperature experiment. Consequently, the wire must be connected to the metallic pads on the chip carrier using an ultrasonic bonding machine. A coated, 25 μm copper/gold alloy wire must be used in the connection, and it is attached using a Wedge bonder. To perform an experiment, the chip carrier is secured to a metal insert that can be placed inside the experimental apparatus. This insert carrier is the connection between the chip carrier and the measurement equipment.

Figure 3.1(a) shows the sample and chip carrier assembly, which consists of a Hall bar system with a rectangular shape that has a series of voltage probe terminals on either side. The active region of Hall bar is 8 μm wide and 32 μm long. The side arms are voltage probes, and both ends of the Hall bar act as current probes. As shown in Figure 3.1(b), the voltage probes were separated by 2-16 μm gaps. The localised spin-wave modes were distinguished by measuring the photovoltage between two probes in the longitudinal and transverse directions across the ferromagnetic element.

The photovoltage was indicated by irradiating the microwaves at the frequency within a microstrip antenna and will be described later in this chapter. A microwave synthesiser is used to excite an antenna with a GHz signal at different power -10 dBm, -20 dBm, and -30 dBm. Figure 3.2(a) indicates a high-resolution SEM image of a Hall bar device used for photovoltage spectroscopy measurements, the black hollow square indicates the location of the Co. Figure 3.2(b) shows a high-resolution SEM micrograph of a Co stripe that is 80 nm wide and 30 nm thick in the active region of a Hall bar while Figure 3.2(c) illustrates a high-resolution SEM micrograph of a single dot that had an 80 nm diameter, 40 nm thickness, and was magnetised parallel to the 2DEG by B_{dc}.

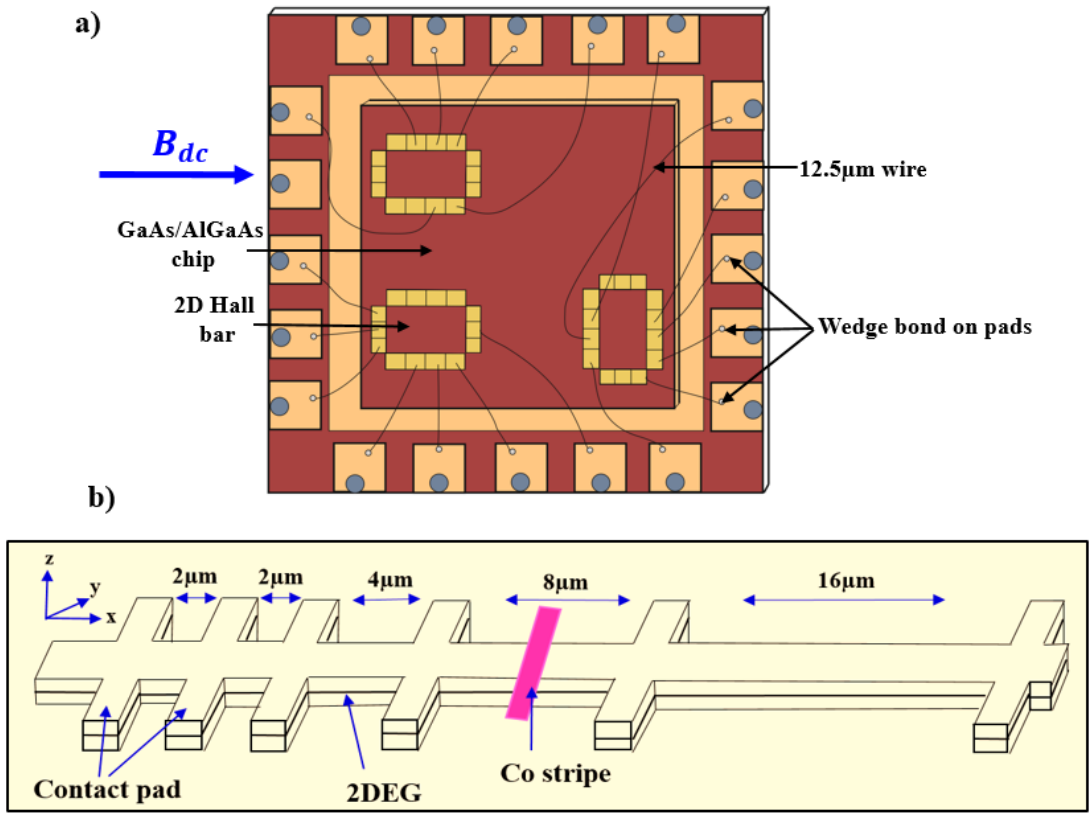

Figure 3.1 a) The schematics of a hybrid semeconductor-ferromagnetic device, showing the micro-magnetised in the plane of the 2DEG by the static magnetic field, B_{dc}. b) A diagram of a Hall bar made from a $GaAs/Al_{0.33}Ga_{0.67}As$ heterojunction that contains a 2DEG. The photovoltage was measured across $8\mu m$ probes.

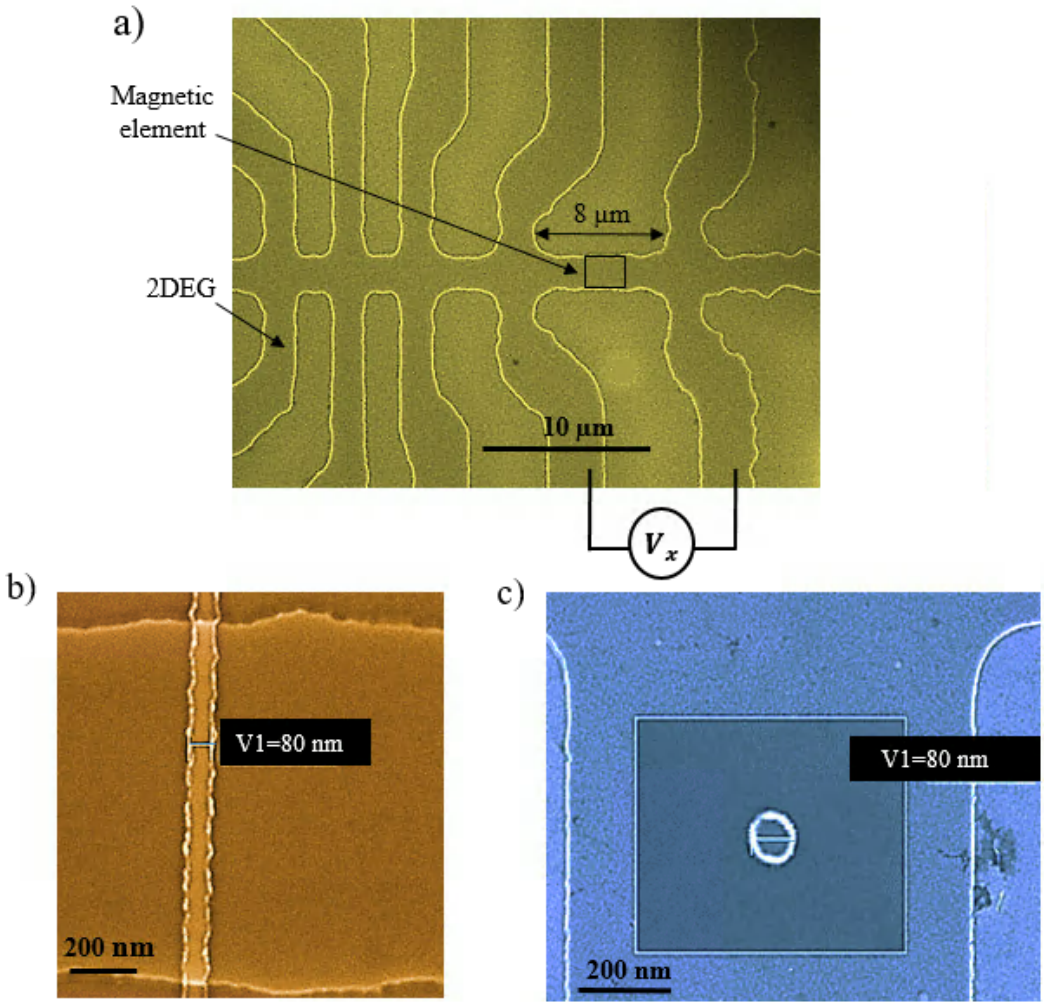

Figure 3.2 a) A SEM image of the sample of a Hall bar system, focusing on the gap across the 8 μm probes, the black hollow square indicates the location of the Co. b) A higher-resolution SEM image of a Co stripe with 80 nm wide and 30 nm thick. c) A SEM image of a cobalt dot that had an 80 nm diameter, 40 nm thickness.

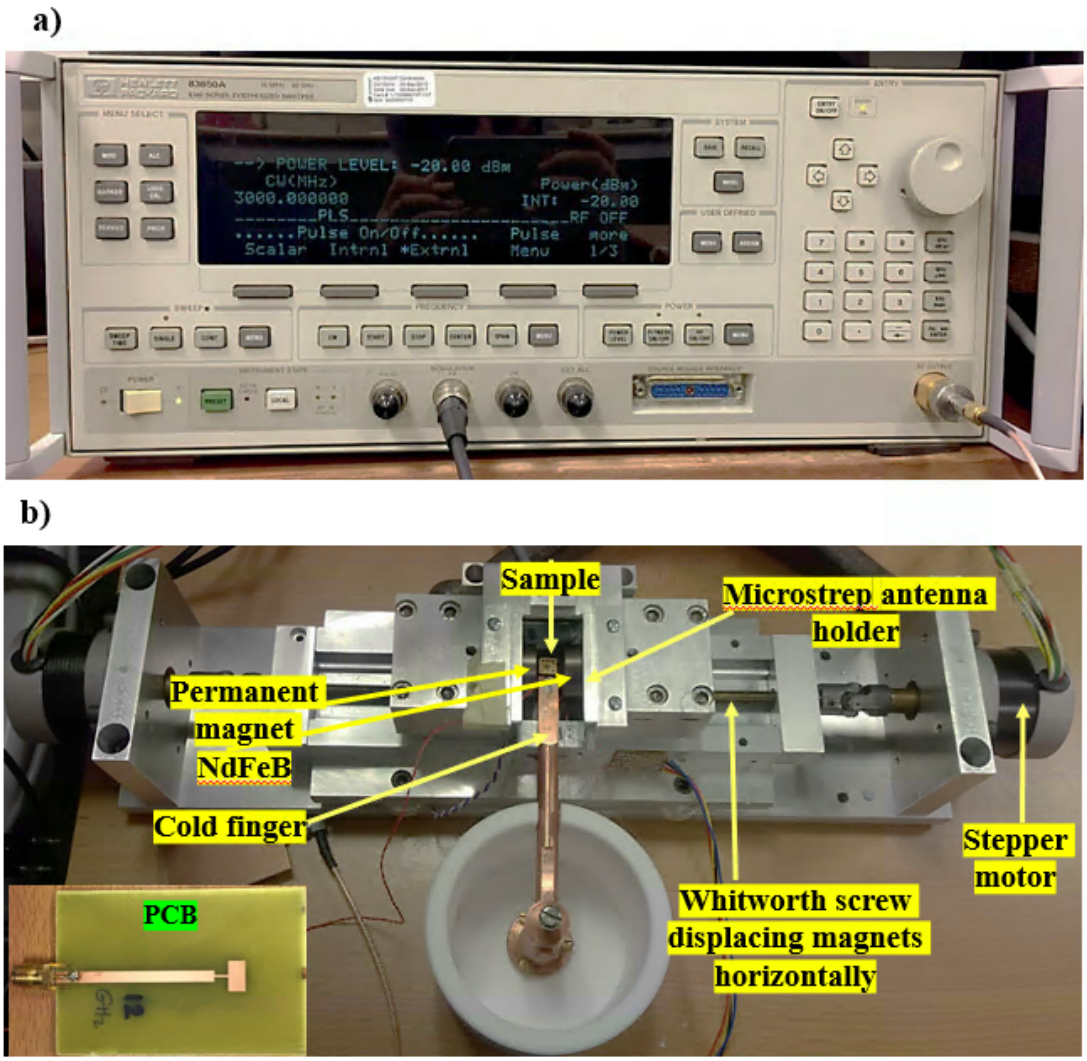

Figure 3.3 a) The microwave source 0 – 25 GHz and b) The setup of the microwave bench, consisting of a sample at the centre between two neodymium–iron–boron magnets housed on a Whitworth screw. The screw is controlled by a stepper motor and a temperature sensor on the cold finger.

3.1.2 The Microwave Bench

During this stage, we built a microwave bench to measure the photovoltage spectra by varying the B_{dc} field at constant microwave frequency, and the sample was located in the middle of the bench between two Neodymium Iron Boron, NdFeB, permanent magnets which are the strongest magnets, and it is available with steel weight of up to 7.3 kg. These magnets were housed on a Whitworth screw attached

to a stepper motor. There are two stepper motors with voltage rating 12 V_{dc}, current rating 0.16 A and six wires. The screw provides a calibrated translational distance per number of steps of the stepper motors, and the distance corresponds to a 0.0125 mm translation for each magnet. The motors move the magnets, which produces an external magnetic field B_{dc} through the sample by sliding the magnets symmetrically away from and towards the sample site. The distance varied from 11 to 50 mm, and this distance gives to the magnetic field's strength, which was modified from 0.083 to 0.606 T (Figure 3.3). The two parallel openings between the magnets are for inserting the PCB antenna, which will be presented in more detail in the next section. The sample, which works as a receiver, was irradiated by shining different microwave frequencies using the microstrip antenna, which was placed directly over the sample. The microwave bench was controlled by LabVIEW software to vary the distance between the two permanent magnets so photovoltage could be measured as the Larmor magnetic field was varied.

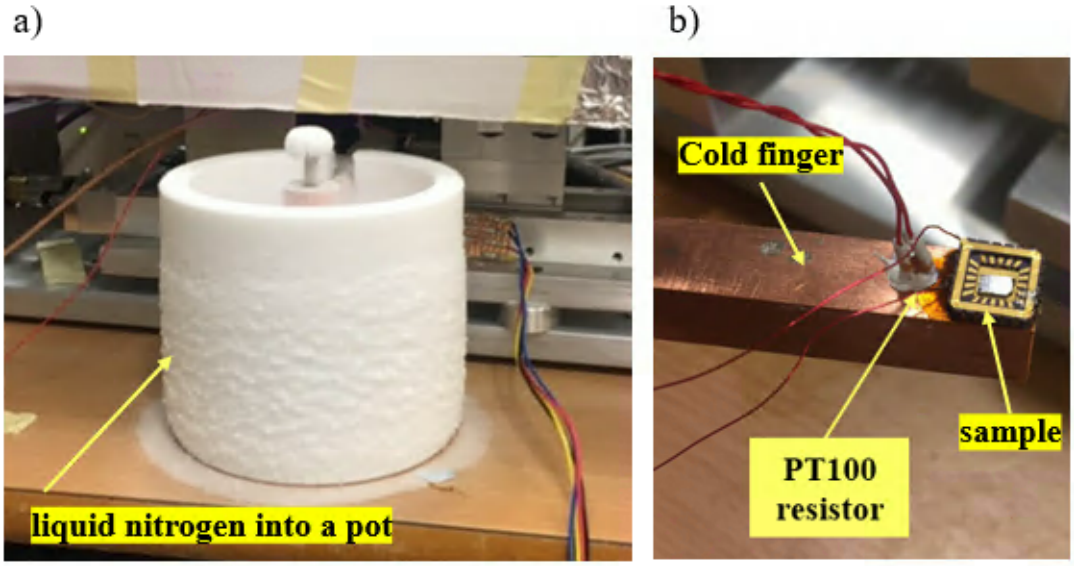

Figure 3.4 At low-temperature measurements, a) The liquid nitrogen into a pot to cooling the sample. b) A small hole in the cold finger near the sample and the PT100 resistor.

The low-temperature measurements were performed by cooling the sample using a cold finger polytetrafluoroethylene pot with a copper base. A copper finger was fastened to the copper base, and the sample remained at the end of the finger, away from the pot. Liquid nitrogen cooled the copper equipment and, consequently,

the sample to 77 K, Figure 3.4(a). Since the sample is located at the end of the finger and in contact with the environment, it is at the warmest part of the finger. Thus, a temperature gradient exists between the reservoir and the sample. Due to the gradient the sample will not be at liquid nitrogen boiling point but somewhere higher than that. A platinum resistor (PT100 resistor) is using to measure the temperature of the cold finger near the sample [93]. The PT100 resistor has a nominal resistance of 100 Ω at 0 °C and a temperature coefficient of 3850 ppm/K. This particular resistor is Class Y so its tolerance is 0.10 + 0.0017×|T| valid from -50 °C to 150 °C where |T| is the numerical value of the temperature in °C without taking leading signs into account. For a PT100 element, the relationship between the resistance and temperature for the temperature range between -200 °C $\leq T \leq$ 0°C can be described as the following equation [94]:

$$R(T) = R_0(1 + A \times T + B \times T^2 + C \times [T - 100] \times T^3) \tag{3.1}$$

where R(T) is the resistance at temperature T. A, B and C are material-dependent coefficients and $R_0 = 100\ \Omega$ is the nominal resistance at 0°C. For the platinum resistor with the temperature coefficient 3850 ppm/K the coefficients are $A = 3.9083 \times 10^{-3\circ}\mathrm{C}^{-1}; B = -5.775 \times 10^{-7\circ}\mathrm{C}^{-2}; C = -4.183 \times 10^{-12\circ}\mathrm{C}^{-4}$.

Besides, a small hole was created in the cold finger near the sample and the resistor is embedded in this hole with the assistance of heat-conductive paste, Figure 3.4(b). A multimeter was used to measure the resistance of the resistor. Low noise measurements were obtained using a model 5210 lock-in amplifier. Lock-ins are helpful in reducing noise and obtaining an accurate reading of a homogenous sample. A lock-in consists of several parts, including two input connectors used to determine the sensitivity of the voltage. The display was, therefore, used to set the voltage in the Hall probe. The reference was also connected with the waveform generator's output, which was required to communicate with the multimeter and obtain the analogue voltage.

Figure 3.5 illustrates the experimental setup, consisting of a microwave bench holding a sample, which was irradiated with microwaves emitted by a microstrip antenna (yellow). Two motorised magnets (green) were also used, as well as a microwave generator and its custom-made antenna, a lock-in amplifier, multimeter,

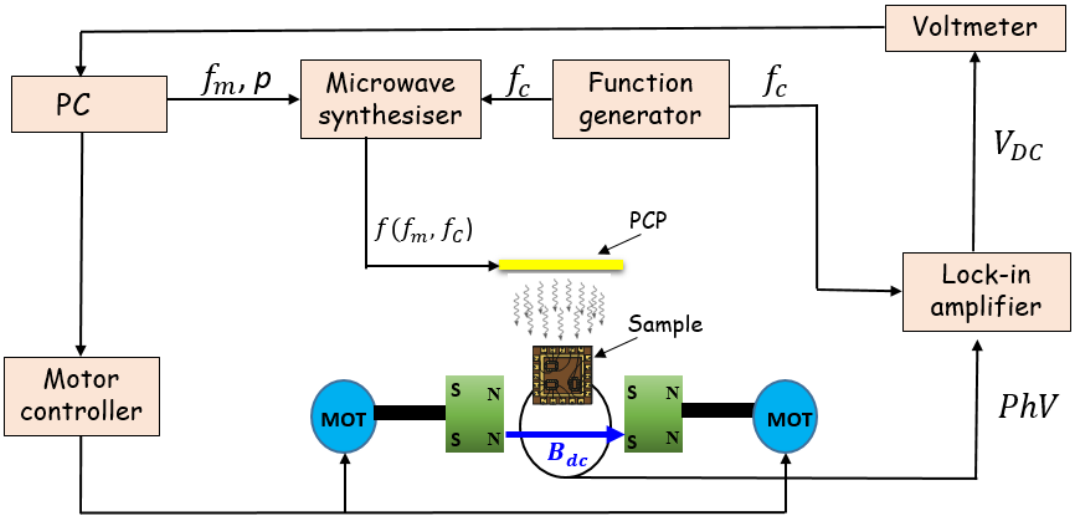

Figure 3.5 A schematic of the photovoltage spectroscopy experimental setup consists of a rig holding a sample with two motorised magnets; a microwave generator and its custom-made antenna; a lock-in amplifier; multimeter, a LabVIEW program in the computer to control the experiment, and the function generator.

a function generator, and a computer with LabVIEW software installed. The microstrip antenna was excited using a microwave synthesiser with a GHz signal $f_m = 3$ GHz modulated with a kHz signal f_C from a function generator where f_m was set by the LabVIEW software. A lock-in amplifier, which demodulated the resulting oscillating photovoltage across the sample with a reference signal f_C from the function generator, was also used. A voltmeter measured the voltage from the output of the lock-in amplifier, which is proportional to the magnitude of the oscillating photovoltage. In addition, this system allows for the following five variables: the photovoltage and photoresistance; microwave frequency; applied magnetic field; temperature, and microwave power.

3.1.3 Microstrip Antenna

The microstrip antenna is a critical part of the experimental setup; this antenna has the ability to direct radiation to the sample at a peak frequency defined by the geometry of the stripe. It has many advantages: it is lightweight, suitable for use in small devices (e.g., cellular phones), and, most significantly, easy to manufacture in the laboratory.

f (GHz)	λ_0 (mm)	W (mm)	ε_{eff}	λ_{sub}	ΔL (mm)	L_{eff}	L	Zin	Zo	ε_r	A	W/d (Z_0)	W (Z_0)	Z t	A	W /d (Z_T)	W (Z_T)
3	100	30	4.291	48.3	0.75304	24.1	0	202	50	4.7	1.57	1.82	2.91	100	3	0.403	0.64
6	50	15	4.071	24.8	0.76	12.4	10.9	202	50	4.7	1.57	1.82	2.91	100	3	0.403	0.64
9	33	9.9	3.928	16.8	0.7649	8.41	6.88	202	50	4.7	1.57	1.82	2.91	100	3	0.403	0.64
12	25	7.4	3.826	12.8	0.76854	6.39	4.85	202	50	4.7	1.57	1.82	2.91	100	3	0.40	0.64
15	20	5.9	3.748	10.3	0.77135	5.17	3.62	202	50	4.7	1.57	1.82	2.91	100	3	0.403	0.64
18	17	4.9	3.687	8.68	0.77357	4.34	2.79	202	50	4.7	1.57	1.82	2.91	100	3	0.403	0.64
21	14	4.2	3.636	7.49	0.77533	3.75	2.2	202	50	4.7	1.57	1.82	2.91	100	3	0.403	0.64
24	13	3.7	3.594	6.59	0.77675	3.3	1.74	202	50	4.7	1.57	1.82	2.91	100	3	0.403	0.64

Table 3.1 The calculations of the dimension of the microstrip antenna including the length, L, width, W, of the patch antenna at different frequencies at the range of 3 GHz to 24 GHz; the dimension of the termination impedance, Z_0, the Z_{IN}, and the dimension of the quarter-wave transformer Z_T. All those dimensions were used to design and fabricate the microstrip antenna in the laboratory.

Various steps must, therefore, be taken to fabricate the microstrip antenna. The waveguide was designed using computer aided design (CAD) and the desired dimensions and then transferred to vellum paper, which was transferred to the printed circuit board (PCB) (Table 3.1). Then, the double-sided photoresist board was printed on A4 vellum paper. Afterwards, the waveguide pattern was transferred from the paper to one side of the PCB using UV lithography for about 3 minutes and 30 seconds. The PCB was developed and etched using a copper etch solution at 40°C and then cleaned in water. During the developing stage, a mixture of 25 ml of sodium hydroxide (NaOH) and 75 ml of 25°C water, for approximately 2 minutes. Then, the PCB was rinsed in water and blown dry, followed by etching in the copper etch bath for approximately 5 minutes. Ultimately, the cells holding waveguides were each cut into 16 pieces to prepare them for soldering to the n-type connectors.

The rectangular microstrip antenna has a patch line supplied by a transmission line made from copper, which has high conductivity; L and W indicate the patch length and width, respectively. The transmission line model depicts the width and height of the patch antenna as two radiation slots separated by a transmission line of length L, as shown in Figure 3.6. Table 3.1 shows the calculations of the dimension of the microstrip antenna. It can be started by calculating the L from

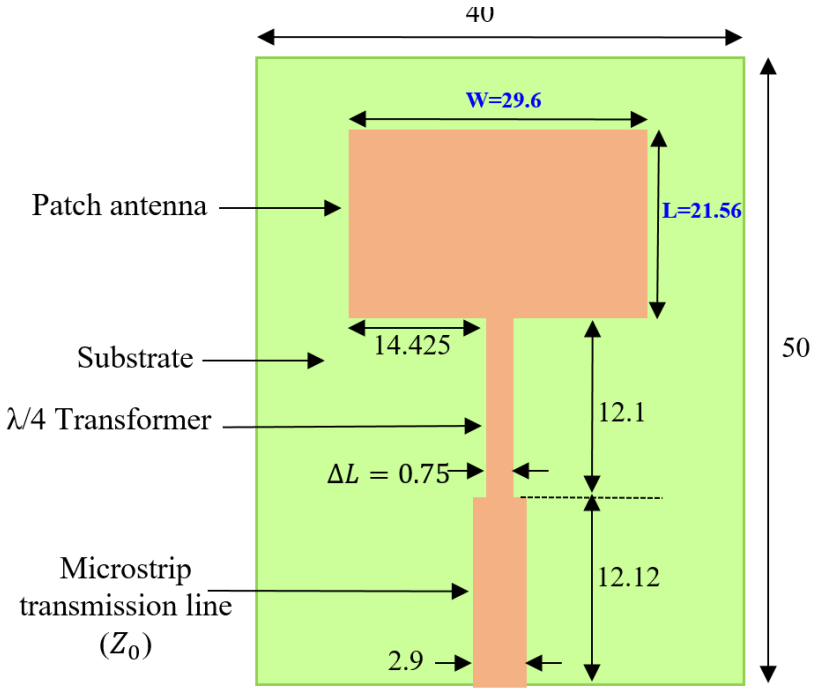

Figure 3.6 Configuration and dimensions of 3 GHz microstrip antenna, consisting of the transmission line, quarter wave transformer, and patch antenna. All the dimensions are in mm.

this expression:

$$L = \frac{\lambda_{sub}}{2} = \frac{3}{2} = 1.5 \tag{3.2}$$

Here, $\lambda_{sub} = \lambda_0 \sqrt{\varepsilon_{eff}}$, and $\lambda_0 = c/f$. For an efficient emitter with a given dielectric of thickness $h = 1.6$ mm and operating frequency f_0, a practical width is calculated using the following equation [95, 96]:

$$W = \frac{c}{2f_0\sqrt{(\varepsilon_r + 1)/2}} \tag{3.3}$$

If the width is larger, the radiation will be more efficient, but it may produce higher-order modes. The influence of a fringing field along the radiating slot's width could be modelled in the expression of a line extension, ΔL. Once W is fixed, ε_{eff} may be calculated as follows:

$$\varepsilon_{eff} = \frac{\varepsilon_r + 1}{2} + \frac{\varepsilon_r - 1}{2} \cdot \frac{1}{\sqrt{1 + \frac{12h}{W}}} \tag{3.4}$$

where ε_{eff} is the effective dielectric constant, ε_r is the relative permittivity of the dielectric substrate = 4.7, and h is the thickness = 1.6 mm. Thus, ΔL is given by the following equation:

$$\Delta L = 0.412h\frac{(\varepsilon_{eff} + 0.3)(W/h + 0.264)}{(\varepsilon_{eff} - 0.258)(W/h + 0.8)} \tag{3.5}$$

The antenna's length can be determined using the following equation:

$$L = L_{eff} - 2\Delta L \tag{3.6}$$

where,

$$L_{eff} = \frac{c}{2f_0\sqrt{\varepsilon_{eff}}} \tag{3.7}$$

Figure 3.6 shows the termination impedance Z_0= 50 Ω that matches to the cable and connector (all 50 Ω), and the input impedance Z_{IN} is very low because the patch is wider than the section of Z_0. Consequently, when connecting Z_0 directly to the patch without the quarter wave transformer, it will be seen some reflection of power. Thus, the purpose of adding a quarter-wave transformer is to match the input impedance Z_{IN} of the antenna with the termination impedance Z_0 and to reduce the reflection. Now, assuming $W \ll \lambda_0$, the input impedance is given by the following equation [97]:

$$Z_{IN} = \frac{1}{2G_1} \tag{3.8}$$

where G_1 is the conductance of the metal strip, and is given by [98]:

$$G_1 = \frac{1}{90}(\frac{W}{\lambda_o})^2 \tag{3.9}$$

However, the quarter-wave transformer must have a correct impedance, which is the transformer impedance Z_T, to correctly match the 50 Ω and Z_{IN}. This impedance could be calculated using the following equation:

$$Z_T = \sqrt{Z_0 * Z_{IN}} \tag{3.10}$$

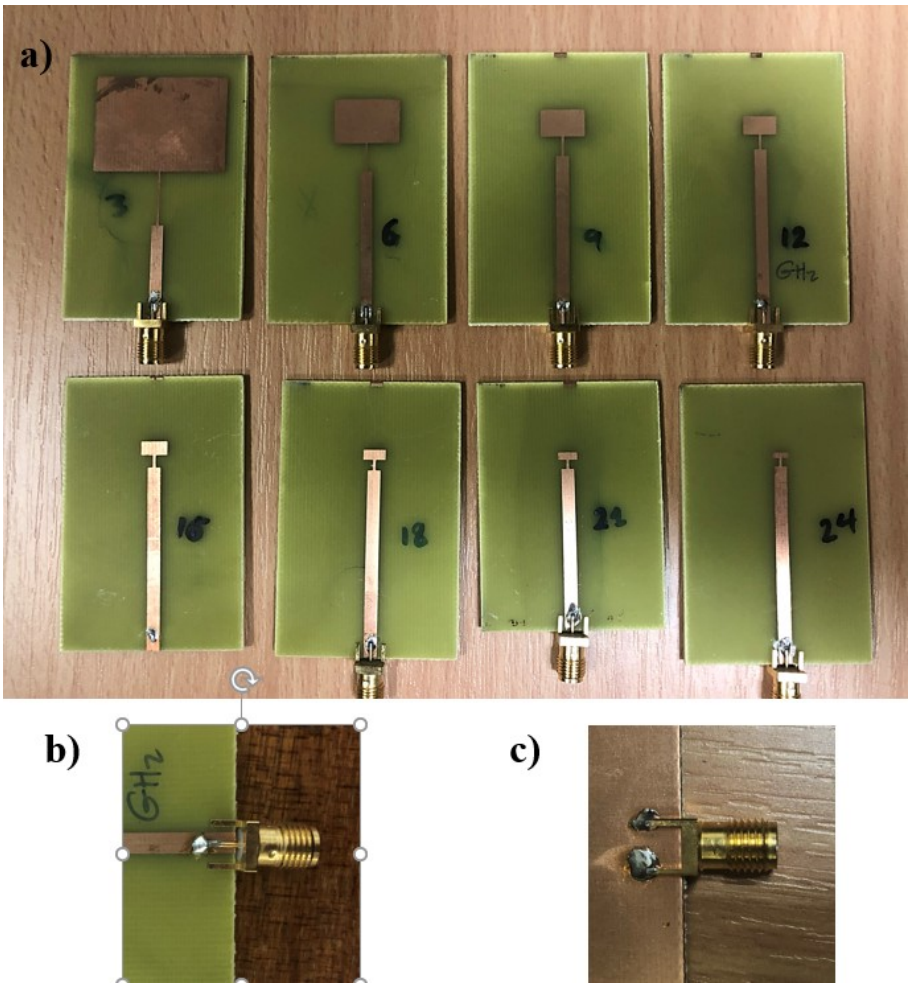

Figure 3.7 a) Top view of the microstrip antennas engineered to emit at a range of different frequencies: 3, 6, 9, 12, 15, 18, 21, and 24 GHz. b) Top view. c) Bottom view of the BNC connector to the waveguide.

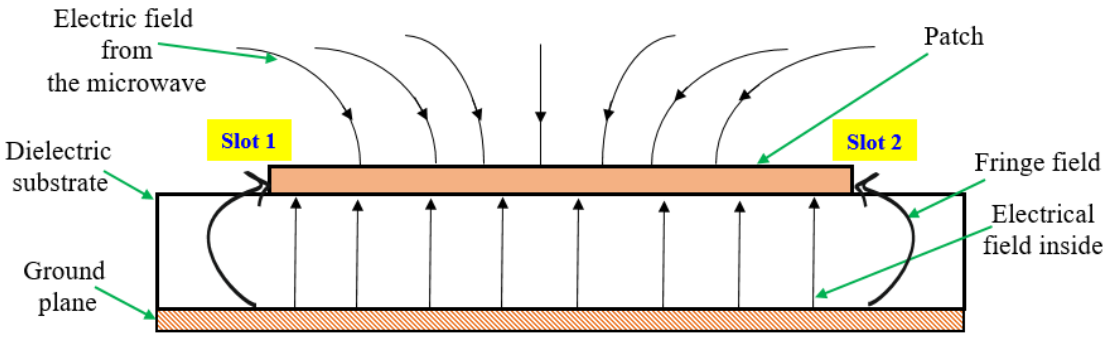

Figure 3.8 The transmission line design for rectangular patch antenna as radiating slot, and showing the electric field distribution.

Furthermore, the microstrip antenna was built using a thin copper strip located on the small portion of the wavelength above a ground plane in a dielectric substrate (Figure 3.7). Figure 3.8 demonstrates that the patch antenna consists of a ground plane, dielectric substrate and radiating patch , and parallel-plate transmission line connected with two radiating slots. Electromagnetic waves fringe between the top parts and the substrate. The frequency spectrum of the stripe antenna is between 300 MHz and 3000 MHz. It is designed to transmit or receive electromagnetic waves [97]. In addition, it was be printed directly onto a circuit board with the dimensions of 16 cm $\times$ 20 cm. The microstrip antenna developed in this thesis has a rectangular shape and was manufactured in the laboratory for different frequency bands (i.e., 3 GHz, 6 GHz, and so on, up to 24 GHz).

To probe the emission spectrum of each patch antenna against prediction and compare it, we measured as follows. Figure 3.9 shows the experimental measurements were performed by exposing the sample to microwave and varying the power frequency at fixed values of power (-10 dBm, -20 dBm, and -30 dBm), as explained in Section 3.1.2. The spectrum analyser was utilized to measure each value of input microwave power automatically by LabVIEW, as detailed below.

Figure 3.9 also shows that, the amplitude of the peak increases with increasing power frequency, experimentally. In theory, the amplitude of the peak must increase proportionally to the square root of the power, $\sqrt{P}$, which is proportional to the ac magnetic field according to the following equation:

$$A \propto \sqrt{P} \propto B_{ac} \tag{3.11}$$

Figure 3.10 interprets the amplitude of the peak for each value of power calculated using the attenuation which is expressed in decibels (dBm):

$$P_{dBm} = 20log_{10}\frac{P}{P_0} \tag{3.12}$$

where P_0 is 100 mWatt, and P is the source signal. In addition, the amplitude can be calculated using the formula for the electromagnetic power:

$$A = B_{ac} = \sqrt{2\mu_0 P} \tag{3.13}$$

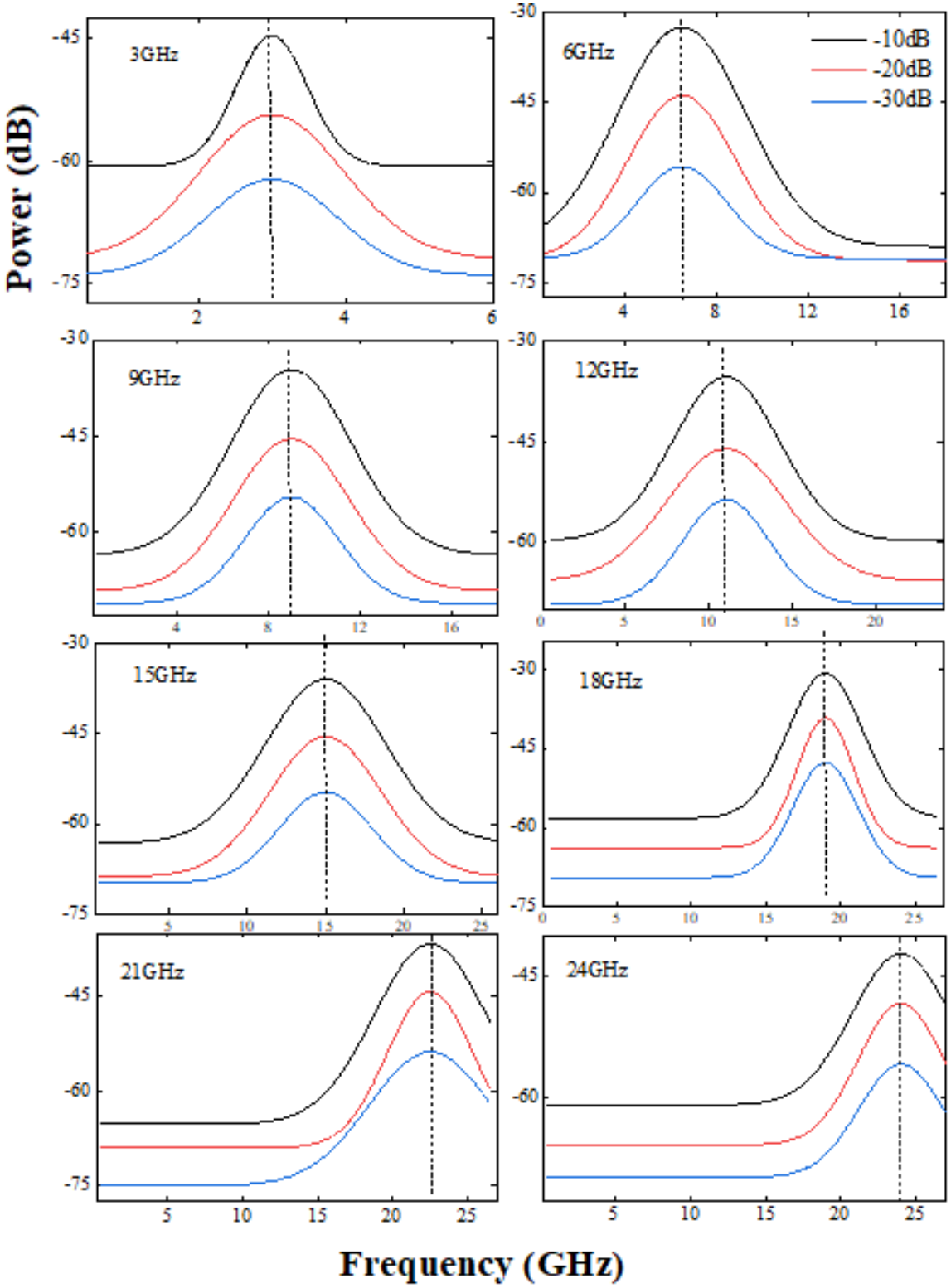

Figure 3.9 Plot of the power spectrum versus frequency with different power (-10 dBm,-20 dBm,-30 dBm) at 3 GHz, 6 GHz, 9 GHz, 12 GHz, 15 GHz, 18 GHz, 21 GHz and 24 GHz.

The above equation is possible because the electric and magnetic fields are interchangeable for an electromagnetic wave; $E = cB$. Thus, when the square root of the power is 0.3, the amplitude is 500 μWatt while when the square root of the power is 10, the amplitude is 15849 μWatt. This indicates theat the examination of the power frequency with the microstrip antenna was successful and allows measurements at low temperature as we show in the next chapter.

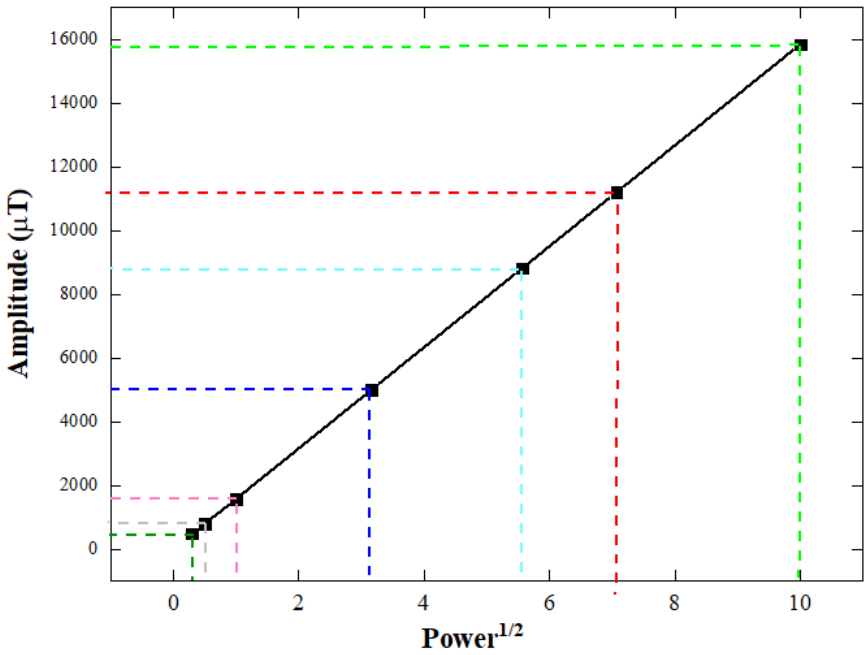

Figure 3.10 Plot of the amplitude of the peak versus the square root of the attenuation of the power.

3.2 Measurement Process

Spin-waves in the ferromagnetic samples varied the electrical properties of the 2DEG while stray magnetic fields threaded the 2DEG and induced eddy currents. Resistance was measured using 4-terminal measurements. The voltage measurements were taken between two channels in the Hall bar system while current is passed through it as shown in Figure 3.11. One of the advantages of this method is that it allows measurements of resistance of the 2DEG when the modulated current is supplied. A current source, I_{ac}, can be formed from the lock-in amplifier with an oscillator voltage oscillator V_{ac} (13 Hz) in series with a resistor, r (1

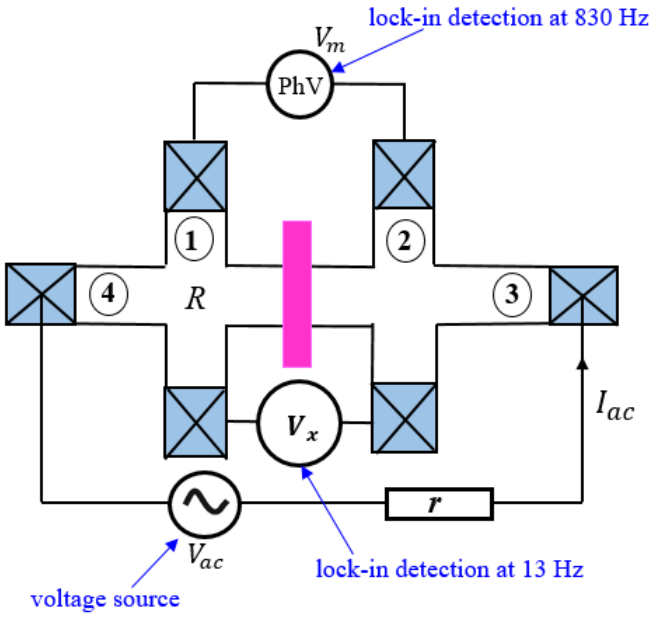

Figure 3.11 A circuit of a 4-terminal measurement of resistance.

MΩ), which is connected to the current probes, 3 and 4 (Figure 3.11). The other benefits of lock-in amplifiers is their ability to demodulate the potential difference at the frequency of microwave modulation, V_x, and to gauge the voltage in the active region of the device, probes 1 and 2 (Figure 3.11).

Thus, the lock-in amplifier includes the output voltage, $V_{x,pp}$, which is proportional to the amplitude of the oscillating potential difference, which can be measured with a voltmeter. However, the measured resistance of the 2DEG is equivalent to $R = V_{x,A}/I_{ac,A} = V_{x,A}/(V_{ac,A}/r)$, the subscript A indicates the amplitude of the alternating voltages and currents. A function generator was also utilized to deliver a pulse signal in kHz to the microwave synthesiser. This stage was crucial to modulate the microwaves, and the modulation causes the photovoltage to oscillate. The modulation frequencies for the modulated microwaves for photovoltage. V_m and modulated current for photoresistance were 830 Hz and 33 Hz respectively. Thus, the LabVIEW software was utilized to vary the magnetic field B_{dc}. We obtained the photovoltage and resistance as a function of B_{dc} or microwave frequency when the latter was varied by the source to be measured.

3.2.1 LabVIEW

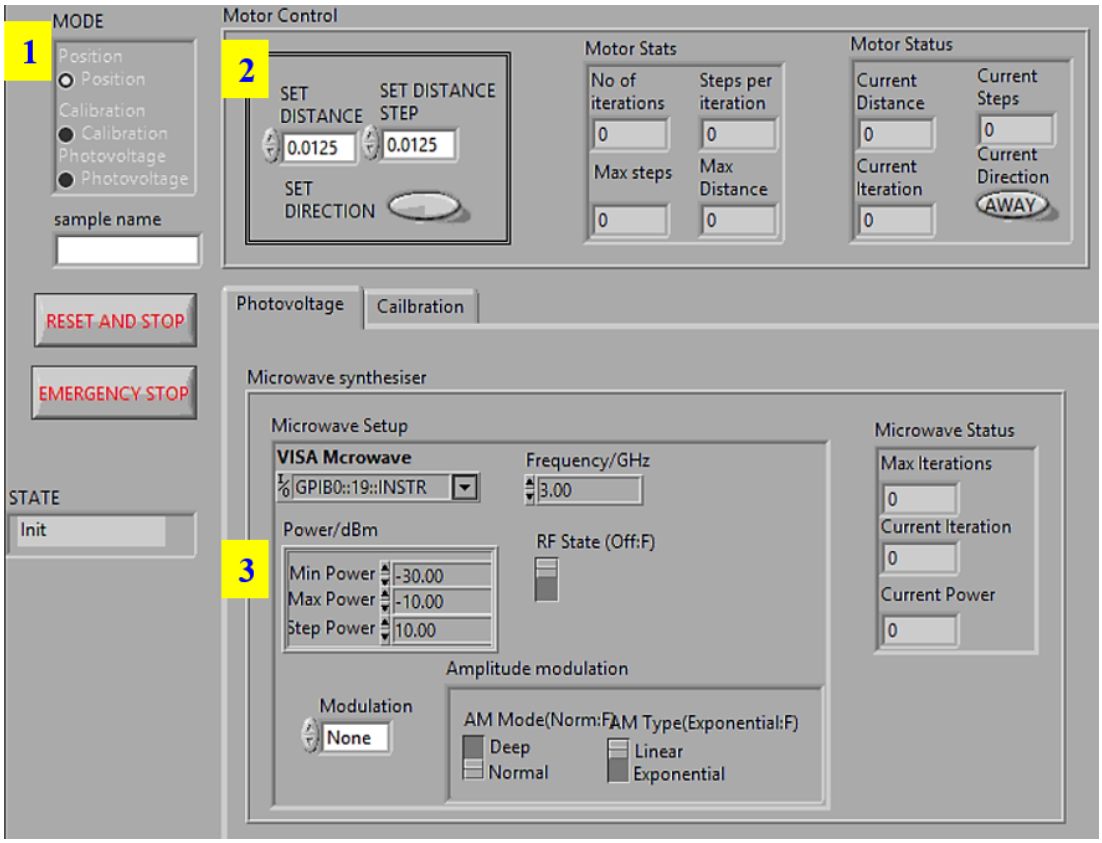

Figure 3.12 The graphical front panel of the LabVIEW program.

LabVIEW is unique software that allows user-friendly computer automation in research conducted by engineers and scientists working on laboratory research and data analysis [99, 100]. In this work, the LabVIEW software was used to control the location of the magnets in the microwave bench and record measurements from multimeters at each position of the magnets. This software also controls different values, such as frequencies and the power level of a microwave synthesiser, and assists with the calibration of magnetic field strength based on the translational displacement of the magnets.

Figure 3.12 shows the graphical front panel of the LabVIEW program that was used to control and observe the progress in the experimental setup and divide it into pats 1, 2, and 3 in yellow colour. Part 1 contains three main modes: the position, calibration, and photovoltage modes. The position mode is used to control the position of magnets and helps to place the magnets at a certain distance from

the sample before photovoltage measurements are taken. Then, the calibration and photovoltage modes are remarkably similar; the distinctions between them are in how they perform measurements. In both modes, the system transfers the magnets a set distance to a new situation to record a measurement then repeats performs this process. The data are recorded at the end of the experiment and saved to a comma-separated-values file for analysis. When working in the calibration mode, the applied magnetic field is recorded for each position of the magnets. A gaussmeter, which is not connected to the LabVIEW software, is used to calibrate the applied field. The gaussmeter readings are then entered into the software for each magnet position. In the photovoltage mode, photovoltage readings and temperatures are recorded directly from each magnet position. Part 2 is for setting the rotation, which is one term corresponding to 0.0125 mm translation of each magnet for different frequencies. Part 3 is for microwave setup that comes from the microwave synthesiser such as 3 GHz at different microwave power value from -10 dBm to -30 dBm and a step power for 10 dBm. The aim of this software is to send a series of pulses to a controller that passes through the stepper motors; each pulse corresponds to a full step of the stepper motor.

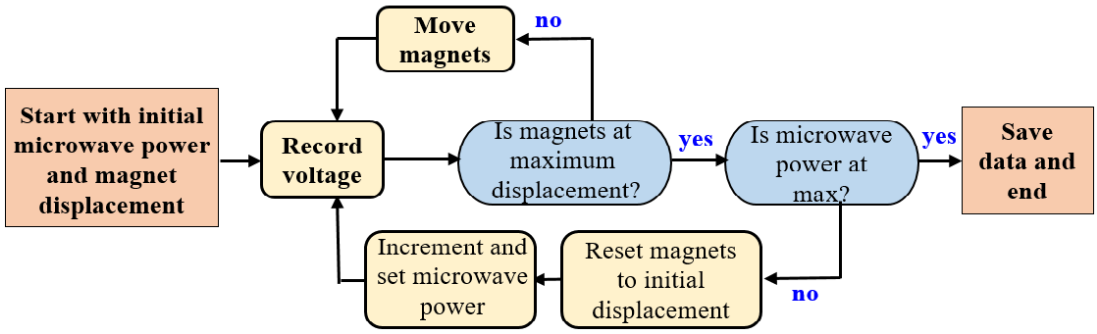

Figure 3.13 A flowchart of the LabVIEW algorithm used to perform photovoltage spectroscopy.

Figure 3.13 depicts a simplified flow chart of the photovoltage spectroscopy process. Starting with the initial state, the software accepts inputs from the user, such as the microwave frequency and the minimum, maximum, and step power of the microwave synthesiser, as well as the maximum distance and step distance for magnet movement. In this situation, several calculations were performed depending on the initial position of magnets, such as how many steps the stepper motors needed to run to move a magnet a step distance, and set up the microwave

synthesiser's frequency, and the lowest microwave power. When the LabVIEW software runs in the photovoltage mode, the program moves to the following state, called Record. In the Record state, the photovoltage spectra are measured and the resulting measurements are saved in memory. Then, the software moves to the Motor state and checks the progress of the magnets. If the magnets have not reached the maximum distance, the magnets are moved a step distance to a new position; the software then takes a reading of the photovoltage and repeats this process. After measurements are taken at each magnet position and microwave power, the LabVIEW software will reach the final state, called Write. In this state, the measuremed data points are plotted as a function of the magnetic distance and microwave power, are saved to a file.

3.3 The Low-temperature Experiment

The experimental technique used to explore low temperature is described below. The first section sets out briefly the underlying basis of cryogenic systems, and is followed by a discussion of measurement Experimental setup in the second section.

3.3.1 Cryogenics

The study used a 4He–bath cryostat with a top-loading variable temperature insert (VTI), suitable for measurements at 1.4 K–300 K and in magnetic fields up to 17 T. The system comprises a liquid nitrogen envelope surrounding a helium bath which contains a superconducting bobbin. The top-loading VTI includes a magnetic field probe that rotates for measurements in perpendicular and parallel directions. The measurement process exploits the temperature and pressure of liquid 4He. The sample, located in the probe, is cooled by thermal conduction into the 4He exchange gas. The flow of liquid 4He from the main bath to the VTI is controlled by a needle valve. The temperature is reduced to 1.4 K by pumping the vapour in the VTI. Figure 3.14 depicts the VTI used in this study. To achieve higher temperatures, an ITC4 heater, obtained from Oxford Instruments, was regulated by controlling the flow of gas. Specially fabricated probes enable this VTI to be used for microwave measurements also. Microwaves are alternating

current frequency signals between 300 MHz and 300 GHz, which correspond to a wavelength between $\lambda = c/f = 1$ m and 1 mm. This study used microwaves ranging from 32.7 GHz to 170 GHz. The microwave sources are backward wave oscillators, also known as backward wave tubes, or as the more sinister-sounding 'carcinotrons'. Fundamentally, they are vacuum tubes used to create microwaves in the terahertz range. Carcinotrons have a broad range of electronic tuning capabilities; they belong to the travelling-wave tube family.

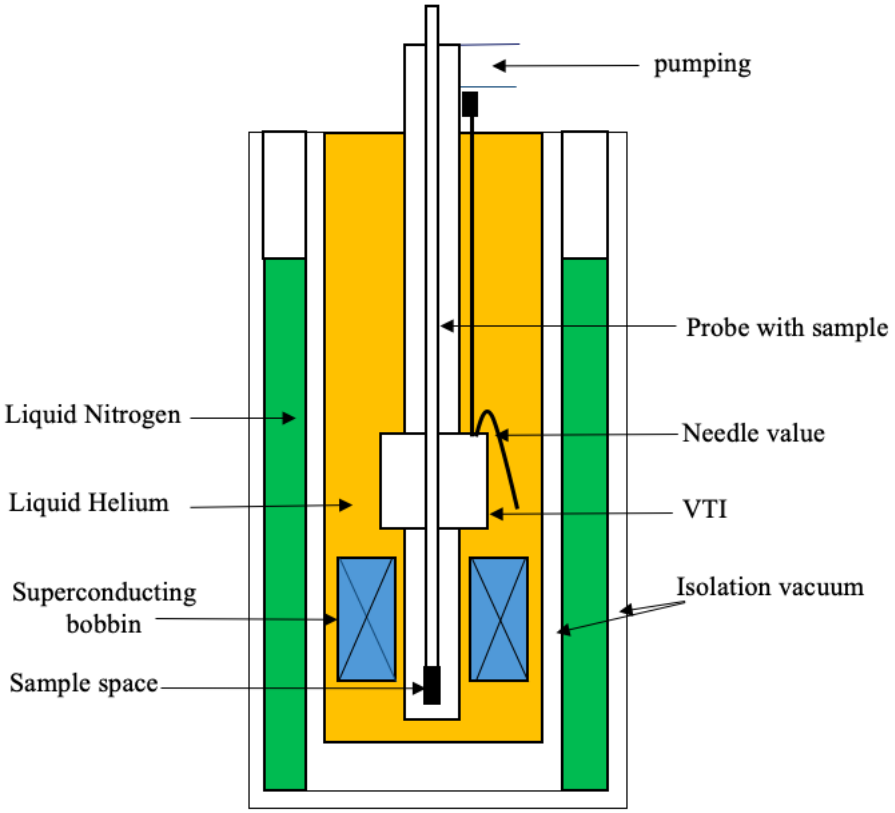

Figure 3.14 The variable temperature insert (VTI).

3.3.2 Low-temperature Experimental setup

To measure microwaves, two different types of probes are fitted to the VTI cryostat system (temperature range from 1.4 to 300 K). Integrated into the probes is a circular waveguide that delivers microwaves from the microwave source to the sample. Figure 3.15 presents the experimental setup. Figure 3.15(a) shows that the microwave generator is fitted with an attenuator. The cylindrical waveguide is

1 mm in diameter and 4.5 m long (Figure 3.15(b)). This design minimises loss of microwave power. A unique device has been used in this study to linearly polarise the microwaves before they impinge on the sample. After passing the attenuator, microwaves pass through a bespoke brass inset whose internal profile converts from a rectangular input to a circular output (see Figure 3.16), "transforms" the output into the circular waveguide. The measurements taken in this study have used indeterminate polarisation; that is, the waveguide was configured with an open circular exit (denoted by the red star in Figure 3.16). That linear polarisation is possible indicates the presence of microwave effects that are sensitive to linear polarisation. Linear polarisation is measurable for generators from 55 GHz to 170 GHz using the specially constructed second brass inset at the end of the waveguide (see Figure 3.16). For all measurements, the waveguide and the sample are separated by 1–2 mm (Faraday configuration).

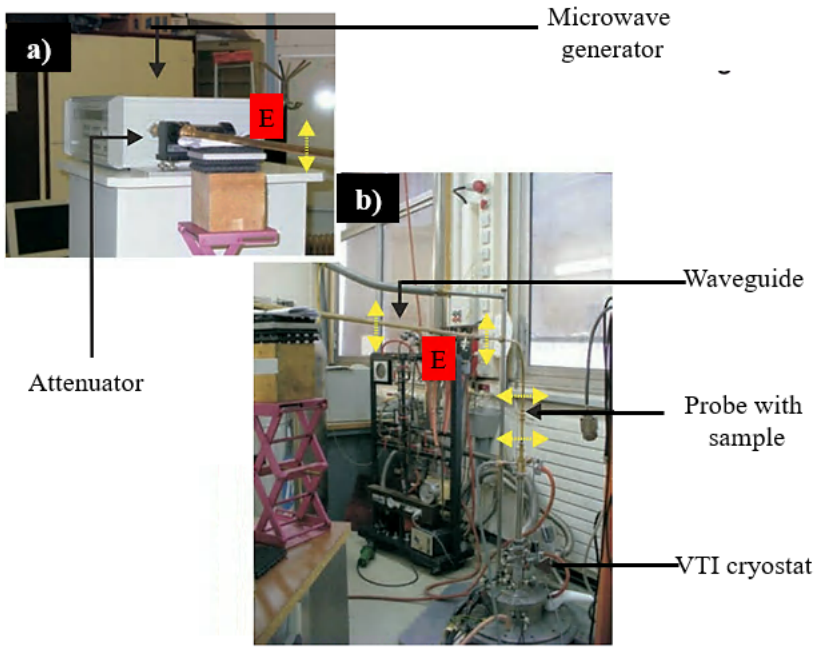

Figure 3.15 a) Setup for microwave experiments: (a) microwave generator with attenuator and (b) VTI with probe and waveguide.

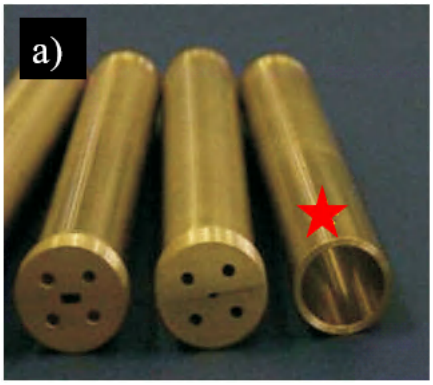

Figure 3.16 Brass inset for the microwave waveguide: By adding such an inset at the end of the waveguide, the microwaves penetrating the sample are linear polarized.

3.4 Micromagnetic Simulation

Object-Oriented MicroMagnetic Framework (OOMMF) is micromagnetic simulation software. The user can define the parameters of the simulation including the size and shape of the material, and the cell size of the simulation mesh. So, it is a powerful program to simulate the dynamics of micromagnetic moments and photovoltage spectra. It is also a combination of discrete magnetic dipoles that occur when an ac wave is applied to an OOMMF programme by applying an external magnetic field to calculate magnetisation and determine the power absorption of magnetic materials. A thorough micromagnetic simulation was utilized to solve the Landau-Lifshitz-Gilbert (LLG) nonlinear time-dependent partial differential equations of the magnetisation, which was given by [101]:

$$\frac{dM}{dt} = -\gamma[M \times H_{eff}] - \gamma\frac{\alpha}{M_s}M \times [M \times H_{eff}] \tag{3.14}$$

where γ is Landau-Lifshitz gyromagnetic ratio, α is the Gilbert damping parameter, and H_{eff} is the effective field which is a combination of the exchange, anisotropy, demagnetization and applied magnetic field. This term consists of two parts, the first part defines the precession of the magnetic moment around the direction of the field which is will continue endlessly in the absence of damping. The second part defines the damping which is the reason for decreasing the

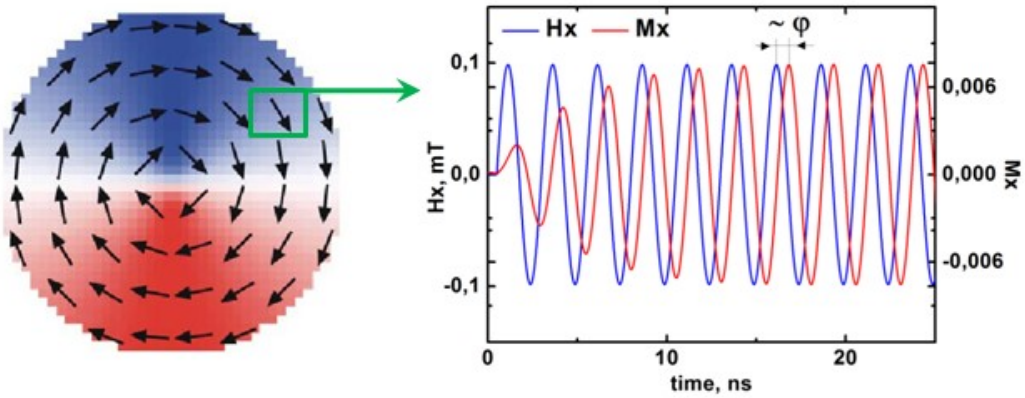

Figure 3.17 An example simulation: disk D= 600 nm, h= 30 nm, vortex ground state; changes in magnetisation were recorded for each cell.

amplitude of the processional motion until it reaches the decay. The damping also acts perpendicular to the direction of motion of the magnetization.

The calculations were carried out by dividing the area into a square or rectangular 3D mesh. To conduct the simulation, a small alternating field B_{ac} was applied, and the variations in magnetisation were recorded. The phase difference φ was held constant between plots (Figure 3.17), which enabled the real and imaginary parts of the magnetic susceptibility to be calculated as follows [102, 103]:

$$\chi = \frac{M}{H} = \frac{M_0}{H_0}\cos\varphi + \frac{M_0}{H_0}\sin\varphi\frac{\cos\omega t}{\sin\omega t} \tag{3.15}$$

$$\acute{\chi} = \frac{M_0}{H_0}\cos\varphi \tag{3.16}$$

$$\chi^{''} = \frac{M_0}{H_0}\sin\varphi \tag{3.17}$$

$$\chi = \acute{\chi} + i\chi^{''} \tag{3.18}$$

where $M(t)$ is the periodic magnetic response, $H(t)$ is the periodic magnetic field, with known microwave angular frequency ω and estimated phase differences φ. Equation 3.16 calculates real susceptibility, $\chi^{'}$, which gives the speed at which the electromagnetic wave is propagated in the magnet, as well as imaginary susceptib-

ility, χ'', which corresponds to the absorption of microwave energy, Equation 3.17. The magnetisation of Co was excited by the alternating magnetic in the presence of a constant field, B_{ac}, and the constant field B_{dc} was applied along the short side of the stripe with a geometry of 2040 × 220 × 40 nm, which was meshed by 5 × 5 × 40 nm.

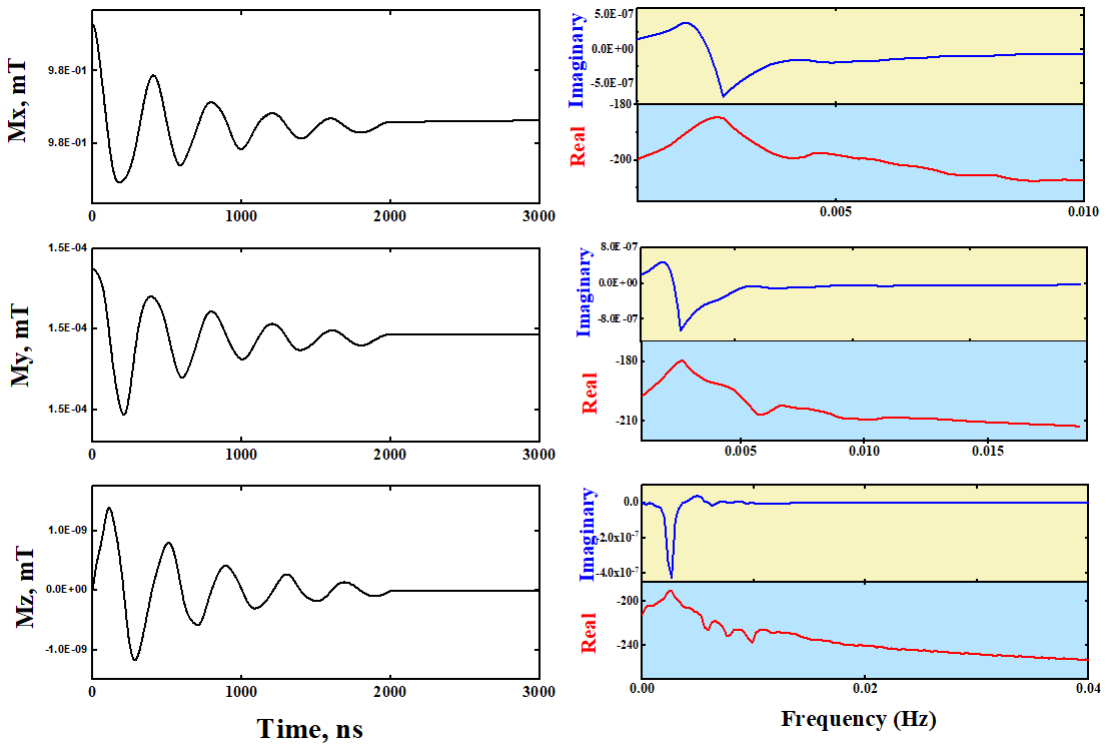

Figure 3.18 The recorded magnetic response for the strip of Co as a for the whole object, and the calculation of the spectral dependence of the real and imaginary susceptibility as a function of magnetisation in the x, y, and z–direction.

Variation in the magnetic field B_{dc} will be shown later in the results part, in steps of 0.025 T (Figure 3.18). The relaxation of the system occurred 0.2 ns after each change over 20 periods of the alternating field B_{ac}=B_0 sin(ωt) [104]. A magnetic simulation was executed for different frequencies in the magnetic stripe in the cases of amplitude of the alternating field $B_{ac} = 1 \times 10^{-5} T$.

The magnetic simulation was then repeated with a Co disk measuring 80 × 80 × 40 nm, with a mesh of 2 × 2 × 40 nm, using OOMMF for the calculation. The standard parameter values of cobalt were used: saturation magnetisation, M_s = 1.4 ×10^6 A/m, exchange interaction constant $A = 30 \times 10^{-12}$ J/m, and the

damping parameter $\alpha = 0.5$ [105]. Since sputtered cobalt films are polycrystalline, there is no average magnetocrystalline anisotropy and $K_1 = 0\ J/m^3$ [106, 107, 108]. Most parameters that determine magnetization such as Gilbert damping of Cobalt, saturation magnetization, exchange energy, uniaxial anisotropy energy are determined by spin interactions at the level of interatomic distances and therefore are the same whether Co is monocrystalline or polycrystalline.

However, when doing spin resonance the axis of anisotropy is different in each 30 nm or so microcrystal of evaporated Cobalt. Therefore while in each microcrystal the parameters are the same as described in the above paragraph, in the polycrystal, one needs to define average value of the constant of anisotropy and average magnetization axis to interpret the macroscopic spin resonance results at the level of the sample. The dynamic characteristics of a nanostructure can be defined using fast Fourier transformation (FFT); it is crucial to obtain the imaginary susceptibility $\chi^{''}$ as a function of the magnetic field (see Equation 3.17) to describe the phase shift of the magnetisation and the microwave field (Figure 3.18) [109]. These values have been compared with experimental absorption. As a result, the power was absorbed per unit volume P demonstrated the relationship with imaginary susceptibility as [45, 46, 110]:

$$P = \frac{1}{2}\omega\chi^{''}{H_0}^2 \tag{3.19}$$

This equation demonstrates the relationship between power absorption by local spin-wave modes and the local imaginary susceptibility, which can be used to approximate the photovoltage line shape. The spatial map of the imaginary susceptibility shows the power absorbed over the sample at resonance.

Chapter 4

Ferromagnetic Resonance of the Individual Stripe

The ferromagnetic resonance theory was described in Section 2.7. Our experimental results demonstrating confined spin-wave modes are presented and discussed in this chapter. This work demonstrates photovoltage spectroscopy as a novel technique for detecting spin dynamics in submicron magnets. A magnetised cobalt stripe generates an inhomogeneous internal magnetic field, which confines localised spin wave modes near the poles. We show that a two-dimensional electron gas (2DEG) is highly sensitive to the dynamics of localised spin waves bound to the surface and interfaces of ultrasmall magnetic elements.

Our results exhibit Damon–Eshbach modes that propagate along the long edge parallel to the dc magnetic field at different frequencies and low temperatures. Localised dipolar edge spin waves are observed in a magnetic field perpendicular to the long edge. Strong bulk-edge mode coupling is occurs as a bonding-antibonding gap at resonance. These experimental measurements were compared to micromagnetic simulation results using the OOMMF. Our photovoltage technique can detect the resonance of localised magnetic moments through the eddy currents induced by the alternating stray magnetic field in a high mobility 2DEG. In addition, we studied the photovoltage under multiple conditions of varying the magnetic field orientation, B_{dc}, and geometry of the nanomagnets. The effect of the magnetocrystalline anisotropy on ferromagnetic resonance is also investigated.

4.1 Results

The purpose of photovoltage measurements at 77 K under a high magnetic field on Hall bars decorated with Co stripe was to examine the sensitivity of the device and spectral response prior to looking to 1.3 K. Multiple room temperature measurements were performed involving the calibration curve of the magnetic field as a function of distance to measure the microwave power spectrum using photovoltage spectroscopy at 300 K.

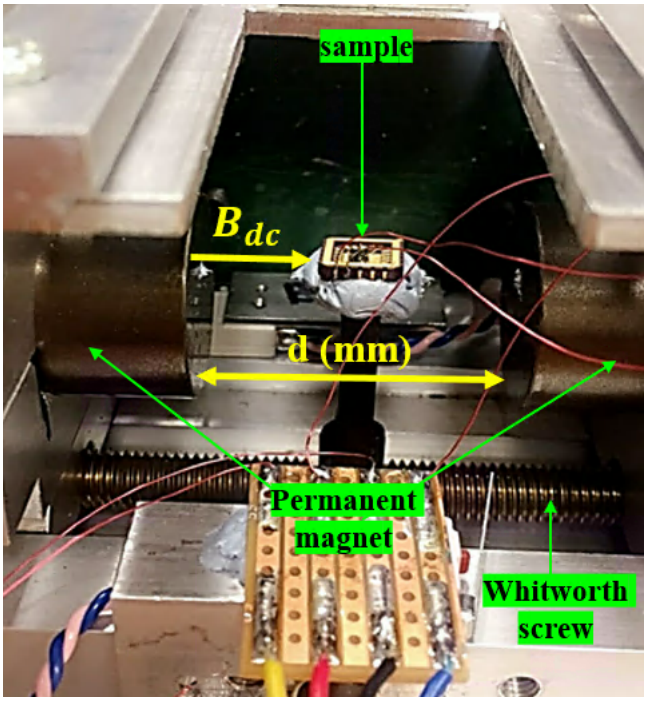

Figure 4.1 Side view of the rig consisting of two permanent magnets; the sample is placed at the centre of the bench, and the Whitworth screw displacing magnets horizontally.

4.1.1 Calibration Curve B_{dc} versus Distance

The purpose of these experiments was to calibrate the magnetic field to magnetic displacement and microwave frequency. A calibrated Hall junction measured the magnetic field, B_{dc}, produced by the NdFeB magnets as a function of the distance between the magnets (Figure 4.1). The calibration curve $B = f(d)$, representing

the magnetic field decay when the magnets are moved away from the sample. The measurement was taken using a Hall probe incremental value at the half distance between magnets as shown in Figure 4.2. For example, at a displacement of 44.75 mm, the magnetic field is 0.1 T corresponding a resonance frequency of 3 GHz whereas at 31 mm, the magnetic field is 0.2 T corresponding to 6 GHz. All these values can be calculated using Equation 2.22.

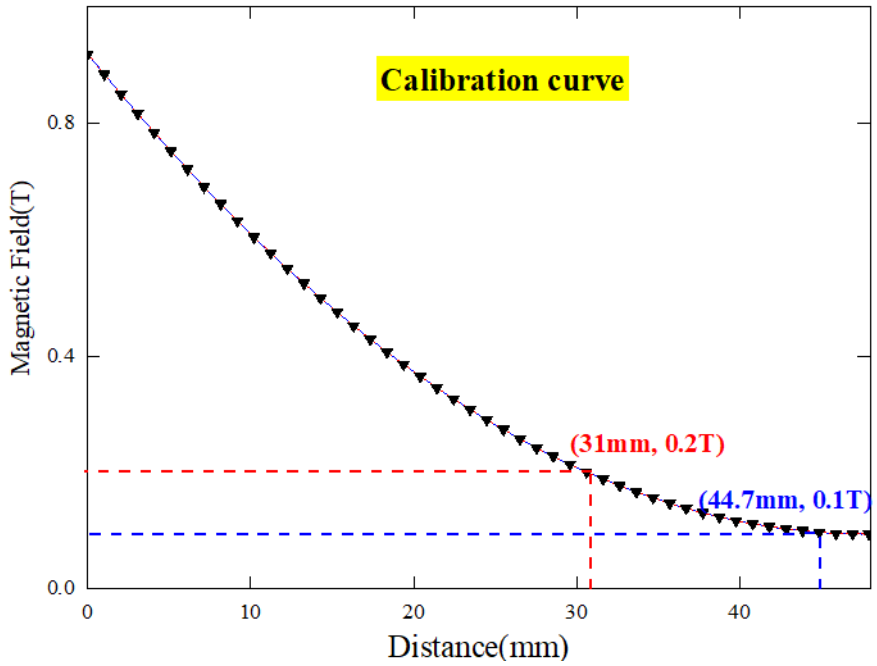

Figure 4.2 The calibration curve of the magnetic field according to the distance between two permanent magnets. Measured with a Hall probe incremental value at the half distance between magnets

4.1.2 Photovoltage Measurements at 300K

We perform photovoltage measurements at 300 K on Hall bars decorated with Co stripe to demonstrate the sensitivity of the Hall sensors to microwaves at room temperature. The measurements were achieved by placing the sample into the microwave cavity and sweeping the external magnetic field, B_{dc}. We varied microwave frequency between 3 and 21 GHz to determine the position and width of the resonance absorption peak for bar magnets. We irradiated the samples using microstrip antenna by sending the train of control signals through LabVIEW to

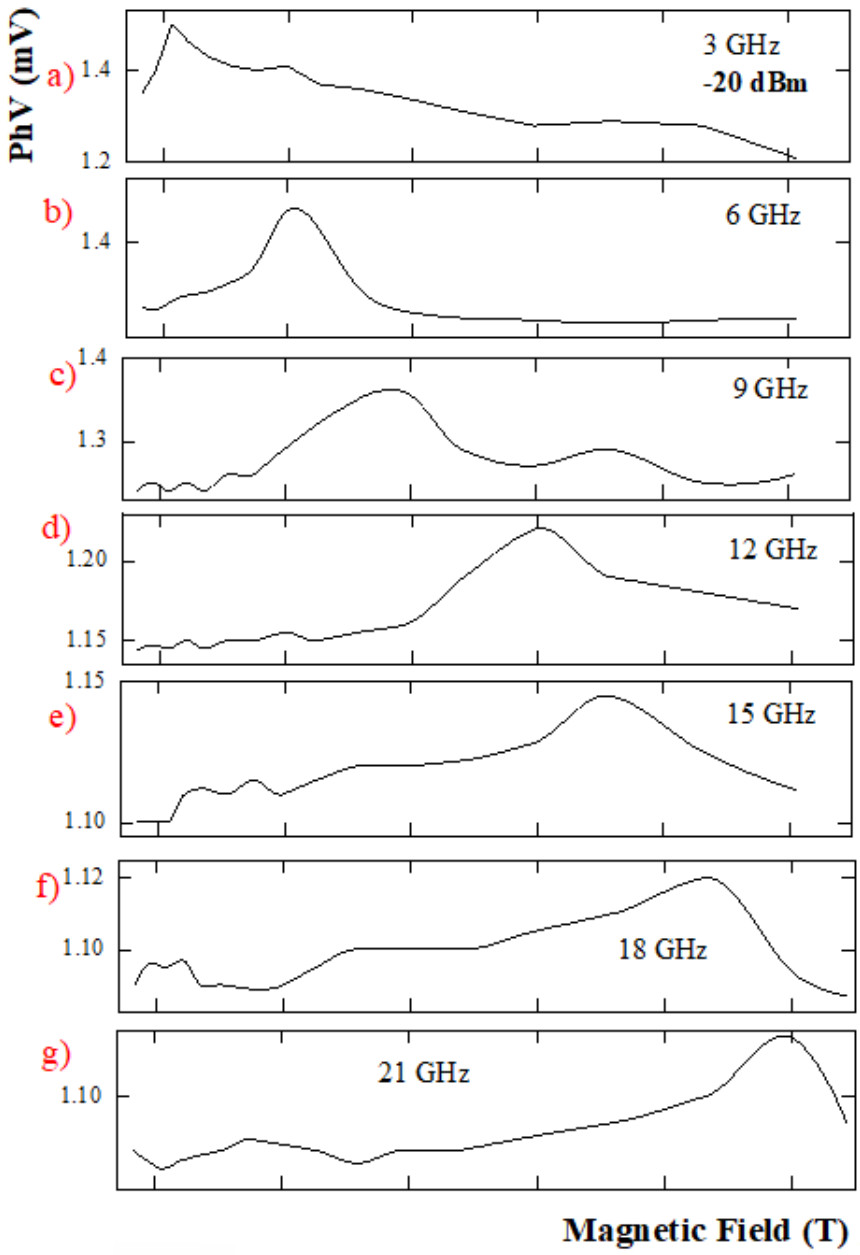

Figure 4.3 Experimental results of photovoltage measurements as a function of magnetic field at 300 K with power -20 dBm at different frequency for sample $[Ta(30A), [Co/Ni]_{\times 9}]_{x2}$, a) 3 GHz, b) 6 GHz, c) 9 GHz, d) 12 GHz, e) 15 GHz, f) 18 GHz, g) 21 GHz.

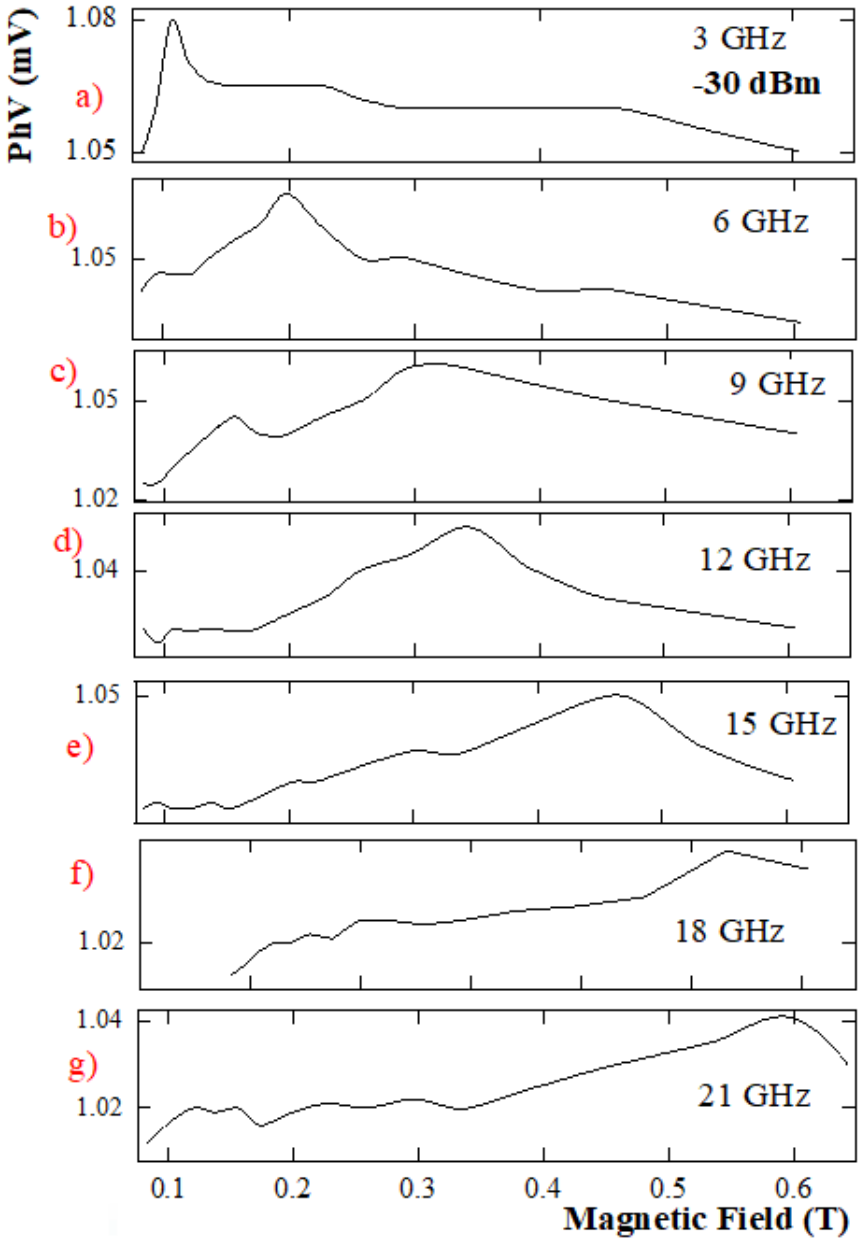

Figure 4.4 Experimental results of photovoltage Measurements as a function of magnetic field at 300 K with power -30 dBm at different frequency for sample $[Ta(30A), [Co/Ni]_{\times 9}]_{x2}$, a) 3 GHz, b) 6 GHz, c) 9 GHz, d) 12 GHz, e) 15 GHz, f) 18 GHz, g) 21 GHz.

the microwave generator in continuous wave mode (CW). We used a range of microstrip antenna, PCB, to cover the range 3 GHz to 21 GHz. The microwave power was -20 dBm to maintain the experiment at a safe level which is equal to 10 μWatt, and -30 dBm is equal to 1 μWatt. These experiments involved modulating the microwaves and demodulating the resulting photovoltage with a lock-in amplifier at a modulation frequency of 830 Hz to remove noise and background signals as explained in Section 3.1.2. A lock-in detector was used to pick up the voltage between 8 μm probes of the Hall bar device and feed the analogue output into the digital multimeter, which can be read by LabVIEW. As shown in Figure 4.3 (a), at 3 GHz the peak position is at 0.11 T experimentally. This matches the position of the theoretical peak at 0.1 T. At 6 GHz, the experimental peak position was observed at 0.21 T, and predicted to be at 0.2 theoretically using Equation 2.22, as shown in Figure 4.3 (b). Meanwhile, Figure 4.3 (c) exhibits the results at 9 GHz, where the peak position is at 0.29 T experimentally compared to the theoretical peak at 0.3 T. At 12 GHz the experimental and theoretical peaks are at 0.4 and at 0.4, respectively, as shown in Figure 4.3 (d). At 15 GHz, the experimental peak position at 0.46 T corresponds to the theoretical peak at 0.5 T, and at 18 GHz, the experimental and theoretical peaks are at 0.54 T and 0.6 T, respectively, Figures 4.3(e) and 4.3(f). Finally, at 21 GHz, the experimental peak position of 0.61 T is near the predicted peak at 0.7, Figures 4.3(g).

To identify the effect of varying power on the micromagnetic stripe, Figure 4.4 displays the same information at Figure 4.3, but at -30 dBm instead of -20 dBm. The experimental peaks shown in Figure 4.4 correspond to the theoretical peaks located at 0.11, 0.2, 0.31, 0.35, 0.46, 0.54 and 0.61 T for 3, 6, 9, 12, 15, 18 and 21 GHz, respectively. The values of the resonances markedly shift with increasing microwave frequency. Thus, there is a good agreement between theory and experiment at low frequency, but less agreement at higher frequency. The devices work better and are more sensitive at low temperatures, explaining the better agreement at low temperature.

On the other hand, the amplitude of the resonance at 3 GHz is about 0.2 mV at -20 dBm, while at -30 dBm it is approximately 0.031 mV, as shown in Figures 4.3(a) and 4.4(a). At 6 GHz, the amplitude is about 0.18 mV at -20 dBm and 0.03 mV at -30 dBm, as shown in Figures 4.3(b) and 4.4(b). The amplitude of

the resonance at 9 GHz and 12 GHz at -20 dBm are about 0.13 mV and 0.09 mV, respectively (Figures 4.3(c) and 4.3(d)), while at -30 dBm they are around 0.029 mV and 0.027 mV, respectively (Figures 4.4(c) and 4.4(d)). These results show good agreement between the experiment and the theory, which predicted that the amplitude of the resonances would decrease with decreasing power, as explained in Section 3.1.3, Equation 3.11.

However, the bandwidth of the peak resonance becomes wider with increasing frequency as measured by the full width at half maximum FWHM. FWHM is an expression of the extent of function given by the difference between the two extreme values of the independent variable at which the dependent variable is equal to half of its maximum value. In theory, the bandwidth is proportional to the resistance of the waveguide, and the waveguide is the resistor. The resonance is defined by the inductance (L) and capacitance (C) between the parallel plates, which will create the RLC circuit. When we apply a microwave frequency, the resonance frequency of the peak is:

$$\omega_0 = 2\pi f_0 = \frac{1}{\sqrt{LC}} \tag{4.1}$$

where the resonant frequency, ω_0, is expressed in natural units (radians per second). The Q factor can be defined as the frequency-to-bandwidth ratio of the resonator:

$$Q = \frac{f_0}{\Delta f} = \frac{1}{2\pi R\omega_0} \tag{4.2}$$

Here, f_0 is the resonant frequency, Δf is the bandwidth of the resonance and R is the resonance of the waveguide. Thus, we can calculate Δf using the following equations:

$$\Delta f = \frac{f_0}{Q} = \frac{2\pi R\omega_0}{2\pi\sqrt{LC}} = \frac{R}{\sqrt{LC}}\omega_0 = \frac{R}{LC} \tag{4.3}$$

Thus,

$$\Delta f = R \times \omega_0^2 \tag{4.4}$$

Figure 4.5 plots the calculated relationship between $\sqrt{\Delta f}$ and ω_0. At $f = 3$ GHz, $\sqrt{\Delta f}$ is 1.37 GHz and $\omega_0 = 18.84\ rad/s$, while at 12 GHz, $\sqrt{\Delta f}$ is 2.74 GHz and ω_0

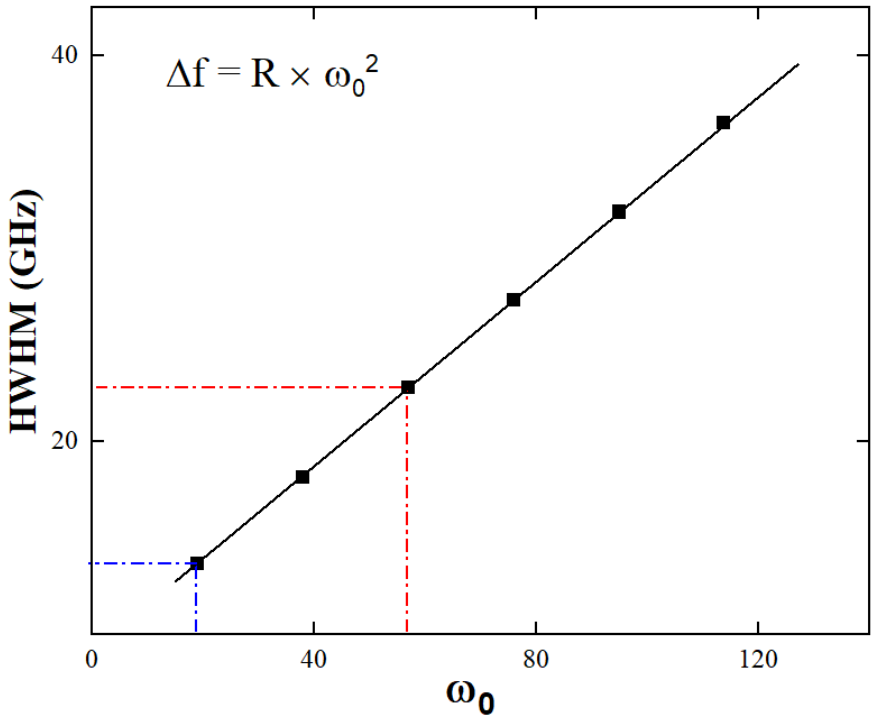

Figure 4.5 The calculations of the square root of the bandwidth as a function of the resonance frequency at different frequencies.

$= 75.36\ rad/s$. This is compared to the experimental $\sqrt{\Delta f}$ = FWHM extracted from Figure 4.4 and displayed as the symbols in Figure 4.5. Each experimental observation of the signal bandwidth increases with the frequency and is in good agreement with the corresponding calculated values shown in Figure 4.5.

4.1.3 Photovoltage Measurement at Low-temperature

The results presented in this section were obtained using the experimentala Hall bar decorated with individual cobalt stripes that are 80 nm wide and 30 nm thick. At low magnetic field, the sample was refrigerated to 1.3 K. Furthermore, in such experiments, microwaves were guided by an overmoded waveguide to the sample space of a 17 T superconducting magnet. This experiment has been performed in Grenoble by Alain Nogaret, Maksym Steblyi, and Jean–Claude Portal. The Co micromagnets were magnetised with an external magnetic field B_{dc} in-plane with respect to the sample. When the Co stripe is magnetised, magnetic poles are formed in the facets perpendicular to the field B_{dc}. The sample was cooled

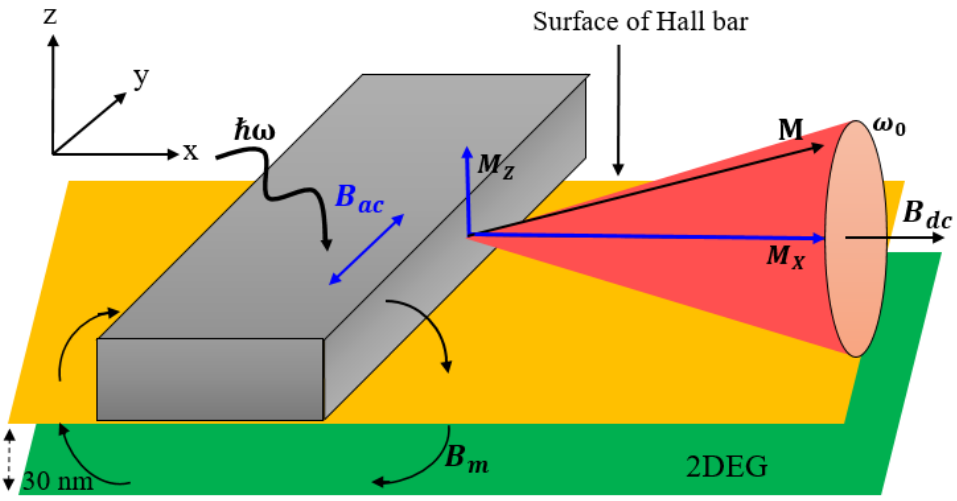

Figure 4.6 Schematics of the magnetic stripe (Co) magnetised in the plane of the 2DEG by B_{dc} and driven to resonance by B_{ac}. Magnetic moments M undergo precession at frequency ω_0 in magnetic field B_{dc}.

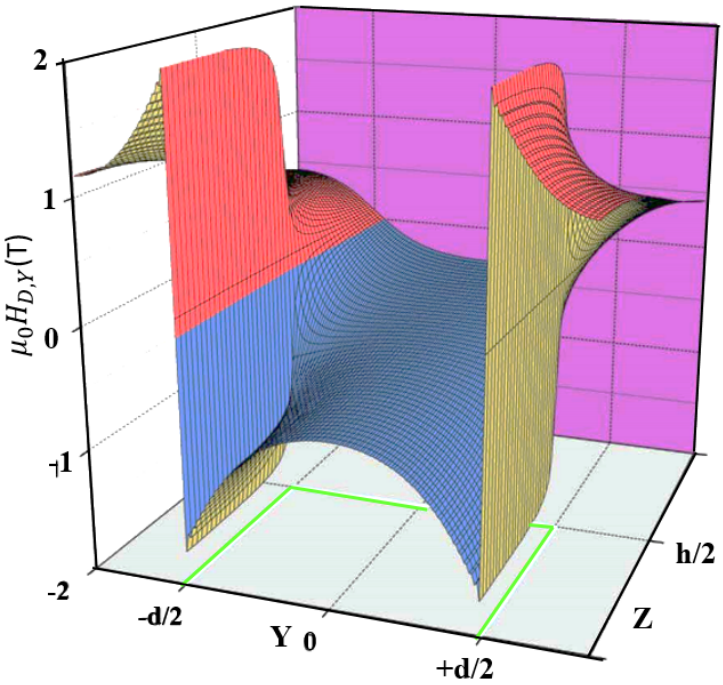

Figure 4.7 The spatial variation of the in-plane dipolar magnetic field in the cobalt stripe. The superlattice is supposed to be magnetised to saturation along y. The edges of the stripe are indicated by the full lines in the y0z plane. Adapted from ref [3]

down using liquid helium and preserved at 1.3 K by a variable temperature insert [111]. A collection of backward wave oscillators was used to generate microwaves over frequencies ranging from $f = \omega/2\pi = 30$ to 130 GHz. The magnetic field component of these microwaves, B_{ac}, drives spin resonance and the oscillations of the magnetisation induce a Faraday electric field that generates ac currents in the 2DEG which induce an alternating fringe field B_m at the site of the 2DEG [112, 85]. B_m deflects eddy currents via the Hall effect along the orientation perpendicular to the magnetic stripe. The rectified Hall voltage generated across the magnetic stripe is [113]:

$$PhV = \mu_0 \mu^2 S \langle M_z \dot{M}_x - M_x \dot{M}_z \rangle \tag{4.5}$$

where μ is the electron mobility in the 2DEG, μ_0 is the magnetic permeability, S refers to the effective surface, which is approximately the square of the decay length of the stray magnetic field, and M_x and M_z are magnetisation components (Figure 4.6). Considering the effect of the static magnetic field B_{dc} applied either parallel or perpendicular to the magnetic stripe, the Co magnetisation precesses at a frequency ω_0, which is proportional to the magnitude of the field B_{dc}. At resonance $\omega = \omega_0$, the magnetisation oscillates back and forth parallel and antiparallel to B_{dc}, giving rise to the photovoltage peaks in accordance with Equation 4.5 and the resonance condition of localised spin-wave excitations was explained in Section 2.7.2. Under the conditions of resonant with B_{dc} is parallel to x, the oscillations of magnetisation components M_y and M_z induce stray radio frequency magnetic fields at the site of the 2DEG. However, in the large magnet, we can ignore the spins effects at the edge compared to the bulk, however in the nanomagnet, the edge play a key role in magnetic properties. We further will represent the effect of the orientation of the dc magnetic field which is parallel or perpendicular to the long edge of the nanomagnet (Co stripe).

4.1.3.1 B_{dc} parallel to the long axis of Co stripe

In the case presented in this study, we used the experimental setup that we were explained at Section 3.1.2 with cooling the sample until 1.3 K. The magnetostatic boundary conditions are the spin-wave modes to the surface of the magnets. The

stripe then exhibits a backward volume magnetostatic waves modulated by Damon–Eshbach modes, which propagate along the edges parallel to B_{dc}, meaning that the dynamic amplitude of the precession is distributed across the thickness [114, 115]. These resonant peaks are indicated by several distinct arrows labelled I, II, and III at frequencies: 35 GHz, 41 GHz, 55 GHz, 75 GHz and 95 GHz in Figures 4.8 and 4.9.

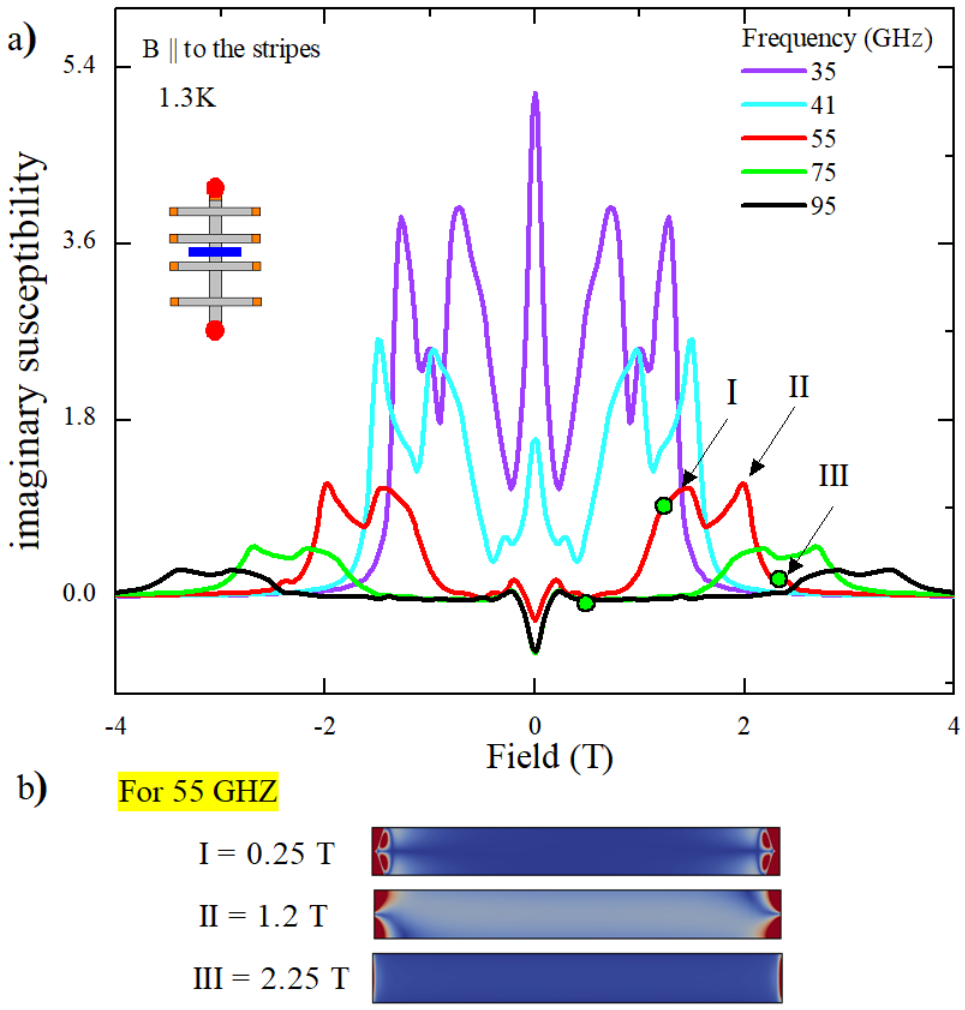

Figure 4.8 a) The calculation of the imaginary susceptibility in parallel magnetic field, B_{dc}, at different frequencies: 35 GHz, 41 GHz5, 55 GHz, 75 GHz, and 95 GHz. b) Spatial distribution of magnetisation oscillation amplitude for different resonance peaks at 55 GHz.

Quantitatively, Figure 4.8(a) implies the OOMMF calculation of imaginary susceptibility depending on the frequency identifieds peaks corresponding to the po-

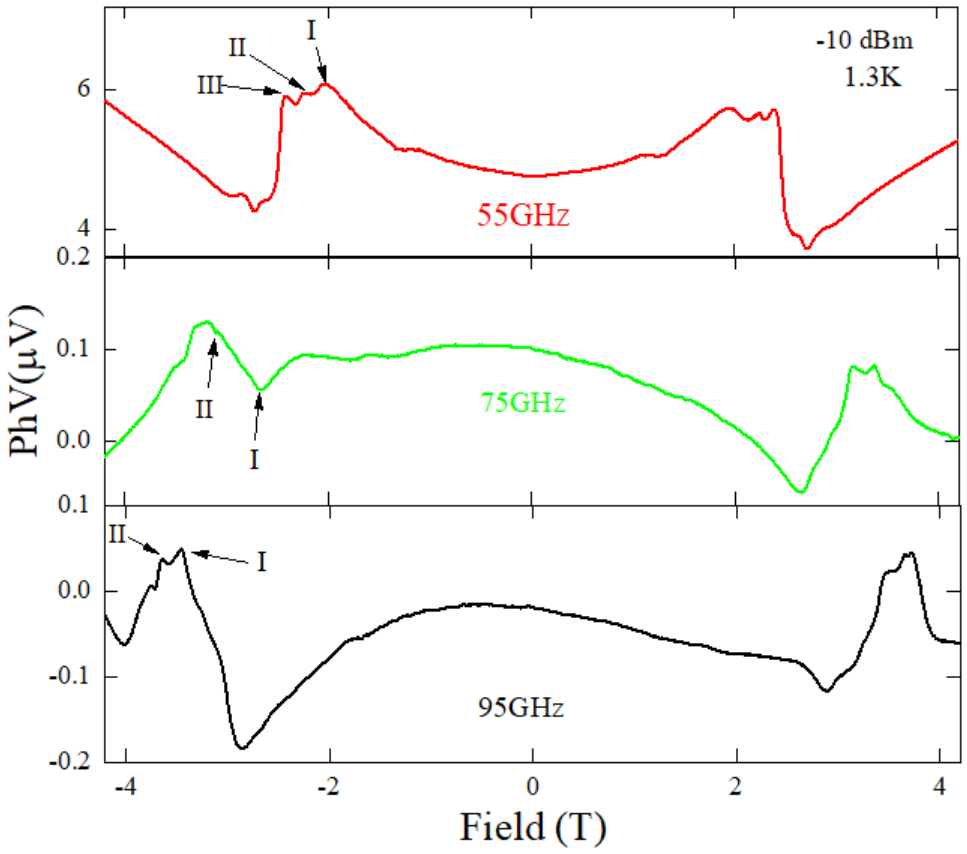

Figure 4.9 Experimental dependence of the photovoltage with B_{dc} parallel to the stripes at different frequencies 55 GHz, 75 GHz and 95 GHz at -10 dBm of power. The stripe then exhibits a backward volume mode modulated by Damon–Eshbach modes, which propagate along the edges parallel to B_{dc}. Several distinct peaks are labeled I , II, and III corresponding to various quantized spin-wave modes.The amplitude of the resonance decreases with increasing frequency. T = 1.3 K. The magnetic element is not perfectly centred on the Hall bar which can give asymmetry with respect to change of sign of the magnetic field.

sitions of $B_1 = 0.73$ T (I), $B_2 = 1.00$ T (II) and $B_3 = 1.25$ T (III) at 35 GHz, $B_1 = 0.98$ T and $B_2 = 1.46$ T at 41 GHz, $B_1 = 1.4$ T, $B_2 = 1.98$ T and $B_3 = 2.34$ T at 55 GHz, $B_1 = 2.13$ T and $B_2 = 2.7$ T at 75 GHz, and $B_1 = 2.8$ T and $B_2 = 3.38$ T at 95 GHz. It is seen that at low frequencies, the spectrum exhibits several peaks but, as frequency increases, the separation between peaks increases according to equation (2.22) that explained the peak positions which is same at the negative and positive. The susceptibility amplitude of the first resonant peak at 35 GHz and 41 GHz are $\chi^{''} = 2.2$ and $\chi^{''} = 1.22$, respectively. Meanwhile, the peak amplitude of the first peat at 55 GHz is $\chi^{''} = 0.4$ but the amplitude of the first resonant peak at 75 GHz is $\chi^{''} = 0.2$ and the amplitude at 95 GHz is $\chi^{''} = 0.06$. Figure 4.8(b) depicts Spatial distribution of magnetisation oscillation amplitude for different peaks at 55 GHz at 0.25 T, 1.2 T and 2.25 T that corresponding to the green circles at Figure 4.8(a).

Figure 4.9 demonstrates the position of ferromagnetic resonance in the experimental photovoltage which are $B_1 = 2$ T, $B_2 = 2.2$ T and $B_3 = 2.43$ T at 55 GHz, $B_1 = 2.6$ T and $B_2 = 3.1$ T at 75 GHz, and $B_1 = 3.4$ T and $B_2 = 3.6$ T at 95 GHz. Therefore, the internal magnetic field of the peaks at different frequencies can be calculated through Equation 2.22 for one of the peaks and there are some additional peaks. In additions, the amplitude of the first resonant peak at 55 GHz is 0.15 μV but at 75 GHz, the amplitude is about 0.03 μV while at 95 GHz, the amplitude of resonances is around 0.011 μV. By comparing the position and the amplitude of resonance, there is an agreement between theory and experiment, when we increase the frequency, the magnetic field and the position of the peak will be increased and shifted as well. The magnetic element is not perfectly centred on the Hall bar which can give asymmetry with respect to change of sign of the magnetic field. As can be seen in Figures 4.8 and 4.9, the experimental resonances are shifted to the higher magnetic field by the magnetocrystalline anisotropy of Co whereas magnetocrystalline anisotropy is difficult to include in OOMMF calculations because the Co film is polycrystalline. This shift is $H_c = 2K_u/M_S\mu_0 =$ 0.6 T at 55 GHz, 0.47 T at 75 GHz, and 0.6 T at 95 GHz. The average of shifting is about +0.5 T, where $K_u = 5.5 \times 10^5 J\mathrm{m}^{-3}$, at low temperature.

Meanwhile, the amplitude of the resonant peaks increases with decreasing frequency, which agrees well with the theory that expounded in Section 3.3 (Equa-

tion 3.19). Both the amplitude of resonant peaks in micromagnetic simulation and in the photovoltage spectroscopy decreases with increasing frequency. This is because, although the microwave power P remained constant, $P = n \times \hbar\omega$, the increase in photon energy $\hbar\omega$ caused the number of photons n to decrease. The amplitude of resonance is proportional to the number of the photon which is absorbed. This is why the amplitude of resonant peaks decreases with increasing frequency. However, the dispersion curve of Damon-Eshbach modes is discussed in detail in Section 2.7.2.1.

However, the reasons for comparing the photovoltage peak with the simulations for the imaginary susceptibility are that Equation 4.5 expresses a proportional relationship with the average of the magnetisation, and that the imaginary susceptibility has a proportional relationship with the magnetisation which is always perpendicular and dissipative $\chi^{''} = M_{\perp}/H$ whereas the real susceptibility is always parallel in a complex plane $\chi^{'} = M_{\parallel}/H$.

4.1.3.2 B_{dc} is Perpendicular to the Long Axis of the Co Stripe

In the chapter on localised spin wave excitations, we then observe an experimental spin-wave resonance of the magnetic stripe at various frequencies at 1.3 K. The creation of confined spin waves involves the quantum mechanical exchange interaction and classical confinement by the magnetostatic potential. The exchange interaction aligns spin chains of itinerant electrons. The magnetostatic potential creates the boundary conditions confining the spin waves. The discrete energy levels produced in the confinement of spin are comparable to those of electrons which are confined in a narrower quantum well as described in Figure 2.20.

The investigation now focuses on the impact of applying B_{dc} perpendicular to the long axis of the magnetic stripe. The spin waves were confined to the opposite edges and overlapped to create a localised bonding state at the centre of the stripe and a localised antibonding state at the site of the two magnetic wells at the edges. These bonding states are the main peaks that occur at the low magnetic field while the antibonding states are the minor peak, as indicated by the arrows labelled I and II, respectively, (Figures 4.10 and 4.11).

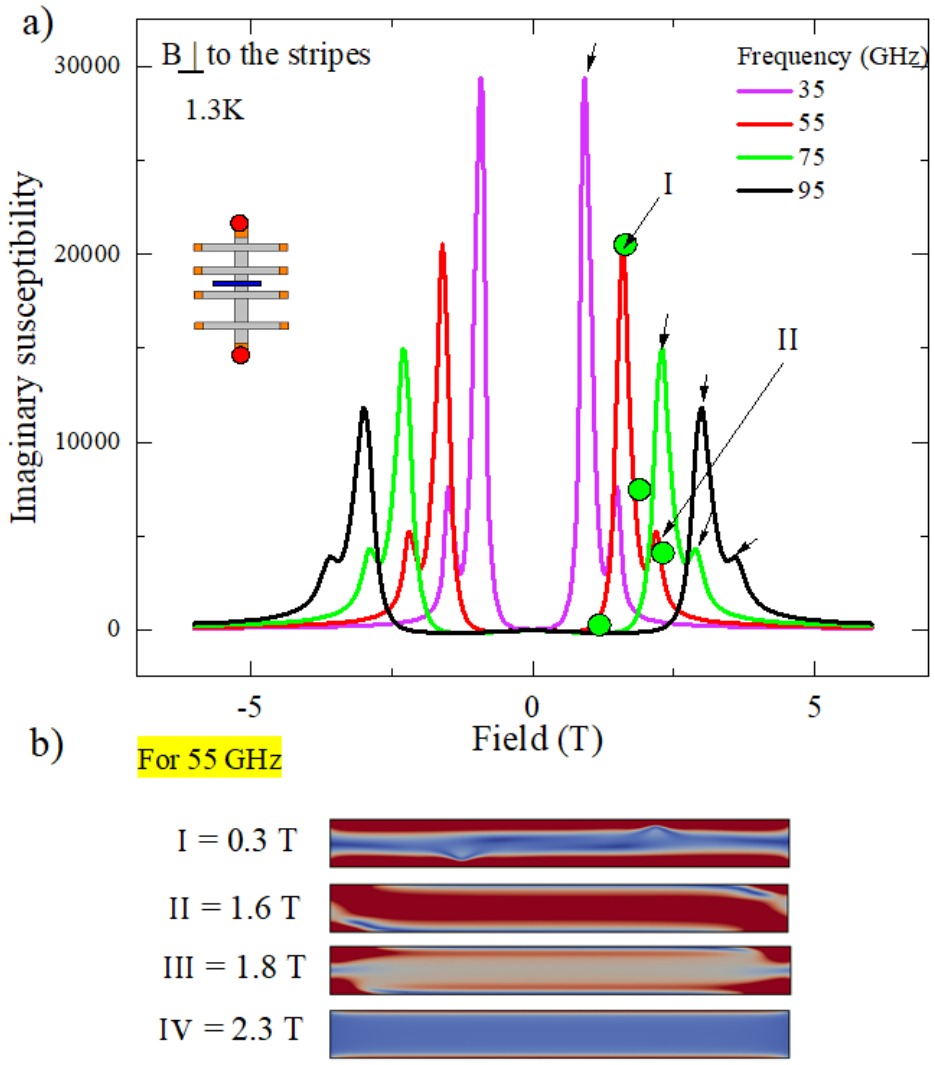

Figure 4.10 The calculation of the imaginary susceptibility in perpendicular magnetic field, B_{dc}, at different frequencies: 35 GHz, 55 GHz, 75 GHz, and 95 GHz. b) Spatial distribution of magnetisation oscillation amplitude for different resonance picks at 55 GHz.

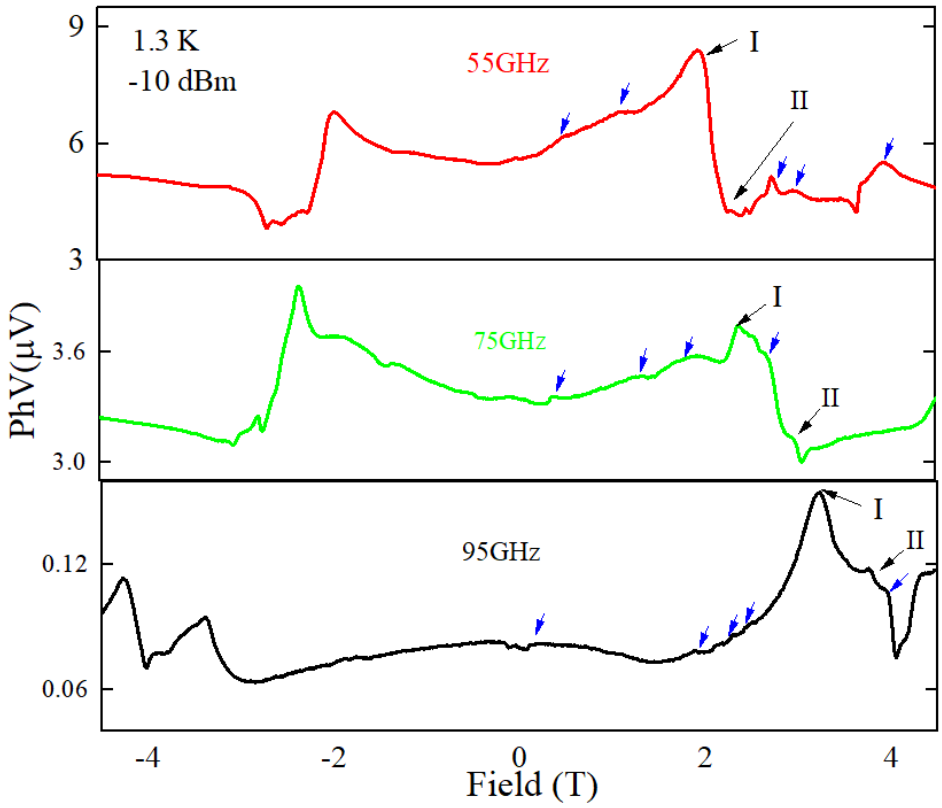

Figure 4.11 Experimental dependence of the photovoltage with B_{dc} perpendicular to the magnetic stripes at -10 dBm at 55 GHZ, 75 GHz and 95 GHz. The bonding states are the main peaks that occur at the low magnetic field while the antibonding states are the minor peak, as indicated by the arrows labelled I and II, respectively. The amplitude of the resonance decreases with increasing frequency. T = 1.3 K

Figures 4.10 and 4.11 provides an instructive comparison between the location of the peaks from the simulation and experiment for various frequencies. Figure 4.10(a) predicts the precise position of the resonances for the micromagnetic simulation (OOMMF) at $B_1 = 0.91$ T and $B_2 = 1.49$ T at 35 GHz, $B_1 = 1.61$ T and $B_2 = 2.2$ T at 55 GHz, $B_1 = 2.29$ T and $B_2 = 2.87$ T at 75 GHz, and $B_1 = 3$ T and $B_2 = 3.62$ T at 95 GHz. The maximum susceptibility of the resonant peak at 35 GHz is $\chi'' = 29474$, at 55 GHz is $\chi'' = 20669$, at 75 GHz is $\chi'' = 15150$ and at 95 GHz is $\chi'' = 11774$. Figure 4.10(b) presents the spatial distribution of magnetisation oscillation amplitude for different peaks at 55 GHz at 0.3 T, 1.6 T, 1.8 T and 2.3 T that corresponding to the green circles at Figure 4.10(a). Experimentally, the corresponding peak positions are observed by photovoltage spectroscopy occurred at $B_1 = 1.87$ T and $B_2 = 2.25$ T at 55 GHz, $B_1 = 2.34$ T and $B_2 = 2.95$ T at 75 GHz, and $B_1 = 3.1$ T and $B_2 = 3.7$ T at 95 GHz (Figure 4.11). The experimental observations display a series of small resonances (1-5) associated with quantised dipolar edge spin-wave modes including bonding-antibonding peaks. In most cases, the general solution of the $B = \hbar\omega/g\mu_B$ equation gives the right position of the peak at the bulk mode, but when we have the localised mode, this equation will explain the position of the main peak and the shifting of resonances. The resonances shift linearly with increasing frequency, Figures 4.10 and 4.11. There are additional experimental resonances not explained theoretically, which most likely arise from 3D volume spin waves not accounted for by OOMMF magnetic stimulation and are indicated by blue arrows, Figures 4.11. The narrowness of the dips and their occurrence below the ferromagnetic resonance is suggestive of localised spin waves, as shown in detail in Section 2.7.2.2.

The results obtained by the OOMMF simulation are in qualitative agreement with the experimental results for the predicted positions of resonance, Figures 4.10 and 4.11. These suggest the formation of bonding–antibonding pairs of edge spin waves. One difficulty in indexing these peaks is that the experimental resonances are shifted by the higher magnetic field, possibly due to the magnetocrystalline anisotropy of Co. This shift is $H_c = 2K_u/M_S\mu_0 = 0.26$ T at 55 GHz, 0.05 T at 75 GHz, 0.1 T at 95 GHz, and the average of the shifting is around +0.13 T. For example, accounting for this +0.26 T shift from theoretical to experimental one is able to relate the position of the bonding and antibonding resonances I and II as we have now indicated in Figures 4.10 and 4.11.

Figure 4.11 shows that the amplitude of the resonant peak is 1.6 μV at 55 GHz, 0.2 μV at 75 GHz and 0.04 μV at 95 GHz. The positions of peaks I and II from the OOMMF simulation match the peaks observed with photovoltage spectroscopy. The position of the main peak can be calculated using Equation 2.22. In addition, the amplitude of the resonant peaks in both theory (micromagnetic simulations) and experiment (photovoltage spectroscopy) decreases with increasing frequency, which is in close agreement with the theory interpreted in Section 3.3 and the results presented in Figures 4.10 and 4.11.

However, in practice, Figure 4.10 does not show the microwave heating effect seen in experiments. Microwave heating can increase the photovoltage background. Thus, there is a mismatch between the background signal of the simulation, which can be greater than the photovoltage signal in Figure 4.11. Consequently, there is rectification by Ohmic contacts in the sample which adds a background photovoltage and causes differences in the actual values of the signal in Figure 4.11 as described in Section 3.1.1.

Figure 4.12 displays the photovoltage of the Co stripe at microwave frequencies ranging between 36 GHz and 83 GHz at -20 dBm. The results were obtained at -10 dBm (Figure 4.11), both at a temperature of 1.3 K. It also shows a broadening of the ferromagnetic resonance band, which hosts a complex series of subsidiary resonances. We observe that the resonances shift linearly with frequency and the dotted line shows that the distance between the peaks becomes larger with increasing frequency (see Figure 4.12). This indicates that dipolar interactions are more effective in stabilising the magnetisation perpendicular to the stripes. Accordingly, the onset of the end of the ferromagnetic resonance is plotted to provide a precise comparison between experiment and simulation. Figure 4.13 indicates the ferromagnetic onset (red circles) and cut-off (blue circles) that demonstrate how the width of the ferromagnetic resonances increases from 0.94 T at 36 GHz to 2.77 T at 83 GHz. Figure 4.14 details the 50 GHz curves at the resonances with dipolar edge spin-wave modes and their dependence on the microwave powers -15 dBm, -20 dBm, and -30 dBm taken at a temperature of 1.3 K and when B_{dc} is perpendicular to the Co stripe. The resonances with dipolar edge spin waves modes according to the microwave powers shows an equal bandwidth which is

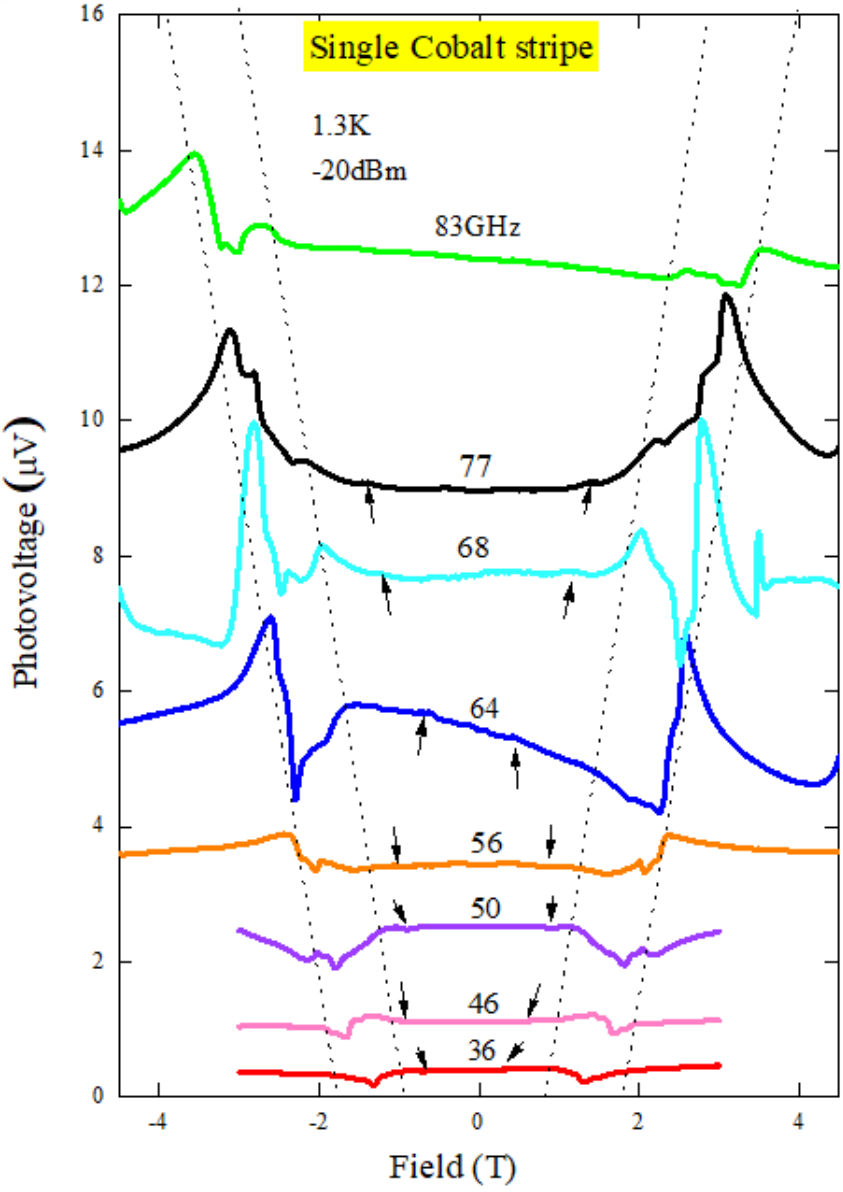

Figure 4.12 Photovoltage spectroscopy of magnetic excitation as a function of magnetic field strength B_{dc} and microwave frequency, taken at a temperature of 1.3 K the microwave power was applied is -20 dBm. The dotted line marks the guide to the eye for the magnetic field dependence of the onset and the cutoff of the bulk ferromagnetic resonance. At lower magnetic field, the arrows indicate a series of smaller dips induced by microwaves.

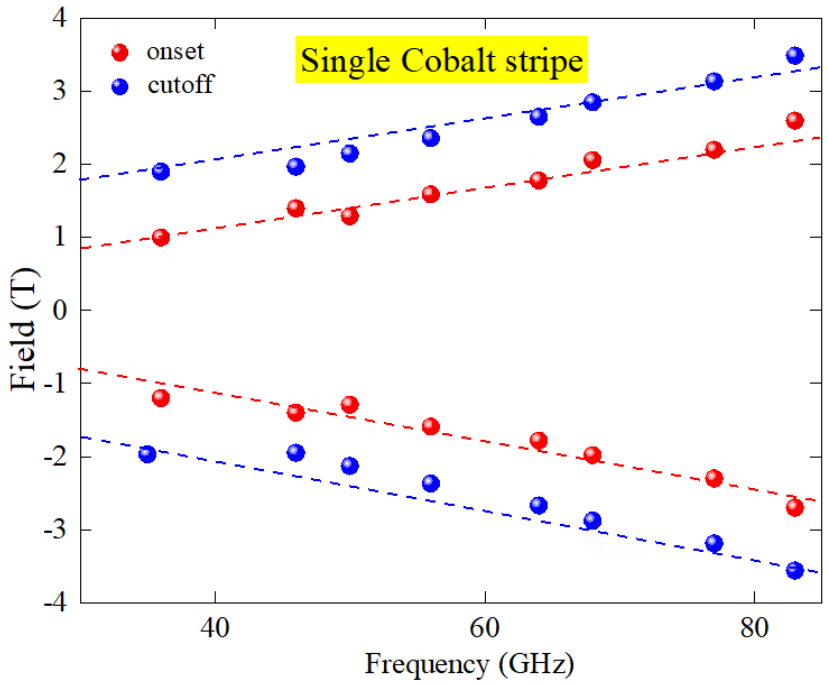

Figure 4.13 The fan diagram of frequency dependence of the microwave resonances in the photovoltage of Co stripe under 1.3 K temperature for the data of Figure 4.13.

about 0.23 T but the amplitude of the resonances proportional with the power as Equation 3.11.

However, on further analyses, the magnetic resonance spectra of the Co stripes were calculated using OOMMF and were compared when B_{dc} is along the short and long axes at 4 K with power (-10 dBm) as shown in Figure 4.15. Shown in the same figure is the difference between the amplitude of the magnetic resonance at 41 GHz with B_{dc} in perpendicular and parallel orientations to the Co stripe. The maximum susceptibility of the resonant peak at 41 GHz with the perpendicular orientation is about $\chi^{''} = 22546$ while in the parallel orientation, the amplitude of resonance is approximately $\chi^{''} = 26$. The peak at perpendicular orientation is 586 times larger than the peak in parallel orientation which is very weak theoretically, Figure 4.15. Nevertheless, the locations of ferromagnetic resonance in the micromagnetic simulation are the following: $B_1 = 1.14$ T (I) and $B_2 = 1.69$ T (II) at 41 GHz in the perpendicular orientation, while in the parallel orientation are the following: $B_1 = 0.287$ T (I) $B_2 = 0.97$ T (II) and $B_3 = 2.6$ T (III) at 41

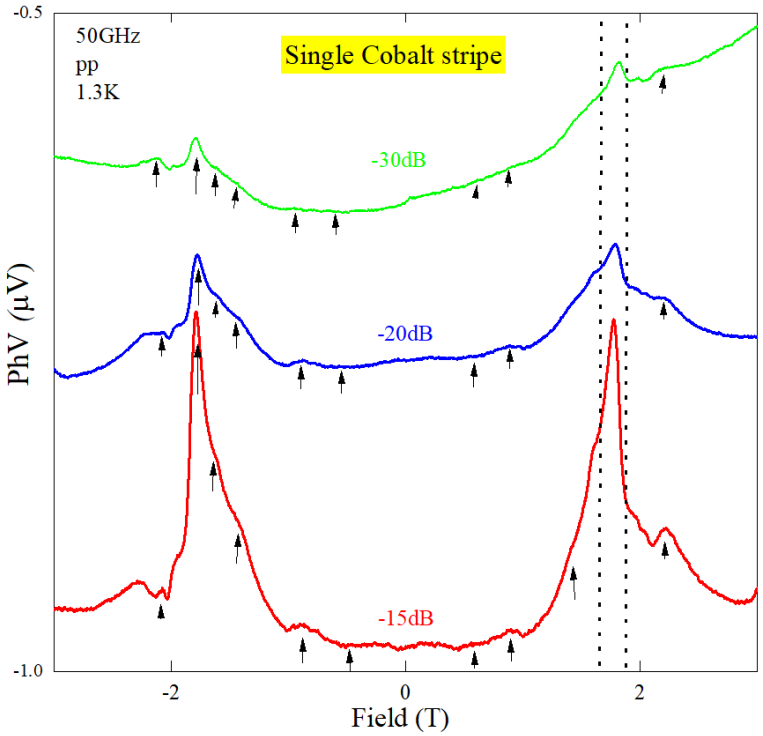

Figure 4.14 The 50 GHz curves which shows the resonances with dipolar edge spin waves modes according to the microwave powers for the Co stripe and at B_{dc} perpendicular to the long axis. The arrows indicate resonances with quantised DESW modes in singal Cobalt stripe. The bandwidth of the resonance is delimited by the dash-dotted lines.

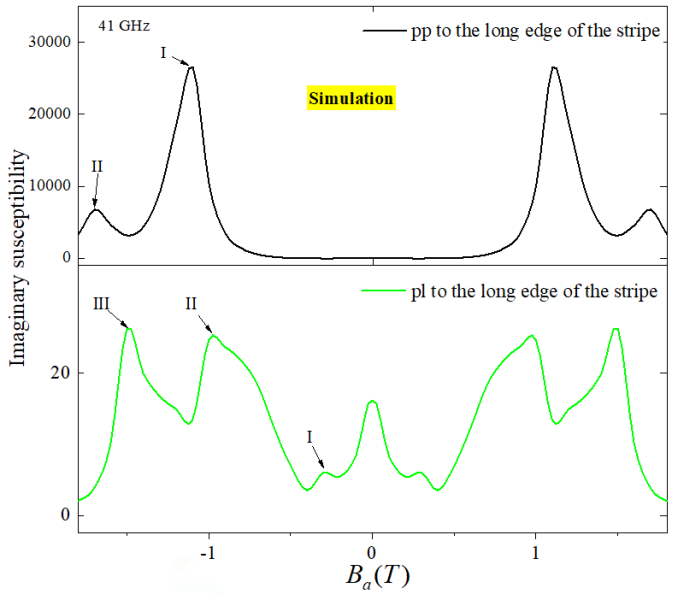

Figure 4.15 The comparison of magnetic resonance spectra of individual magnets between when B_{dc} is parallel or perpendicular to the magnetic stripe using OOMMF micromagnetic simulation.

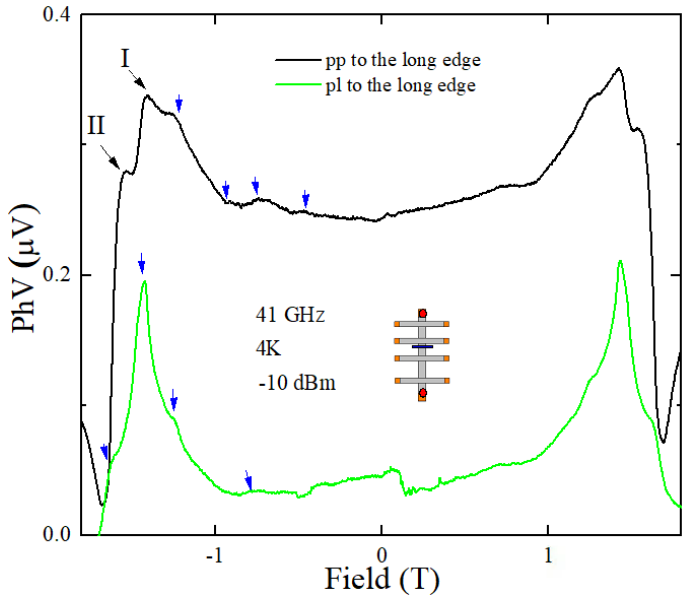

Figure 4.16 The experimental comparison of magnetic resonance spectra of individual Co stripe probed by photovoltage spectroscopy. The distances between the curves were adjusted using the y-offset. The photovoltage is measured across voltage probes 8 μm apart, when B_{dc} parallel and perpendicular to the long edge of the Co stripe. The measurements were taken under T = 4 K and -10 dBm power. The arrows point to a discrete structure of localised spin excitations.

GHz. Additionally, photovoltage peaks always occurred at higher magnetic fields than was expected from theory.

In contrast, Figure 4.16 shows the experimental distinction of magnetic resonance spectra of a cobalt magnetic stripe at 41 GHz in parallel and perpendicular d.c. magnetic field at the long edge of the stripe at 4 K. The hybrid devices with the Hall probes used to detect Photovoltage which was measured using lock-in detection at the modulation frequency of the microwave power (830 Hz). The magnetic stripe creates a peak of about 0.31 μV when magnetised perpendicular and 0.19 μV when parallel to the Co stripe. The peak at perpendicular orientation is 1.63 times larger than the peak in parallel orientation experimentally, Figure 4.16. Moreover, the peak position at perpendicular orientation are about $B_1 =$ 1.37 T (I) and $B_2 = 1.55$ T (II) at 41 GHz. Consequently, the series of resonances calculated using OOMMF matches the magnetic fields corresponding to the peak positions observed by photovoltage spectroscopy. It can be concluded that the amplitude when B_{dc} perpendicular is greater than when B_{dc} parallel to the long edge, Figures 4.15 and 4.16. These measurements show the localisation of edge spin waves in B_{dc} perpendicular is stronger than that in the Damon–Eshbach mode when B_{dc} parallel to the Co stripe. Also, the influence of temperature on the resonant peaks at 4 K which is very similar to the results at 1.3 K, as summarised in Figures 4.10 and 4.11.

4.1.4 The effect of Magnetocrystalline Anisotropy on the Ferromagnetic Resonance

The magnetic anisotropy of ferromagnetic materials plays a dominant role in the magnetisation curves and ferromagnetic resonance spectra, and in the position of the measured spectra. The hexagonal cobalt lattice structure implies that the easy axis is perpendicular to the plane. The anisotropy is determined by the field required to tilt the magnetisation from the easy to the hard axis, with the easy axis indicated by the vector (x, y, z). The effect of magnetocrystalline anisotropy on ferromagnetic resonance is more complex as precession causes the magnetisation vector to probe a 3D volume before settling in its new steady state. The dipolar easy axis is the long axis of the micromagnet. In our Co micromagnetic stripes,

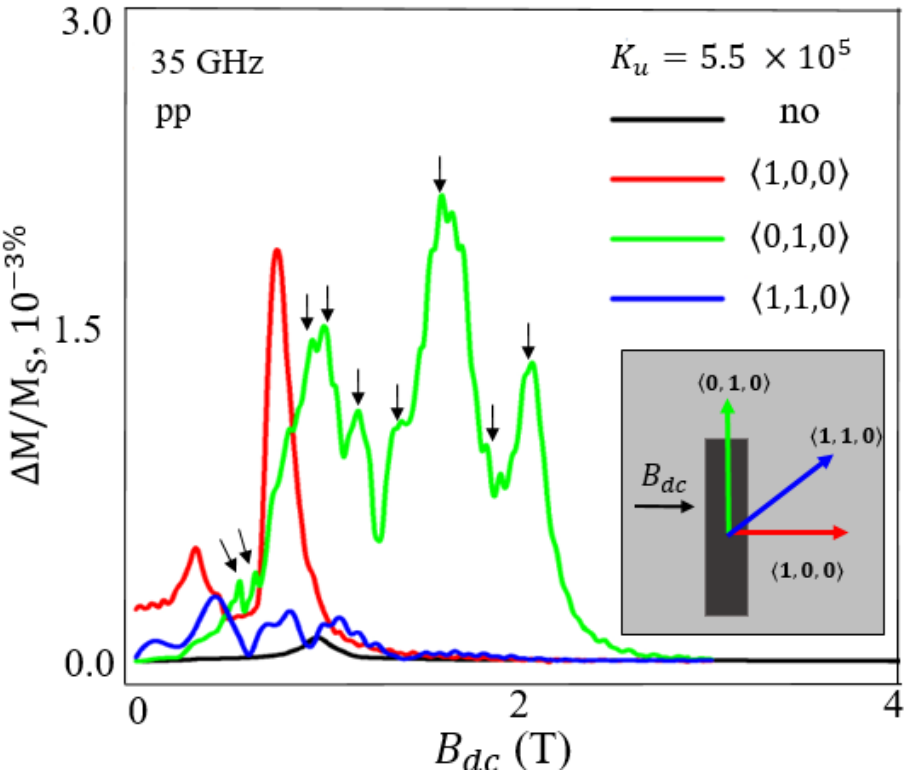

Figure 4.17 Ferromagnetic resonance calculated at 35 GHz for different orientations of the magnetocrystalline anisotropy ⟨100⟩, ⟨010⟩, and ⟨110⟩. The resonance splits into multiple resonances owing to the finite size of the stripe. As the easy axis tilts progressively along the long axis the resonance moves to higher B_{dc}. The inset shows a schematic view of the orientations of the magnetocrystalline anisotropy in the Co polycrystalline and B_{dc} is along the short axis of the stripe.

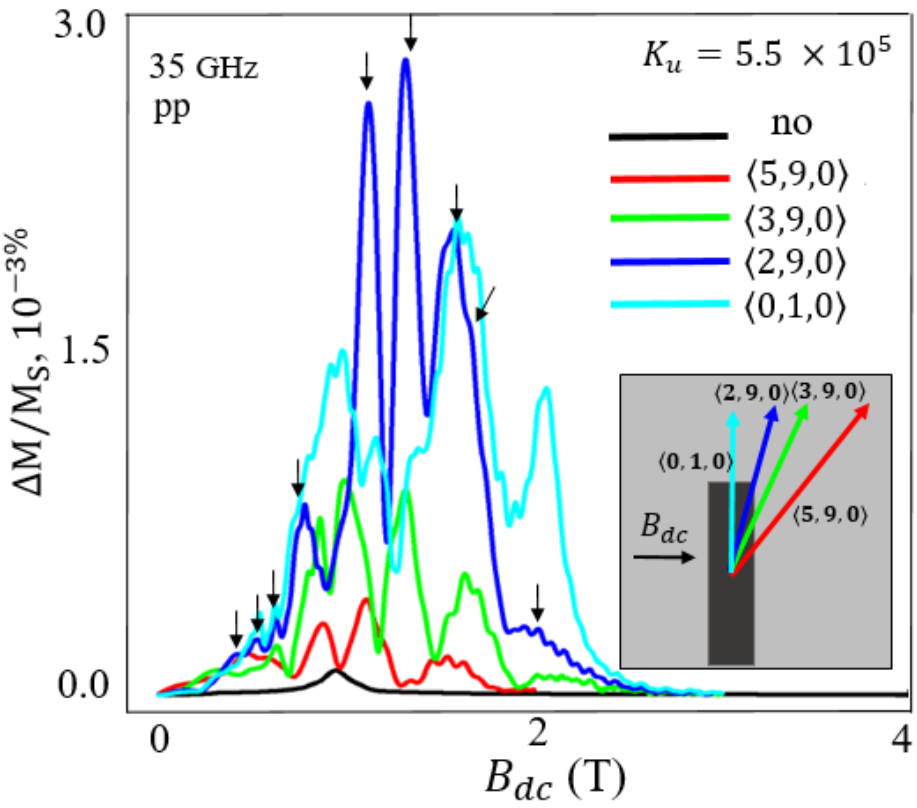

Figure 4.18 Ferromagnetic resonance calculated at 35 GHz for different orientations of the magnetocrystalline anisotropy ⟨590⟩, ⟨390⟩, ⟨290⟩, and ⟨010⟩. The resonance splits into multiple resonances owing to the finite size of the stripe. As the easy axis tilts progressively along the long axis the resonance moves to higher B_{dc}. The inset shows a schematic view of the orientations of the magnetocrystalline anisotropy in the Co polycrystalline and B_{dc} is along the short axis of the stripe.

the easy dipolar axis is along the longest edge in a polycrystalline Co film the resonance is shifted to higher for all orientations of B_{dc}. The anisotropy field can be expressed by: $\Delta H = 2K_u/M_S\mu_0$, where $2K_u$ is the constant anisotropy of Co and is $5.5 \times 10^5 J/m^3$, at low-temperature [116].

We calculated the micromagnetic simulation using OOMMF by applying a small ac magnetic field to the polycrystalline Co which is on the top of the semiconductor, and considered the magnetocrystalline anisotropy field which is perpendicular to the Co stripe. B_{dc} is therefore along the short axis of the strip. Changes in the magnetisation were then recorded. Figure 4.17 identifies the position of the ferromagnetic resonance at 35 GHz for the different orientations of magnetocrystalline anisotropy: $\langle 100 \rangle$, $\langle 010 \rangle$, $\langle 110 \rangle$. As shown in Figure 4.17, the resonance splits into multiple resonances owing to the finite size of the stripe. As the easy axis tilts progressively along the long axis the resonance moves to another B_{dc} position. Figure 4.18 shows the ferromagnetic resonance (also at 35 GHz) for various directions of magnetocrystalline anisotropy ($\langle 590 \rangle$, $\langle 390 \rangle$, $\langle 290 \rangle$, and $\langle 010 \rangle$). Different peaks appear because the resonances shift to a new position as the easy axis tilts gradually along the long axis.

4.2 Discussion

We explained the results on the discrete structure of spin-wave resonance as a function of the shape of the magnets, the magnetic field orientation (parallel or perpendicular to the magnetisation), the magnetocrystalline anisotropy and the geometry of the approximately 80 nm wide nanomagnets. When the magnetic field is parallel, a series of resonances determined using the OOMMF calculation of imaginary susceptibility χ'' matched the position of magnetic fields observed by photovoltage spectroscopy that correspond to the peak positions for each frequency (Figures 4.8 and 4.9). The relative peak amplitudes when the magnetisation is parallel to the long axis of the stripe indicate that Damon-Eshbach modes are much weaker than dipolar edge spin wave modes when B_{dc} is perpendicular to the long axis. The relative peak amplitudes when the magnetisation is parallel to the long axis of the stripe indicate the Damon-Eshbach modes. There are also small additional peaks with a vanishing magnetic field and the amplitude of the

resonant peaks decreases with increasing frequency, both theoretically and experimentally (Figures 4.8 and 4.9). The experiment cannot confirm whether there is a peak at zero, as predicted theoretically.

For the perpendicular field orientation case, interpretation is more straightforward because the formed magnetostatic potential confines spin waves in bonding-antibonding peaks, as shown in Figure 4.10(a). The peak positions observed by OOMMF simulation and experiment match (Figures 4.10 and 4.11). The amplitude of the resonant peaks in the micromagnetic simulation and photovoltage spectroscopy decrease with increasing frequency as well, and no peaks exist at zero frequency in the simulation (Figure 4.10). The decreases of resonances with increasing frequency are unavoidable irrespective of the temperature or orientation of the magnetic field. The simulation differs from the experimental structure below the main resonance and, practically, there is a mismatch in the amplitude of resonance between the simulation which is much higher compared with the structure observed by photovoltage (Figures 4.8, 4.9, 4.10 and 4.11). The resonance amplitude of the Damon-Eshbach (DE) mode is considerably weaker than that of the dipolar edge spin waves (DESWs) mode when B_{dc} is perpendicular to the long axis. The susceptibility resonances when B_{dc} is perpendicular are better defined than when B_{dc} is parallel to the Co stripe. On the other hand, the amplitude of the experimental ferromagnetic resonance attenuates faster as the microwave frequency increases when B_{dc} is perpendicular, rather than parallel, to the magnetic stripe.

The results obtained at 4 K (shown in Figures 4.15 and 4.16) confirm that the localisation of edge spin waves is stronger than the DE mode when B_{dc} is perpendicular, as observed at 1.3 K (Figures 4.10 and 4.11). However, the influence of the magnetocrystalline anisotropy of Co splits into multiple resonances owing to the finite size of the stripe and shifts to a new position with higher amplitude than with no applied the anisotropy field. There are no experimental measurements for the magnetocrystalline anisotropy effect as there exist only its calculation via OOMMF simulation. It is difficult to model true polycrystalline anisotropy and that Figures 4.17 and 4.18 are a limiting case where uniaxial anisotropy is assumed in crystal.

Chapter 5

Ferromagnetic Resonance of the Magnetic Disk

The previous chapter compared the results from micromagnetic simulations and experimental measurements when B_{dc} propagate along the short edge and the long edge of the magnetic stripe at varying frequencies. In this chapter, we demonstrate the properties of a magnetic disk at varying frequencies in order to find the resonance peak as a function of the microwave frequency, with the measurements performed at 4 K. The magnetic disks are therefore well suited to studying photovoltage spectroscopy as a part of this thesis. The modulation magnetic field was generated by an 80 nm diameter Co disk. There is no distinction between the parallel orientation and the perpendicular magnetic field for symmetry reasons. This disk is magnetised the in-plane, parallel to the 2DEG. In this case, a 2D potential is created at opposite ends of the magnetised disk. A bonding state is located at the centre of the disk, and the antibonding states occur at the sites of the two magnetic wells on the edges. The ferromagnetic resonances of the magnetic disk is similar to the case when the stripes are magnetised along their short axis [117]. The photovoltage spectra calculation will be explained as a part of this chapter which shows the shape of the resonance (Lorentzian shape).

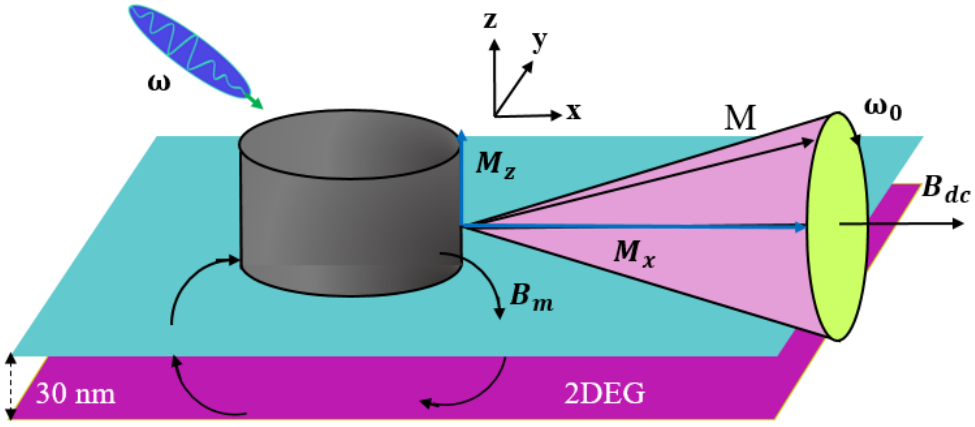

Figure 5.1 Schematic of the magnetic Co dot magnetised in the plane of the 2DEG by B_{dc} and driven to resonance by B_{ac}. Magnetic moments M undergo precession at frequency ω_0 in magnetic field B_{dc} under 4 K temperature.

5.1 Results

The photovoltage measured on the disks will show multiple steps involving the discrete structure of spin-wave resonance as a function of the shape of Co ferromagnets. The photovoltage spectra will also be modelled using OOMMF simulation. The positions and amplitudes of the experimental spin-wave resonances will be compared with the micromagnetic simulation of the spectra. We will also describe the numerical calculation of the photovoltage for different magnetic fields using MatLAB to solve Equation 4.5.

Figure 5.1 illustrates a schematic of the Co dot magnetised in the plane of the 2DEG by B_{dc} and driven on resonance by B_{ac}. We manufactured a 30 nm deep $GaAs/Al_{0.33}Ga_{0.67}As$ heterojunction to minimize the decay of the stray magnetic field B_m from Co micromagnets fabricated at the surface. A homogenous magnetic field B_{dc} was applied to induce precession of magnetic moments, M. The microwaves, moreover, was applied at frequency $\hbar\omega$ to the Co disk, which was linearly polarized with an electric field and the magnetic field. The B_{ac} field will drive the precession of the magnetisation, M, at a frequency ω_0, as seen in Figure 5.1. The M_x and M_z components produce the time-dependent magnetic modulation $B_m(x,t)$. The magnetic modulation produces an eddy current contribution. The M_x and M_z components induce an oscillating (e.m.f.) in the 2DEG. This e.m.f. oscillates at high frequency giving high-frequency photocurrent. The aver-

age voltage induced by these currents doesn't vanish however due to rectification by the Hall effect. The rectification mechanism is explained by considering Ohm's law:

$$J = \sigma E + \mu(B_\perp) J \times B \tag{5.1}$$

where J is the current in the 2DEG, σ is the conductivity, E is the electric field, $B_\perp$ is the magnetic field perpendicular to the 2DEG and $\mu = 1.5 \times 10^6 cm^2 V^{-1} s^{-1}$ in the electron mobility of the $GaAs/AlGaAs$ heterojunction at B = 0. The principle of the rectification is based on the there is B_{ac} which drives the spin resonance. The oscillations of the magnetization induce a Faraday electric field which drives a.c. currents in the 2DEG. These currents result from oscillations of the magnetization which induce an a.c. fringe field $B_\perp$ at the 2DEG. This field will couple with the electric field driving eddy currents to produce a d.c. rectified photovoltage across the stripe. At resonance, $\omega = \omega_0$, the magnetisation oscillates between being parallel and antiparallel to B_{dc}, giving photovoltage peaks in accordance with Equation 4.5.

5.1.1 Photovoltage Measurement at Low-temperature

We now come back to the measured results for the disk, which are similar to the case of magnetic stripes when the stripes are magnetised along their short axis. These results show the difference in the positions of peaks and the amplitude of the resonant peaks, both theoretical and experimental, as a function of frequency, at 4 K, Figures 5.2 and 5.3.

The micromagnetic simulation was obtained by applying a small magnetic field to record the magnetisation and define the power absorption of micromagnetic materials, as described in Section 3.3. The bonding state occurs at a lower magnetic field, whereas the other is the antibonding state. These states are indicated by arrows (I) and (II), respectively, in Figure 5.2. The resonances in the micromagnetic simulation occur at $B_1 = 1.01$ T and $B_2 = 1.25$ T in the 35 GHz range. At 55 GHz, the locations of the resonances in the micromagnetic simulation are $B_1 = 1.71$ T and $B_2 = 1.95$ T, while at 75 GHz the resonances are at $B_1 = 2.42$ T and $B_2 = 2.72$ T, as shown in Figure 5.2. Figure 5.2(b) depicts the spatial

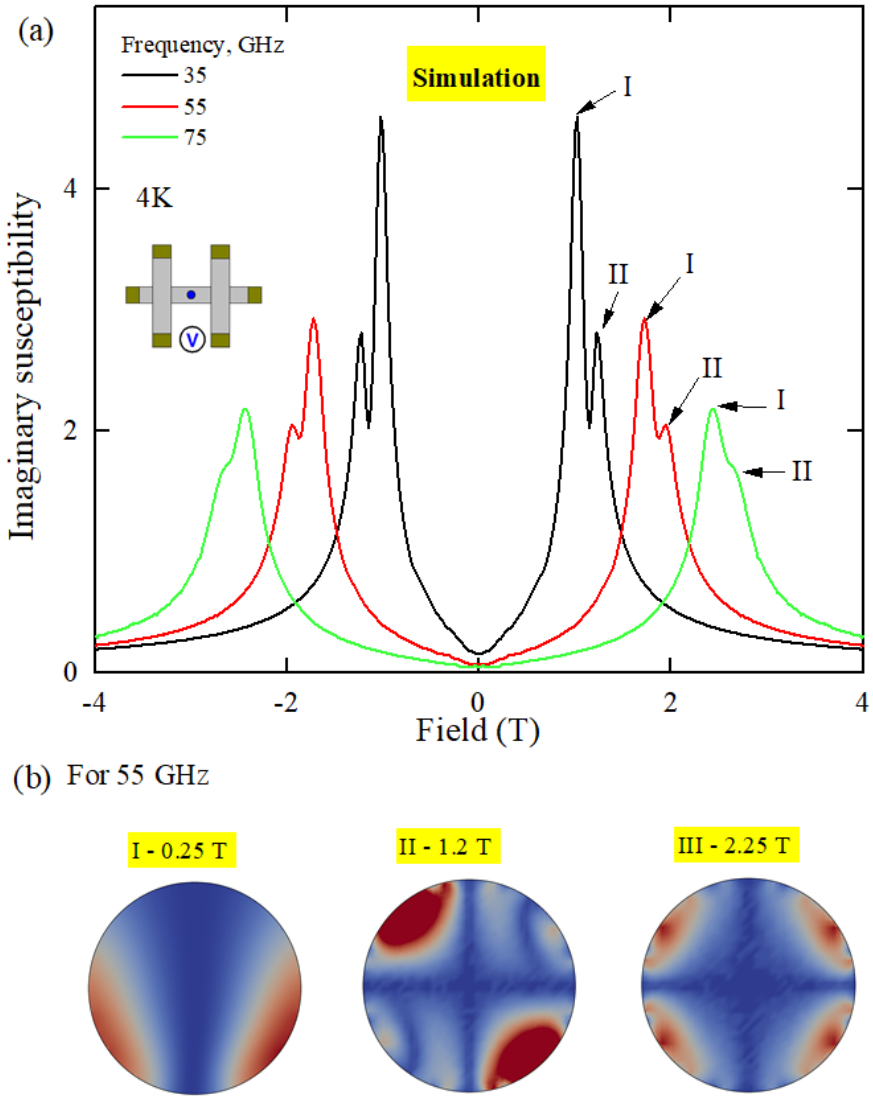

Figure 5.2 Disk. (a) Dependences of the amplitude of magnetisation oscillation on the value of magnetising field for different frequencies 35 GHz5, 55 GHz, and 75 GHz. (c) Spatial distribution of magnetisation oscillation amplitude for different resonance picks at 55 GHz.

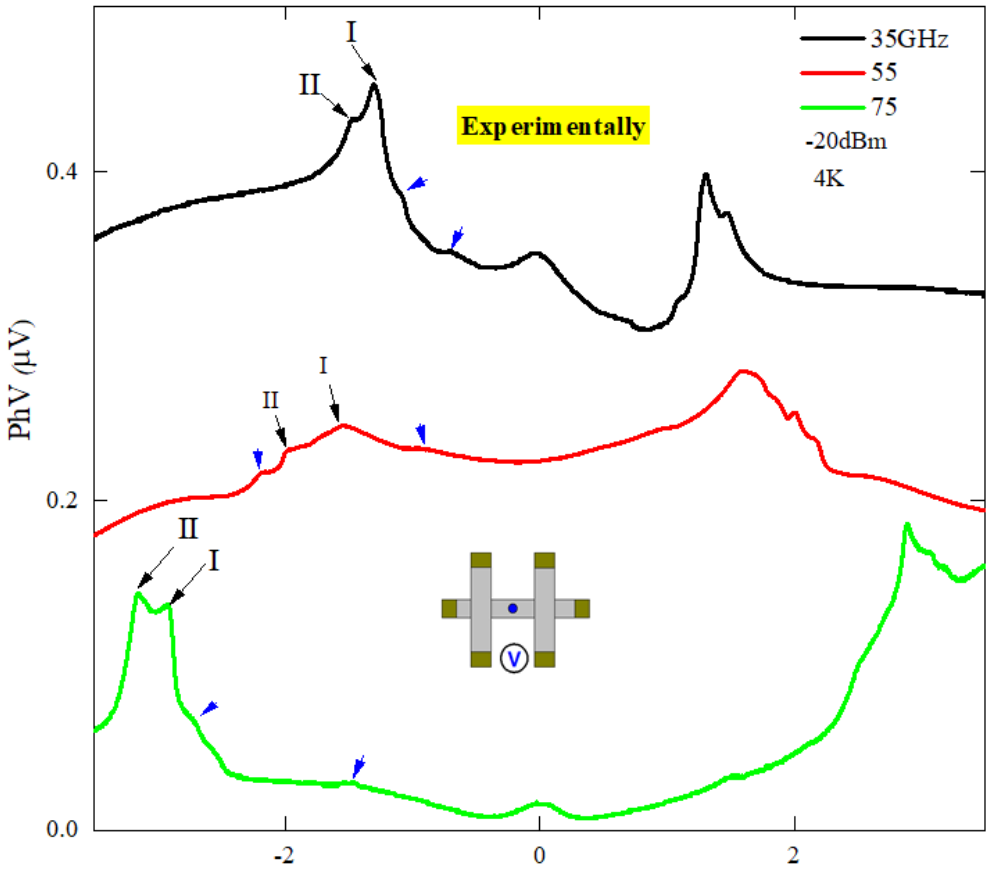

Figure 5.3 Experimental dependence of the photovoltage spectroscopy of magnetic excitation was magnetised in-plane parallel to the 2DEG at different frequencies 35 GHz, 55 GHz, and 75 GHz. The microwave power was 6 dBm. The bonding states are the main peaks that occur at the low magnetic field whereas the antibonding states are the minor peak, as indicated by the arrows labelled I and II, respectively. The amplitude of the resonance decreases with increasing frequency. T = 4 K. Curves are vertically offset for clarity.

distribution of the magnetisation oscillation amplitude for different peaks at 55 GHz and magnetic fields of 0.25 T, 1.2 T, and 2.25 T. In contrast, the positions of the ferromagnetic resonances in the experimental photovoltage spectrum are B_1 = 1.3 T (I) and B_2 = 1.48 T (II) at 35 GHz. At 55 GHz the resonances occur at B_1 = 1.58 T (I) and B_2 = 2.02 T (II), and at 75 GHz they appear at B_1 = 2.9 T (I) and B_2 = 3.17 T (II), as seen in Figure 5.3. Several additional peaks occur in the experiment (blue arrows) that are not predicted by theory.

The location of the peaks at different frequencies can be calculated using Equation 2.22, which describes the magnetic field and the precise location of the main peak. For example, at 35 GHz the calculated magnetic field is 1.16 T, which corresponds closely to the main peak in the micromagnetic simulation at 1.01 T and to the photovoltage resonance, which is around 1.3 T. Similarly, at 55 GHz, the calculated magnetic field is 1.83 T, the peak in the OOMMF simulation is around 1.71 T, while the photovoltage spectroscopy gives a peak at 1.58 T. At 75 GHz, the calculation of the magnetic field gives nearly 2.5 T and the OOMMF simulation peak is around 2.42 T and the photovoltage peak is located at 2.9 T. This demonstrates general agreement between experiment and theory in the predicted resonance positions, indicating the formation of bonding-antibonding pairs of edge spin waves. However, the precise positions of the peaks differ between theory and experiment. The experimental resonances are shifted to a higher magnetic field by the magnetocrystalline anisotropy of Co. The resonance shift at low temperature becomes H_c = 0.27 T at 35 GHz, 0.13 T at 55 GHz, 0.48 T at 75 GHz and the average of shifting is about 0.29 T, as observed. However, the agreement between the experiment and theory is about 75.6%. A significant discrepancy between experiment and theory is found at 75 GHz, while at lower frequencies, there is little difference. The reason for this is that the peak is very sharp at low frequencies, while at high frequencies the peak becomes broader making it difficult to accurately identify it when there are many other minor resonances. The shifting suggests that there is a preferential alignment of the easy axis, If there is no shift, that means the field is parallel to the easy axis (C axis). But, if there is a shift, that suggests that the B_{dc} is perpendicular to the easy axis for the Co grows at $GaAs$. In the case of the magnetic stripe, at B_{dc} parallel to the long axis, the shift is about 0.5 T, but at B_{dc} perpendicular to the long axis, the component of the field is much smaller about 0.13 T. At the case

of the magnetic disk, the average of shifting is about 0.29 T, which makes sense, as it is the average of the shifting in magnetic stripe for 0.5 T and 0.13.

Figure 5.2(a) shows the susceptibility amplitude of the bonding state, which is $\chi^{''}$ = 2.55 at 35 GHz. The susceptibility amplitudes of the main resonances are $\chi^{''}$ = 1.08 and $\chi^{''}$ = 0.46 at 55 GHz and 75 GHz, respectively. Likewise, experimentally, at 35 GHz the peak amplitude is about 0.2 μV, while at 55 GHz it is around 0.015 μV and at 75 GHz it is approximately 0.013 μV (see Figure 5.3). In both cases, the peak amplitude decreases with increasing frequency, which completely matches the theory that was introduced in Section 3.3. The results are shown in Figures 5.2 and 5.3.

In Figure 5.4, the photovoltage spectroscopy of the magnetic excitations of the Co disk is repeated over a range of microwave frequencies between 35 GHz and 96 GHz. This measurement was recorded at 4 K with the microwave power changed to -6 dBm. The microwaves produce a range of discrete resonances at a lower magnetic field that indicated by the arrows, Figure 5.4. We observe that the resonances shift linearly with increasing frequency. Remarkably, no effect on the ferromagnetic band from the change of the microwave power can be observed. Where the broadening of the ferromagnetic resonance band increases significantly with increasing frequency in both -20 dBm and -6 dBm, Figures 4.12 and 5.4. The dotted line shows that the distance between the peaks becomes larger with increasing frequency. These experimental results allow a more accurate comparison with the theoretical predictions. Additionally, the onset (red circles) and the cutoff (blue circles) of the ferromagnetic resonance range are plotted in Figure 5.5. The onset and cutoff points of the magnetic field range are taken from the ferromagnetic resonance data in Figure 5.4. Furthermore, the width of the ferromagnetic resonances increases from 0.45 T at 35 GHz to 3.1 T at 96 GHz.

Figure 5.6 exhibits the resonances of the Co disk at 50 GHz and their dependence on the microwave power, which is set to 0 dBm and -6 dBm. These measurements were taken at 4 K. The bandwidth of the main resonances is the same for both power levels, which is approximately 0.152 T. On the other hand, the amplitude of the resonances decreases from about 0.02 μV at 0 dBm to around 0.005 μV at -6 dBm. Experimentally, the amplitude of the resonances is proportional to

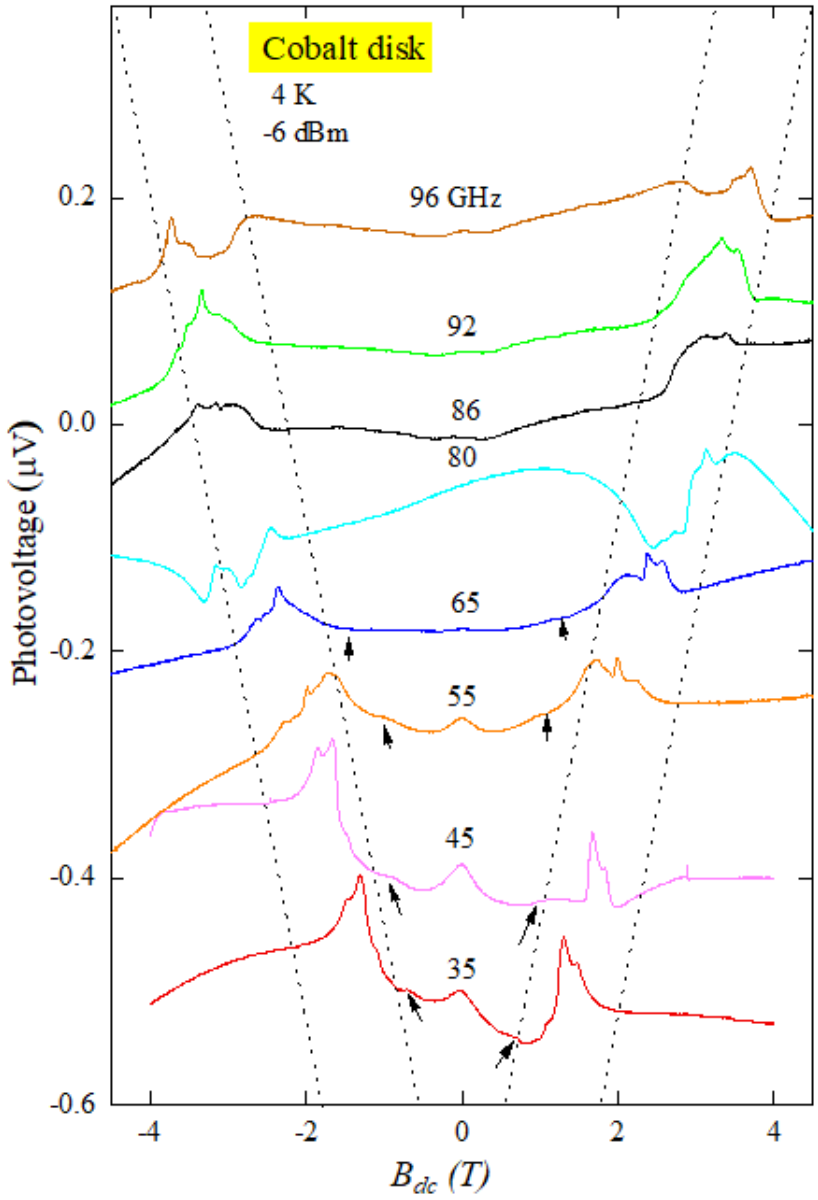

Figure 5.4 Photovoltage spectroscopy of magnetic excitation as a function of magnetic field strength B_{dc} and microwave frequency, taken at a temperature of 4 K the microwave power was applied is -6 dBm. The dotted line marks the guide to the eye for the magnetic field dependence of the onset and the cutoff of the bulk ferromagnetic resonance. These arrows at the lower magnetic field indicated a series of small dips that induced by microwave frequencies.

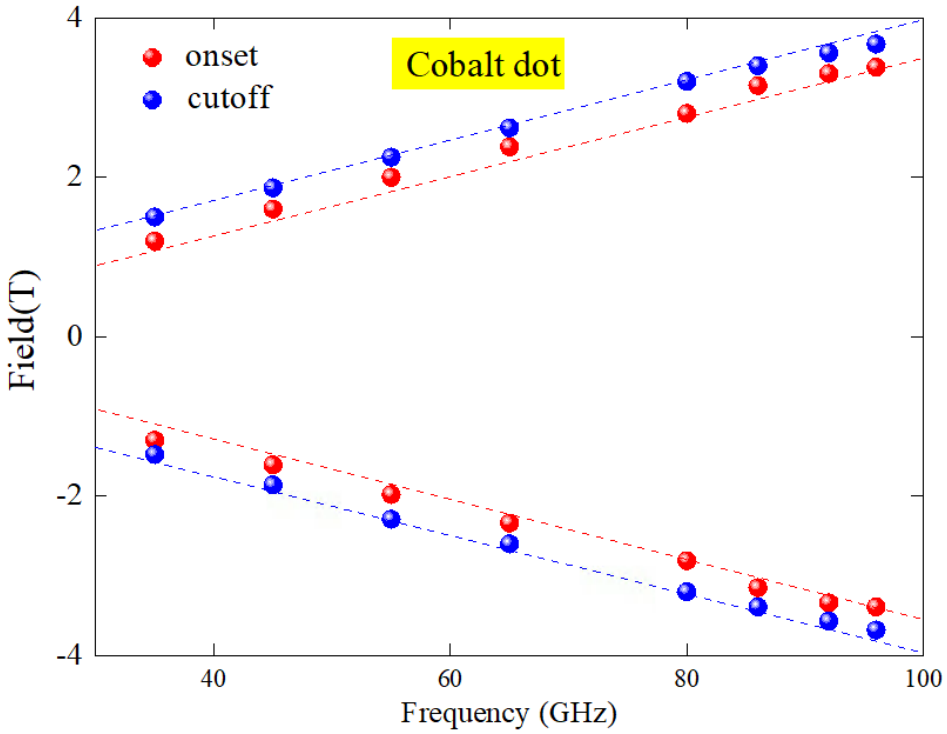

Figure 5.5 The fan diagram of frequency dependence of the microwave resonances in the photovoltage of Co disk under 4 K temperature for the data of Figure 5.4

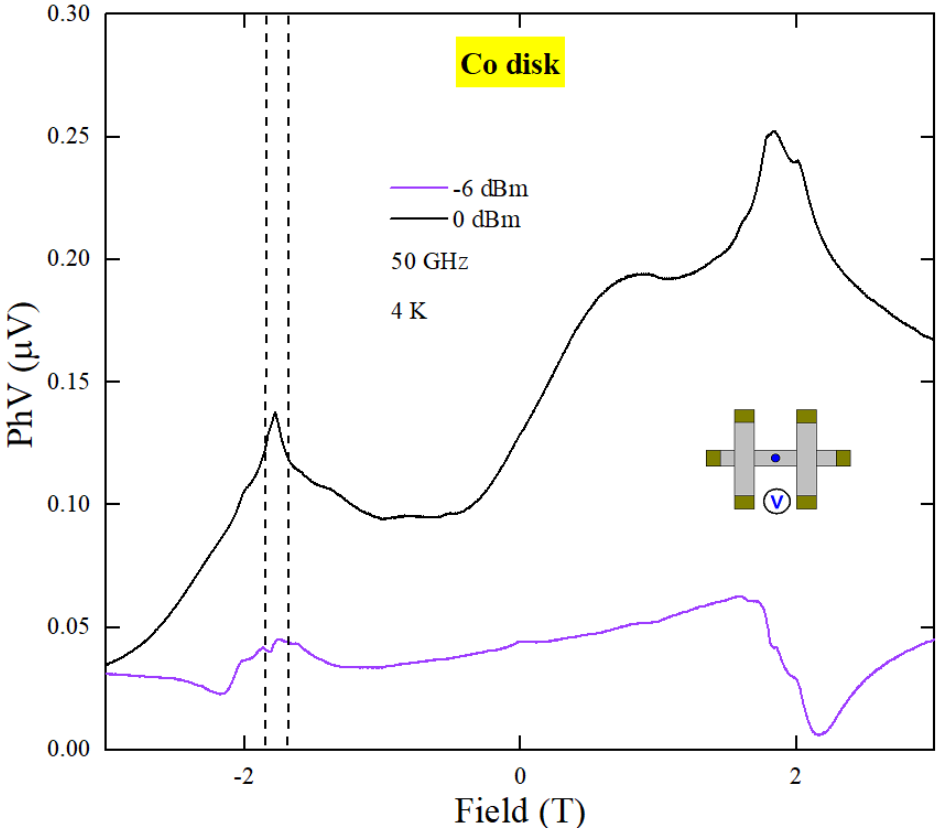

Figure 5.6 The 50 GHz curves which shows the resonances with dipolar edge spin waves modes according to the microwave powers for the Co disk. The bandwidth of the resonance is delimited by the dash-dotted lines.

the microwave power, which is in agreement with the theoretical prediction as described in Equation 3.11 and Figure 3.9.

5.2 Spectra Calculation

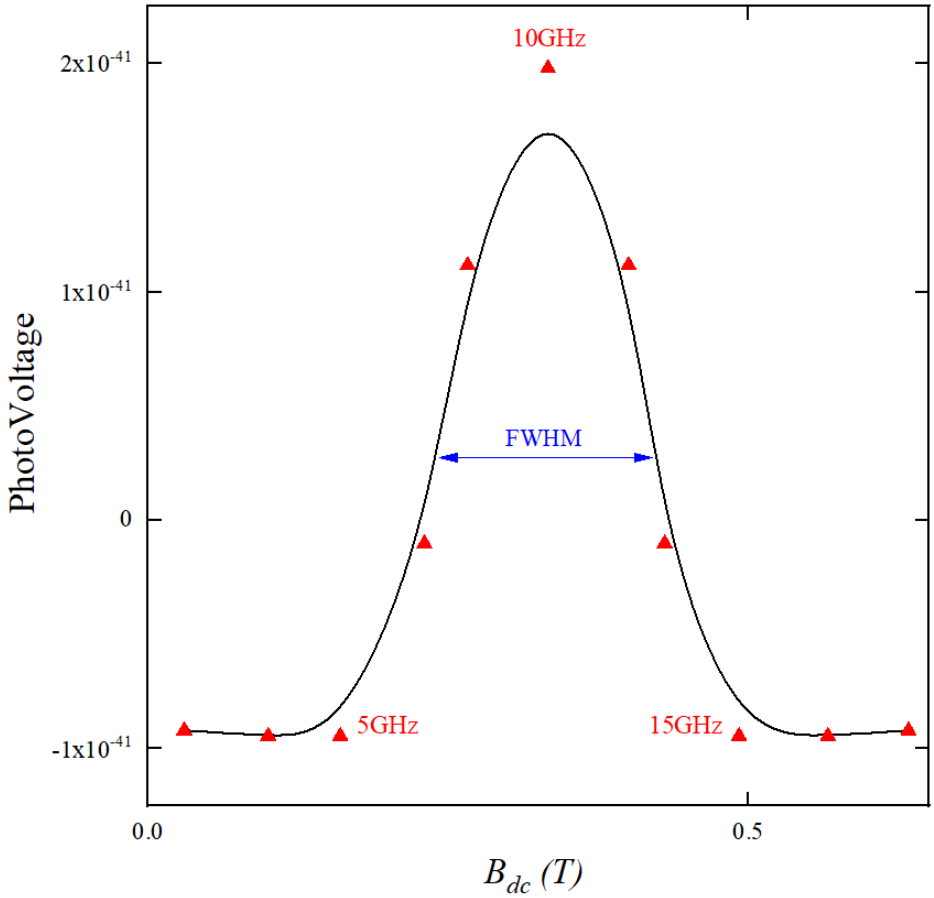

Figure 5.7 The calculation of photovoltage spectra obtained for different frequencies using OOMMF simulation which used to calculate the magnetisation M_x and M_z. The magnetisation M_x is rotating but not flipping. At the same time the magnetisation M_z oscillates and flips by 180 degrees. MatLAB is used to calculate the derivatives as a function of time, $\dot{M}_x$ and $\dot{M}_z$, in order to obtain the average $\langle M_z\dot{M}_x - M_x\dot{M}_z\rangle$. Multiplying the average by $\mu_0\mu^2 A$ to calculate the photovoltage using Equation 5.3. Several points have been calculated, at 1, 3, 5, 7, 8, 10, 12, 13, 15, 17, and 19 GHz, the maximum amplitude at 10 GHz.

The purpose of this section is to explain the calculation of the spectra by relating it to the results of the OOMMF simulation (imaginary susceptibility χ''). It also

shows that the photovoltage formula (4.5) yields a Lorentzian shape, which is the shape of the resonance.

Multiple steps must be taken to generate the calculation of the spectra. Firstly, use the OOMMF code to create the magnetisation in the x-direction (M_x) and the z-direction (M_z). The magnetic moment M_x is rotating but not flipping. At the same time the magnetisation M_z oscillates and flips by 180 degrees. MatLAB is used to calculate the derivatives as a function of time, $\dot{M}_x$ and $\dot{M}_z$, in order to obtain the average $\langle M_z\dot{M}_x - M_x\dot{M}_z\rangle$ [118, 119]. The photovoltage may then be calculated numerically by multiplying the average by $\mu_0\mu^2 S$, where μ is the electron mobility in the 2DEG, μ_0 is the magnetic permeability, and S is the effective area. Mathematically, the average can be written as follows:

$$\langle M_z\dot{M}_x - M_x\dot{M}_z\rangle = \frac{1}{T}\int_0^T (M_z\dot{M}_x - M_x\dot{M}_z)dt \tag{5.2}$$

The photovoltage formula, Equation 4.5, may then be rewritten in a time-dependent form:

$$PhV(t) = \mu_0\mu^2 S\frac{1}{T}\int_0^T (M_z\dot{M}_x - M_x\dot{M}_z)dt \tag{5.3}$$

where $T = 40\tau$ and τ is the period of the oscillation of M. Figure 5.7 shows the calculated resonance absorption. Several points have been calculated, at 1, 3, 5, 7, 8, 10, 12, 13, 15, 17, and 19 GHz, using Equation 5.3. At 10 GHz, the equation is satisfied, producing resonance which leads to maximum amplitude. Physically, when we have a magnetic element, there is an oscillation, but when there are two resonances, we obtain a very large and slow oscillation.

The response of an atom to the resonant absorption of electromagnetic radiation can be explained by the susceptibility which consists of two parts [120]. The real part, $\chi^{'}$, is a measure of the speed of an electromagnetic wave in a medium, and is related to the refractive index $n = c/v$. The imaginary part $\chi^{''}$ of the susceptibility corresponds to the absorption of energy. Therefore, the frequency dependence of the absorption $\chi^{''}$ has a Lorentzian shape and the width of the resonance is related to the damping parameter α. Often, the so-called full-width-

at-half-maximum (FWHM) is used to characterise the width of the peak. It depends solely on the strength of the Gilbert damping:

$$FWHM = \alpha\sqrt{3} \tag{5.4}$$

Hence, the damping coefficient, α, can be determined by the width of the resonance curve for any oscillator. The corresponding exponentially damped wave exhibits oscillations whose amplitude and frequency decrease within a decaying exponential envelope.

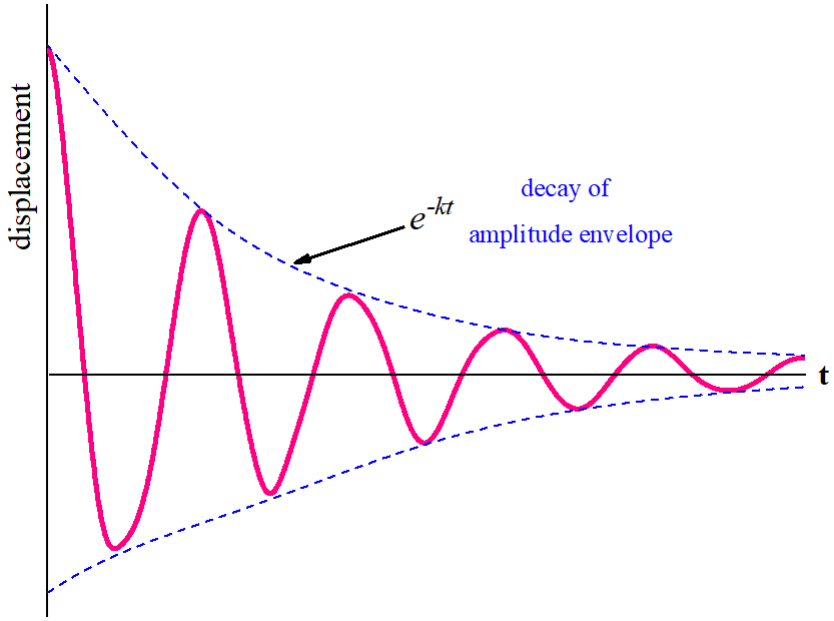

Figure 5.8 The damped oscillations. Notice that the curve is a cosine function inside an exponential envelope, e^{-kt}.

By analogy with the propagation of waves in the dielectrics, the frequency in the dielectric is $\omega = k(c/n)$, where c is the speed of light in vacuum. We use the electric susceptibility χ as an analogue of the magnetic susceptibility. The relative dielectric constant can be expressed as:

$$n^2 = \varepsilon_r = 1 + \chi \tag{5.5}$$

Additionally, if we examine the incident and transmitted portions of the wave, the wave may be written as e^{ikx}, which is:

$$e^{ikx} = e^{i(k^{'}+ik^{''})x} \tag{5.6}$$

$$e^{ikx} = e^{i\frac{\omega}{c}x(n')}e^{-\frac{\omega}{c}x(n'')} \tag{5.7}$$

where $k' = n'\omega/c$, and $k'' = n''\omega/c$. In most dielectrics $\chi \ll 1$, which leads to $n' = 1 + \chi'$ and $n'' = \chi''/2$. The envelope of the absorption is connected to χ'', and this is what has been calculated in the OOMMF simulation.

5.3 Discussion

This investigation has shown that we can improve the discrete structure of spin-wave resonance by changing the shape of the magnet, using a disk with a diameter of 80 nm. The most intriguing of our results concerns the parallel orientation of the magnetic field to the plane. There is no difference between the parallel and perpendicular orientations because of symmetry. The OOMMF simulation results show bonding–antibonding peaks, whereas the photovoltage spectroscopy displays a bonding–antibonding resonance as well as a series of additional resonances not predicted by theory, as seen in Figures 5.3 and 5.4.

Simultaneously, the amplitudes of the resonance peaks in the OOMMF simulation and the photovoltage spectroscopy increase with decreasing frequency. There are, therefore, peaks at zero field which are not predicted by theory, particularly at 35 GHz and 75 GHz (see Figure 5.3). The amplitude of the resonance peak observed in the photovoltage spectroscopy experiments is much smaller than the amplitude calculated by OOMMF simulation, as shown in Figures 5.2 and 5.3.

The photovoltage spectra are modelled by Equation 4.5 for different frequencies (see Figure 5.7). It shows the spectra that have been fitted with Equation 5.3. The photovoltage formula works very well as it gives the absorption which has Lorentzian shape. The width of the resonance is proportional to the damping α.

Chapter 6

Conclusions

6.1 Summary and Key Insights

A new method for electrical detection of electron spin resonance in two-dimensional electron gases, utilising perpendicular and parallel magnetic fields, has been demonstrated. The 2DEG detects microwaves amplified by the nanomagnet over the 30 - 110 GHz frequencies range down to -70 dBm of applied microwave power.

The results presented in Chapters 4 and 5 show that photovoltage spectroscopy using micron size Hall junctions is capable of sensing the magnetisation dynamics of nanomagnets with a size of 80 nm, which is inaccessible by Brillouin light scattering, which is limited to samples at least greater than the wavelength of light $>$ 500 nm. The results show that the discrete structure of spin-wave resonances depends on the shape of the magnets, the orientation of the magnetic field orientation relative to the magnetisation, the shape and the geometry of the nanomagnets. The sensitivity of this technique reveals the theoretically predicted fine structure of confined spin waves. There are additional experimental resonances not explained theoretically, which most likely arise from 3D volume spin waves not accounted for in OOMMF simulations. Localised spin-waves mode are observed which were confined in spin-wave wells near the pole surfaces. It is further given that hybrid structures provide a highly sensitive probing of the magnetisation dynamics down to -70 dBm at liquid helium temperature. The

technique complements established techniques such as BLS by providing access to remarkably small magnets, utilising submicron Hall junctions.

The relative peak amplitudes of photovoltage when the magnetisation is parallel to the long axis of the stripe indicate that Damon-Eshbach modes are much weaker than the dipolar edge spin-wave modes present when B_{dc} is perpendicular to the long axis. Bonding-antibonding pairs of edge spin waves are observed to form when the static magnetic field is perpendicular to the long axis. The larger magnitude of the photovoltage signal in this field orientation makes this case easier to interpret than other orientations.

The effect of magnetocrystalline anisotropy shifts the resonance to a new position relative to the prediction of the OOMMF simulation. The spectral calculation also confirms that the photovoltage formula given in Equation 4.5 works well and gives a Lorentzian-type line-shape. Overall, there is no remarkable difference between the results obtained from the magnetic stripe and the magnetic disk.

However, spin waves are likely to provide further insight into the magnetic characteristics of individual nanomagnets and their ability to channel information carried by spin waves. The rising interest in spin waves has been motivated by three major factors. The first is the rapid advances being made in nanotechnology. Second, the recent development of new experimental techniques has facilitated the study of high-frequency magnetisation dynamics. A third factor is the concept of a novel functional magnetic-field-controlled devices that depend integrally on spin waves. The emerging research field was sparked by the discovery of the potential of magnons as information carriers. Magnonics promises further opportunities in various fields of wave physics. Research into magnons stands to aid the development of theories of spin-wave excitation, propagation, and control within a medium that possesses continuously varying properties [121]. The use of magnons for new forms of information processing could greatly influence the future of electronics, as the spin waves of magnons have the potential to carry and process analogue signals and digital data simultaneously. Such magnonic technology may enable new devices that take advantage of the dynamic properties of magnons and do not rely on as change transport like conventional electronic devices and Joule dispersion. Making use of the spectrum of magnons, such devices could be easily reconfigurable and tuneable by means of an external magnetic field or

spin-polarised currents. Furthermore, magnonic devices offer practical potential, as the wavelengths of magnons are smaller by orders of magnitude than those of photons with an identical frequency (at the GHz to THz frequency range). Magnonic devices could, therefore, be reduced to nanoscale dimensions [122, 123].

Many engineering procedures rely on the measurement of small amplitude magnetic fields and increasingly require highly sensitive detectors capable of identifying weak magnetic fields. Furthermore, high densities of magnetic recording also require tiny magnetic elements and the ability to read small magnetic signals and change magnetisation states of GHz frequencies. A highly sensitive sensor is therefore required to precisely detect such a weak magnetic field, then, read the recorded signals. Giant magnetoresistance sensors have played a significant role in magnetic detection [124]. Amongst the wide range of available magnetic sensors, the giant magnetoimpedance (GMI) element and the superconducting quantum interference device (SQUID) are two examples of highly sensitive sensors. The GMI element typically possesses a detectable field sensitivity of 10^{-8} Oe. SQUIDs have a field sensitivity of 10^{-10} Oe, but are not suitable for detecting all types of magnetic systems because they are restricted to operating at low temperatures. It is acknowledged that there is a shortage of superconducting constituents that operate at ambient temperature. Despite having a hundred-fold lower field sensitivity than the SQUID, the GMI element is more widely used in a broad range of engineering applications. This is due to its soft magnetic composition, which allows it to operate effectively at room temperature. Therefore, for a proper application of the SQUID, we need to develop a room-temperature superconductor, whereas for the GMI element; we necessitate to develop a magnetically considerably softer material, which does not exist yet.

On the other hand, microwave sensors possess attractive features that make them suitable for different sensing applications at both low temperature and room temperature [125, 126]. The microwave sensor is completely different than the SQUID sensor, where the microwave sensor is measuring the power sensitivity depending on the magnetic field that oscillating per second, B_{ac} while the SQUID and GMI sensors are measuring the static magnetic field. Nevertheless, the advantages of the microwave sensor include simple structure and operation, high sensitivity, low manufacturing costs. Applications within the growing sectors of sensing,

security, networks, and communications that utilise RF and microwave technology have also played a part in maintaining momentum in these areas. GaAs metal-semiconductor field-effect transistors (MESFETs) are commonly selected for hybrid and monolithic integrated circuits operating above 10 GHz, as they may be employed very effectively at frequencies in the millimetre-wave range. With low intrinsic noise and high gain, they have proven to be a notable development within microwave technology [96]. Fundamental applications in the fields of remote sensing, wireless communications, GPS, and radar have been based on these transistors.

6.2 Prospects and Extensions of this work

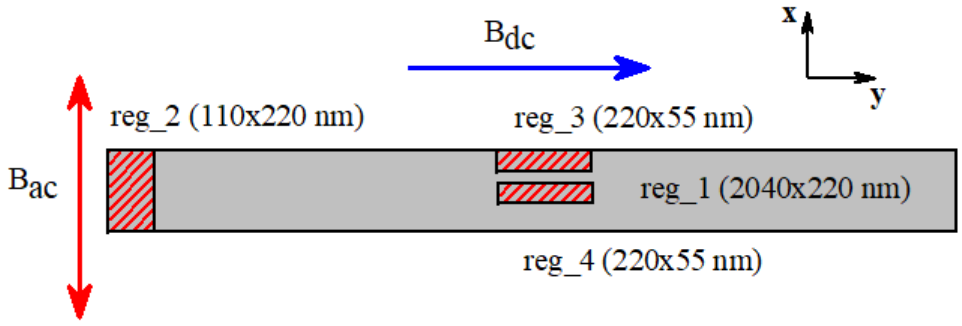

Figure 6.1 The position of the region in the magnetic stripes; the magnetisation at the full stripe (reg_1), the end of the stripe (reg_2), the edge centre (reg_3) and the centre reg_4.

The work presented here opens numerous avenues for future study. Previously, using OOMMF, the spectral dependencies and spatial distribution of magnetisation precession were obtained by analysis of magnetic susceptibility. The results obtained by OOMMF for the full stripe are in qualitative and quantitative agreement with those previously obtained in experiments, Figures 4.8, 4.9, 4.10, 4.11, 4.15, 4.16 in chapter 4, and Figures 5.2 and 5.3 in chapter 5.

Our experimental results shows some small peaks which could not be explained by the existing theory. To account for these peaks in the simulations, we propose a modification of the finite-element computation, in which different regions of the magnetised stripe are considered separately. Four different magnetisation regions

are considered: the full strip reg_1 (2040 nm $\times$ 220 nm), the region reg_2 on the end (110 nm $\times$ 220 nm), reg_3 in the centre with the edge (220 nm $\times$ 55 nm), and reg_4 in the centre (220 nm $\times$ 55 nm). The magnetisation in the centre oscillates differently than in other regions. So the advantage of the theory is that it can identify whether the peaks comes from the centre or the corner or the edge, making it more precise. Then these steps can be repeated with the micromagnetic disk to investigate the effect of the magnetisation in different regions.

Appendix A

List of publications

The work described in this thesis has led to the following publications:

- Almulhem NK, Stebliy ME, Nogaret A, Portal J-C, Beere HE, Ritchie DA, *Photovoltage detection of Damon–Eshbach and dipolar edge spin waves of nanomagnets with two-dimensional electron gas system* , Jpn. J. Appl. Phys. 57, 09TF1, 2018

- Almulhem NK, Stebliy M, Portal JC, Samardak A, Beere H, Ritchie D, Nogaret A, *Photovoltage detection of spin excitation of ferromagnetic stripe and disk at low temperature* , Jpn. J. Appl. Phys. 2020

Bibliography

[1] C. Kittel and P. McEuen. *Introduction to solid state physics*. Wiley New York, 1976.

[2] C. Bayer, J. Jorzick, S. O. Demokritov, A. N. Slavin, K. Y. Guslienko, D. V. Berkov, N. L. Gorn, M. P. Kostylev, and B. Hillebrands. Spin wave excitations in finite rectangular elements. In B. Hillebrands and A. Thiaville, editors, *Spin Dynamics in confined Magnetic Structures III*, chapter 2, pages 57–103. Springer-Verlag, Berlin, Heidelberg, 2006.

[3] P. Saraiva, A. Nogaret, J. C. Portal, H. E. Beere, and D. A. Ritchie. Dipolar spin waves of lateral magnetic superlattices. *Phys.Rev.B*, **82**:224417, 2010.

[4] A. Fernández-Pacheco, R. Streubel, O. Fruchart, R. Hertel, P. Fischer, and R. P. Cowburn. Three-dimensional nanomagnetism. *Nature Communications*, **8**:15756, 2017.

[5] T. Shinjo, T. Okuno, R. Hassdorf, K. Shigeto, and T. Ono. Magnetic vortex core observation in circular dots of permalloy. *Science*, **289**(5481):930–932, 2000.

[6] Y. Zhu, J.G. Zheng and G. A. Prinz. Ultrahigh density vertical magnetoresistive random access memory. *Journal of Applied Physics*, **87**(9):6668–6673, 2000.

[7] M. M. Miller, G. A. Prinz, S. F. Cheng, and S. Bounnak. Detection of a micron-sized magnetic sphere using a ring-shaped anisotropic magnetoresistance-based sensor: A model for a magnetoresistance-based biosensor. *Applied Physics Letters*, **81**(12):2211–2213, 2002.

[8] A. L. Barra, D. Gatteschi, and R. Sessoli. High-frequency epr spectra of a molecular nanomagnet: Understanding quantum tunneling of the magnetization. *Physical Review B*, **56**(13):8192, 1997.

[9] A. V. Chumak, V. I. Vasyuchka, A. A. Serga, and B. Hillebrands. Magnon spintronics. *Nature Physics*, **11**(6):453–461, 2015.

[10] C. W. Sandweg, M. B. Jungfleisch, V. I. Vasyuchka, A. A. Serga, P. Clausen, H. Schultheiss, B. Hillebrands, A. Kreisel, and P. Kopietz. Wide-range wavevector selectivity of magnon gases in brillouin light scattering spectroscopy. *Review of Scientific Instruments*, **81**:073902, 2010.

[11] M. Harder, Y. Gui, and C. M. Hu. Electrical detection of magnetization dynamics via spin rectification effects. *Phys. Rep.*, **661**:1, 2016.

[12] M. V. Costache, M. Sladkov, S. M. Watts, C. H. van der Wal, and B. J. van Wees. Electrical detection of spin pumping due to the precessing magnetization of a single ferromagnet. *Phys.Rev.Lett.*, **97**:216603, 2006.

[13] G. Gubbiotti, M. Kostylev, N. Sergeeva, M. Conti, G. Carlotti, T. Ono, A. N. Slavin, and A. Stashkevich. Brillouin light scattering investigation of magnetostatic modes in symmetric and asymmetric ni fe/ cu/ ni fe trilayered wires. *Physical Review B*, **70**(22):224422, 2004.

[14] M. Harder, Z. X. Cao, Y. S. Gui, X. L. Fan, and C. M. Hu. Analysis of the line shape of electrically detected ferromagnetic resonance. *Physical Review B*, **84**:054423, 2011.

[15] Y. Tserkovnyak, A. Brataas, G. E. Bauer, and B. I. Halperin. Nonlocal magnetization dynamics in ferromagnetic heterostructures. *Reviews of Modern Physics*, **77**(4):1375, 2005.

[16] J. S. Vainshtein, O. S. Yeltsina, E. I. Terukov, and O. M. Sreseli. Photocurrent and photovoltage spectroscopy of amorphous silicon nanoclusters. *Physica E: Low-dimensional Systems and Nanostructures*, **49**:72–75, 2013.

[17] J. Toušková, E. Samochin, J. Toušek, J. Oswald, E. Hulicius, J. Pangrác, K. Melichar, and T. Šimeček. Photovoltage spectroscopy of inas/gaas

quantum dot structures. *Journal of applied physics*, **91**(12):10103–10106, 2002.

[18] S. T. B. Goennenwein, S. W. Schink, A. Brandlmaier, A. Boger, M. Opel, R. Gross, R. S. Keizer, T. M. Klapwijk, A. Gupta, H. Huebl, C. Bihler, and M. S. Brandt. Electrically detected ferromagnetic resonance. **90**:162507, 2007.

[19] J. Reijniers and F. M. Peeters. Resistance effects due to magnetic guiding orbits. *Physical Review B*, **63**(16):165317, 2001.

[20] I. S. Ibrahim and F. M. Peeters. Two-dimensional electrons in lateral magnetic superlattices. *Physical Review B*, **52**(24):17321, 1995.

[21] A. Nogaret. Electron dynamics in inhomogeneous magnetic fields. *Journal of Physics: Condensed Matter*, **22**:253201, 2010.

[22] D. Uzur, A. Nogaret, H. E. Beere, D. A. Ritchie, C. H. Marrows, and B. J. Hickey. Probing the annular electronic shell structure of a magnetic corral. *Physical Review B*, **69**:241301, 2004.

[23] M. Dobers, J. P. Vieren, Y. Guldner, P. Bove, F. Omnes, and M. Razeghi. Electron-spin resonance of the two-dimensional electron gas in ga 0.47 in 0.53 as-inp heterostructures. *Physical Review B*, **40**(11):8075, 1989.

[24] J. R. Eshbach and R. W. Damon. Surface magnetostatic modes and surface spin waves. *Phys. Rev.*, **118**:1208, 1960.

[25] R. W. Damon and J. R. Eshbach. Magnetostatic modes of a ferromagnet slab. *Journal of Physics and Chemistry of Solids*, **19**:308, 1961.

[26] P. Wessels, A. Vogel, J. N. Todt, M. Wieland, G. Meier, and M. Drescher. Direct observation of isolated Damon-Eshbach and backward volume spin-wave packets in ferromagnetic microstripes. *Scientific reports.*, **6**:22117, 2016.

[27] O. Buisson, P. Gandit, R. Rammal, Y. Y. Wang, and B. Pannetier. Magnetization oscillations of a superconducting disk. *Physics Letters A*, **150**(1):36–42, 1990.

[28] M. Donahue. The object oriented micromagnetic framework (oommf) project at itl/nist. *http://math. nist. gov/oommf*, 1998.

[29] N. A. Spaldin. *Magnetic materials: fundamentals and applications*. Cambridge University Press, 2010.

[30] C. Chappert and P. Bruno. Magnetic anisotropy in metallic ultrathin films and related experiments on cobalt films. *Journal of Applied Physics*, **64**(10):5736–5741, 1988.

[31] P. V. Zinin, J. S. Allen III, and V. M. Levin. Mechanical resonances of bacteria cells. *Physical Review E*, **72**(6):061907, 2005.

[32] Y. E. Ryabov and A. Puzenko. Damped oscillations in view of the fractional oscillator equation. *Physical review B*, **66**(18):184201, 2002.

[33] N. K. Almulhem, M. E. Stebliy, A. Nogaret, J. C. Portal, H. E. Beere, and D. A. Ritchie. Photovoltage detection of damon–eshbach and dipolar edge spin waves of nanomagnets with two-dimensional electron gas system. *Japanese Journal of Applied Physics*, **57**(9S2):09TF01, 2018.

[34] Y. S. Gui, N. Mecking, and C. M. Hu. Quantized spin excitations in a ferromagnetic microstrip from microwave photovoltage measurements. *Physical review letters*, **98**:217603, 2007.

[35] P. Park, J. P. Eames, J. Engebretson, D.M. Berezovsky, and P.A. Crowell. Spatially resolved dynamics of localized spin-wave modes in ferromagnetic wires. *Physical review letters*, **89**(27):277201, 2002.

[36] G. E. Uhlenbeck and S. Goudsmit. Spinning electrons and the structure of spectra. *Nature*, **117**(2938):264, 1926.

[37] A. M. Paul. Dirac. the quantum theory of the electron. *Proc. Roy. Soc. Lond. A*, **117**:610–624, 1928.

[38] G. G. Scott. Gyromagnetic ratio of cobalt. *Physical Review*, **104**(6):1497, 1956.

[39] A. H. Morrish. The physical principles of magnetism. *The Physical Principles of Magnetism, by Allan H. Morrish, pp. 696. ISBN 0-7803-6029-X. Wiley-VCH, January 2001.*, page 696, 2001.

[40] D. Jiles. *Introduction to magnetism and magnetic materials*. CRC press, 2015.

[41] S. Chikazumi and C. D. Graham. *Physics of Ferromagnetism 2e*, volume **94**. Oxford University Press on Demand, 2009.

[42] X. F. Zhu, M. Harder, J. Tayler, A. Wirthmann, B. Zhang, W. Lu, Y. S. Gui, and C. M. Hu. Nonresonant spin rectification in the absence of an external applied magnetic field. *Physical Review B*, **83**:140402, 2011.

[43] K. Perzlmaier, M. Buess, C. H. Back, V. E. Demidov, B. Hillebrands, and S. O. Demokritov. Spin-wave eigenmodes of permalloy squares with a closure domain structure. *Physical review letters*, **94**(5):057202, 2005.

[44] A. Kaya and J. A. Bain. High frequency susceptibility of closure domian structures calculated using micromagnetic modeling. *J.Appl.Phys.*, **99**:08B708, 2006.

[45] R. M. White, R. M. White, and B. Bayne. *Quantum theory of magnetism*, volume **1**. Springer, 1983.

[46] E. M. Levin, V. K. Pecharsky, and K. A. Gschneidner Jr. Real and imaginary components of the alternating current magnetic susceptibility of ral 2 (r= gd, dy, and er) in the ferromagnetic region. *Journal of Applied Physics*, **90**(12):6255–6262, 2001.

[47] A. P. Guimarães and A. P. Guimaraes. *Principles of nanomagnetism*, volume **7**. Springer, 2009.

[48] R. M. Bozorth. Ferromagnetism. *Ferromagnetism, by Richard M. Bozorth, pp. 992. ISBN 0-7803-1032-2. Wiley-VCH, August 1993.*, page 992, 1993.

[49] J. M. D. Coey. *Magnetism and magnetic materials*. Cambridge university press, 2010.

[50] N. A. Sergeeva, S. M. Chérif, A. A. Stashkevich, M. P. Kostylev, and J. B. Youssef. Spin waves quantization in patterned exchange-coupled double layers. *Journal of magnetism and magnetic materials*, **288**:250–258, 2005.

[51] D. D. Stancil and A. Prabhakar. *Spin waves*. Springer, 2009.

[52] E. C. Stoner. Collective electron ferronmagnetism. *Proceedings of the Royal Society of London. Series A. Mathematical and Physical Sciences*, **165**(922):372–414, 1938.

[53] J. C. Slater. The ferromagnetism of nickel. ii. temperature effects. *Physical Review*, **49**(12):931, 1936.

[54] J. McDougall and E. C. Stoner. The computation of fermi-dirac functions. *Philosophical Transactions of the Royal Society of London. Series A, Mathematical and Physical Sciences*, **237**(773):67–104, 1938.

[55] D. Mazumdar. *Coherent magnetotunneling based on (001) magnesium oxide barrier*. 2007.

[56] A. G. Gurevich and G. A. Melkov. *Magnetization oscillations and waves*. CRC press, 1996.

[57] B. Hillebrands and K. Ounadjela. *Spin dynamics in confined magnetic structures I*, volume **83**. Springer Science & Business Media, 2003.

[58] M. T. Johnson, P. J. H. Bloemen, F. J. A. Den Broeder, and J. J. De Vries. Magnetic anisotropy in metallic multilayers. *Reports on Progress in Physics*, **59**(11):1409, 1996.

[59] D. Craik. *Magnetism: Principles and Applications*. Wiley, 1995.

[60] P. Rhodes and G. Rowlands. Proc. leeds philos. lit. soc. 1954.

[61] R. M. Nicklow, N. Wakabayashi, M. K. Wilkinson, and R. E. Reed. Spin-wave dispersion relation in dysprosium metal. *Physical Review Letters*, **26**(3):140, 1971.

[62] M. P. Kostylev, G. Gubbiotti, J. G. Hu, G. Carlotti, T. Ono, and Stamps R. L. Dipole-exchange propagating spin-wave modes in metallic ferromagnetic stripes. *Phys.Rev.B*, **76**:054422, 2007.

[63] T. Sebastian, K. Schultheiss, B. Obry, B. Hillebrands, and H. Schultheiss. Micro-focused brillouin light scattering: imaging spin waves at the nanoscale. *Frontiers in Physics*, **3**:35, 2015.

[64] A. Prabhakar and D. D. Stancil. *Spin waves: Theory and applications*. Springer, 2009.

[65] K. Vogt, F. Y. Fradin, J. E. Pearson, T. Sebastian, S. D. Bader, B. Hillebrands, A. Hoffmann, and H. Schultheiss. Realization of a spin-wave multiplexer. *Nature communications*, **5**:3727, 2014.

[66] H. Zhou, X. Fan, F. Wang, C. Jiang, J. Rao, X. Zhao, Y. S. Gui, C.M. Hu, and D. Xue. Electric field controlled reversible magnetic anisotropy switching studied by spin rectification. *Applied Physics Letters*, **104**(10):102401, 2014.

[67] B. Hillebrands, P. Baumgart, and G. Güntherodt. Brillouin light scattering from spin waves in magnetic layers and multilayers. *Applied Physics A*, **49**(6):589–598, 1989.

[68] S. O. Demokritov and B. Hillebrands. Spinwaves in laterally confined magnetic structures. In *Spin Dynamics in Confined Magnetic Structures I*, pages 65–92. Springer, 2002.

[69] K. Y. Guslienko, S. O. Demokritov, B. Hillebrands, and A. N. Slavin. Effective dipolar boundary conditions for dynamic magnetization in thin magnetic stripes. *Phys.Rev.B*, **66**:132402, 2002.

[70] J. Jorzick, S. O. Demokritov, C. Mathieu, B. Hillebrands, B. Bartenlian, C. Chappert, F. Rousseaux, and A. N. Slavin. Brillouin light scattering from quantized spin waves in micron-size magnetic wires. *Physical Review B*, **60**(22):15194, 1999.

[71] B. A. Kalinikos and A. N. Slavin. Theory of dipole-exchange spin wave spectrum for ferromagnetic films with mixed exchange boundary conditions. *Journal of Physics C: Solid State Physics.*, **19**:7013, 1986.

[72] R. I. Joseph and E. Schlömann. Demagnetizing field in nonellipsoidal bodies. *Journal of Applied Physics*, **36**(5):1579–1593, 1965.

[73] P. H. Bryant, J. F. Smyth, S. Schultz, and D. R. Fredkin. Magnetostatic-mode spectrum of rectangular ferromagnetic particles. *Physical Review B*, **47**(17):11255, 1993.

[74] R. B. S. Oakeshott and A. MacKinnon. Conduction in a spatially varying magnetic field: one-dimensional strips, with zero mean field. *Journal of Physics: Condensed Matter*, **5**(50):9355, 1993.

[75] G. T. Rado and J. R. Weertman. Spin-wave resonance in a ferromagnetic metal. *Journal of Physics and chemistry of solids*, **11**(3-4):315–333, 1959.

[76] J. Reijniers and F. M. Peeters. Snake orbits and related magnetic edge states. *Journal of Physics: Condensed Matter*, **12**(47):9771, 2000.

[77] R. C. O'handley. Soft magnetic materials. *Modern Magnetic Materials*, 2000.

[78] B. D. Cullity and C. D. Graham. *Introduction to magnetic materials*. John Wiley & Sons, 2011.

[79] M. Krawczyk and D. Grundler. Review and prospects of magnonic crystals and devices with reprogrammable band structure. *Journal of Physics: Condensed Matter*, **26**(12):123202, 2014.

[80] G. Andersson, T. Burkert, P. Warnicke, M. Björck, B. Sanyal, C. Chacon, C. Zlotea, L. Nordström, P. Nordblad, and O. Eriksson. Perpendicular magnetocrystalline anisotropy in tetragonally distorted fe-co alloys. *Physical review letters*, **96**(3):037205, 2006.

[81] J. C. M. Henning and J. H. Den Boef. Magnetostriction measurement by means of strain modulated ferromagnetic resonance (smfmr). *Applied physics*, **16**(4):353–357, 1978.

[82] P. D. Ye, D. Weiss, R. R. Gerhardts, K. Von Klitzing, K. Eberl, H. Nickel, and C. T. Foxon. Strain-induced magnetoresistance oscillations in gaas-algaas heterojunctions with ferromagnetic and superconducting submicrometre gratings. *Semiconductor science and technology*, **10**(5):715, 1995.

[83] J. J. Harris, J. A. Pals, and R. Woltjer. Electronic transport in low-dimensional structures. *Reports on progress in Physics*, **52**(10):1217, 1989.

[84] J. H. Davies. *The physics of low-dimensional semiconductors: an introduction*. Cambridge university press, 1998.

[85] A. Nogaret, M. E. Stebliy, J. C. Portal, A. S. Samardak, A. V. Ognev, H. E. Beere, and D. A. Ritchie. Photovoltage spectroscopy of dipolar spin waves in dy micromagnets. *Solid State Phenomena*, **215**:400, 2014.

[86] M. C. Lemme, T. J. Echtermeyer, M. Baus, and H. Kurz. A graphene field-effect device. *IEEE Electron Device Letters*, **28**, number=4, pages=282–284, year=2007, publisher=IEEE.

[87] C. W. J. Beenakker and H. van Houten. Quantum transport in semiconductor nanostructures. In *Solid state physics*, volume **44**, pages 1–228. Elsevier, 1991.

[88] B. Heinrich, Y. Tserkovnyak, G. Woltersdorf, A. Brataas, R. Urban, and G. E. W. Bauer. Dynamic exchange coupling in magnetic bilayers. *Physical review letters*, **90**(18):187601, 2003.

[89] L. D. Landau and E. M. Lifshitz. Quantum mechanics, 1977.

[90] D. N. Lawton, A. Nogaret, S. J. Bending, D. K. Maude, J. C. Portal, and M. Henini. Suppression of electron channelling in microscopic magnetic waveguides. *Phys.Rev.B*, **64**:033312, 2001.

[91] R. R. Gerhardts. Quasiclassical calculation of magnetoresistance oscillations of a two-dimensional electron gas in spatially periodic magnetic and electrostatic fields. *Physical Review B*, **53**(16):11064, 1996.

[92] A. Nogaret, D. N. Lawton, D. K. Maude, J.C. Portal, and M. Henini. Hall anomaly of diffusive magnetic waveguides. *Phys.Rev.B*, **67**:165317, 2003.

[93] Ist innovative sensor technolog. platinum sensor with wires - 600 °C series. https://www.ist-ag.com/en/products-services/temperature-sensors, May 2013.

[94] J. Liu, Y. Li, and H. Zhao. A temperature measurement system based on pt100. In *2010 International Conference on Electrical and Control Engineering*, pages 296–298. IEEE, 2010.

[95] J. R. James, P. S. Hall, and C. Wood. *Microstrip antenna: theory and design*. Number 12. Iet, 1986.

[96] D. M. Pozar. Microwave engineering. *Wiley*, 2012.

[97] V. Bernard and J. P. I. Iloh. Microstrip antenna design using transmission line model. *International Journal of Emerging Technology and Advanced Engineering*, **3**(11), 2013.

[98] S. Sharma, C. C. Tripathi, and R. Rishi. Impedance matching techniques for microstrip patch antenna. *Indian Journal of Science and Technology*, **10**(28):1–16, 2017.

[99] G. W. Johnson. *LabVIEW graphical programming*. Tata McGraw-Hill Education, 1997.

[100] T. Jeffery and J. I. M. Kring. Labview for everyone. *Prentice Hall*, 2002.

[101] G. Bertotti, I. D. Mayergoyz, and C. Serpico. Spin-wave instabilities in large-scale nonlinear magnetization dynamics. *Physical review letters*, **87**(21):217203, 2001.

[102] V. Donchev, T. Ivanov, K. Germanova, and K. Kirilov. Surface photovoltage spectroscopy–an advanced method for characterization of semiconductor nanostructures. *Spectroscopy*, **8**, 2010.

[103] N. Vukadinovic and F. Boust. Three-dimensional micromagnetic simulations of magnetic excitations in cylindrical nanodots with perpendicular anisotropy. *Physical Review B*, **75**(1):014420, 2007.

[104] M. E. Stebliy, S. Jain, A. G. Kolesnikov, A. V. Ognev, A. S. Samardak, A. V. Davydenko, E. V. Sukovatitcina, L. A. Chebotkevich, J. Ding, and J. Pearson. Vortex dynamics and frequency splitting in vertically coupled nanomagnets. *Scientific reports*, **7**(1):1127, 2017.

[105] JC Denardin, E Burgos, R Lavín, S Vojkovic, J Briones, and M Flores. Magnetic properties of co/cu/py antidot films. *arXiv preprint arXiv:1406.7322*, 2014.

[106] S. Michea, J. Briones, J. L. Palma, R. Lavín, J. Escrig, R. Rodríguez-Suárez, and J. C. Denardin. Forc and micromagnetism approach to the domain structure of cobalt antidot arrays. *arXiv preprint arXiv:1401.6064*, 2014.

[107] M. E. Stebliy, A. V. Ognev, A. S. Samardak, and L. A. Chebotkevich. Magnetoresistive properties of the "small disk on a big disk" nanostructure. *Journal of Applied Physics*, **113**(17):17B527, 2013.

[108] A. Vogel, A. Drews, T. Kamionka, M. Bolte, and G. Meier. Influence of dipolar interaction on vortex dynamics in arrays of ferromagnetic disks. *Physical review letters*, **105**(3):037201, 2010.

[109] M. Buess, R. Hollinger, T. Haug, K. Perzlmaier, U. Krey, D. Pescia, M. R. Scheinfein, D. Weiss, and C. H. Back. Publisher's note: Fourier transform imaging of spin vortex eigenmodes [phys. rev. lett. 93, 077207 (2004)]. *Physical Review Letters*, **93**(12):129902, 2004.

[110] A. Barman, V. V. Kruglyak, R. J. Hicken, J. M. Rowe, A. Kundrotaite, J. Scott, and M. Rahman. Imaging the dephasing of spin wave modes in a square thin film magnetic element. *Physical Review B*, **69**(17):174426, 2004.

[111] T. Guenault. *Basic superfluids*. CRC press, 2002.

[112] J. A. C. Bland, A. Hirohata, Y. B. Xu, C. M. Guertler, and S. N. Holmes. Spin-polarized electron transport processes at the ferromagnet/semiconductor interface. *IEEE transactions on magnetics*, **36**(5):2827–2832, 2000.

[113] A et al Nogaret. Magnetic properties of co/cu/py antidot films. *Phys. Rev. Lett*, 2020.

[114] V. E. Demidov, S. O. Demokritov, K. Rott, P. Krzysteczko, and G. Reiss. Self-focusing of spin waves in permalloy microstripes. *Applied Physics Letters*, **91**(25):252504, 2007.

[115] W. Bang, J. Lim, J. Trossman, D. Amanov, M. B. Jungfleisch, A. Hoffmann, and J. B. Ketterson. Measurements of long-wavelength spin waves for the magnetic field in the damon-eshbach, backward-volume and forward-volume geometries of an yttrium iron garnet film. *Journal of Applied Physics*, **123**(12):123902, 2018.

[116] H. Ammari, L. Halpern, and K. Hamdache. Thin ferromagnetic films. *Asymptotic Analysis*, **24**(3, 4):277–294, 2000.

[117] H. Hata, M. Goto, A. Yamaguchi, T. Sato, Y. Nakatani, and Y. Nozaki. Coupled oscillations of vortex cores confined in a ferromagnetic elliptical disk. *Physical Review B*, **90**(10):104418, 2014.

[118] H. Moore. *MATLAB for Engineers*. Pearson, 2017.

[119] E. Pärt-Enander, A. Sjöberg, B. Melin, and P. Isaksson. *The MATLAB handbook*. Addison-Wesley Harlow, 1996.

[120] M. Fleischhauer, A. Imamoglu, and J. P. Marangos. Electromagnetically induced transparency: Optics in coherent media. *Reviews of modern physics*, **77**(2):633, 2005.

[121] V. V. Kruglyak, S. O. Demokritov, and D. Grundler. Magnonics. *Journal of Physics D: Applied Physics*, **43**(26):264001, 2010.

[122] A. V. Chumak and H. Schultheiss. Magnonics: spin waves connecting charges, spins and photons. *arXiv preprint arXiv:1901.07021*, 2019.

[123] R. L. Stamps, S. Breitkreutz, J. Åkerman, A. V. Chumak, Y. Otani, G. E. W. Bauer, J. Thiele, M. Bowen, S. A. Majetich, M. Kläui, and others. The 2014 magnetism roadmap. *Journal of Physics D: Applied Physics*, 47(33):333001, 2014.

[124] C. Reig, M. D. Cubells-Beltrán, and M. D. Ramírez. Magnetic field sensors based on giant magnetoresistance (gmr) technology: Applications in electrical current sensing. *Sensors*, **9**(10):7919–7942, 2009.

[125] R. Joffe, E. O. Kamenetskii, and R. Shavit. Novel microwave near-field sensors for material characterization, biology, and nanotechnology. *Journal of Applied Physics*, **113**(6):063912, 2013.

[126] M. Hofmann, G. Fischer, R. Weigel, and D. Kissinger. Microwave-based noninvasive concentration measurements for biomedical applications. *IEEE Transactions on Microwave Theory and Techniques*, **61**(5):2195–2204, 2013.